Numerical Simulation and Analysis of Cavitating Flow around Hydrofoil and in Injector Nozzle

Thesis submitted in fulfilment of the requirements for the Degree of

DOCTOR OF PHILOSOPHY

By

SRIJNA SINGH

Department of Mechanical Engineering

Bennett University (The Times Group)

Greater Noida, Uttar Pradesh-201310, India

November 2023

DECLARATION BY THE SCHOLAR

I hereby declare that the work reported in the Ph.D. thesis entitled "**Numerical Simulation and Analysis of Cavitating Flow around Hydrofoil and in Injector Nozzle**" submitted at Bennett University, Greater Noida, India, is an authentic record of my work carried out under the supervision of **Dr. Mohammad Danish** and **Dr. Kaushik Saha**. I have not submitted this work elsewhere for any other degree or diploma. I am fully responsible for the contents of my Ph.D. Thesis.

(Signature of the Scholar)

Srijna Singh

Department of Mechanical Engineering

Bennett University, Greater Noida, India

Date: 8 November 2023

SUPERVISOR'S CERTIFICATE

This is to certify that the thesis entitled "**Numerical Simulation and Analysis of Cavitating Flow around Hydrofoil and in Injector Nozzle**", being submitted by **Srijna Singh** to the Bennett University for the award of the degree of **Doctor of Philosophy (Ph.D.)**, is a record of the bonafide research carried out by her which has been prepared under our supervisions in conformity with the rules and regulations of the Bennett University. The research reports and results presented in the thesis has not been submitted for any degree or diploma in any other university or institute.

(Signature of Supervisor)

(Signature of Co-Supervisor)

Dr. Mohammad Danish
Associate Professor
Department of Mechanical Engineering
Bennett University
Greater Noida-201310
India

Dr. Kaushik Saha
Assistant Professor
Department of Energy Science and Engineering
Indian Institute of Technology Delhi
New Delhi-110016
India

ACKNOWLEDGEMENTS

I would like to express my deep gratitude and great pleasure as I extend my heartfelt thanks to my supervisors **Dr. Mohammad Danish** and **Dr. Kaushik Saha** for their consistent guidance, continuous encouragement, and strong support in every stage of my Ph.D. research. Working under them has been great experience for me and I am very thankful to them for building up my confidence and for having faith in me during my Ph.D. I deeply appreciate their kindness and contributions not only to my research but also to my professional growth.

I am grateful to my committee members, namely Dr. Neelanchali Asija Bhalla, Dr. Deepali Atheaya, Dr. Neelam Choudhary for their valuable suggestions and insightful advice regarding my research. My special thanks to Dr. Michele Battistoni at University of Perugia, Italy, Dr. Baij Nath Singh, and Akhil Ailaboina, also a co-authors of our paper for their continuous support during my research. The computational support provided by IIT Delhi, is greatly appreciated.

I am thankful to my colleagues and friends, Madhu, Shikha, Manish, Sumit, Tushar, Amit, Abhishek, Mukul, Gyan, Sahil, Aryaman, Akshay, Gagneet, and Aanchal, for their help and cooperation in many ways during my Ph.D. My thanks are also due to all the faculty and other staff members for their support and keenness in my work.

Finally, I would like to take this opportunity to express my heartfelt gratitude to my parents (Mr. Braham Pal Singh and Mrs. Mahendri Singh), my sister (Vibha), my brothers (Swatantra and Ujjawal), and my dogs (Tipu and Leo), whose unwavering support and unconditional love have been the driving force behind my journey towards completing my Ph.D. Their constant encouragement, sacrifices, and belief in my abilities have been instrumental in shaping the person I am today.

List of Tables

List of Figures

NOMENCLATURE

b	Span of the hydrofoil, m
c	Chord length of hydrofoil, m
C_l	Lift coefficient
C_d	Drag coefficient
C_p	Pressure Coefficient
D	Mass diffusivity, m^2/s
e	Specific internal energy, J/kg
E	Young's modulus, GPa
h_m	Specific enthalpy of m*th* species, kJ/kg
k	Turbulent kinetic energy, m^2/s^2
p	Local static pressure, Pa
p_v	Vapor pressure of liquid, Pa
p_∞	Freestream pressure, Pa
R_e, R_c	Evaporation and condensation rate, $kg/(m^3.s)$
Re	Reynolds number based on the chord length
S_m	Source term in species transport equation.
t	Time, s
T	Local cell temperature, K
u_i	Advecting mean velocity, m/s
u_j	Advected mean velocity, m/s
U_∞	Freestream velocity, m/s
x	Local cell vapor quality

$\bar{x}$ Local cell equilibrium quality

Greek

α Angle of attack, degree

α_v Vapor volume fraction

ϵ Rate of dissipation of turbulent kinetic energy, m^2/s^3

σ Cavitation number

μ Molecular viscosity, Pa.s

μ_l Viscosity of water, Pa.s

μ_v Viscosity of water-vapor, Pa.s

μ_t Turbulent viscosity, Pa.s

μ_{eff} Effective viscosity, Pa.s

ν Poisson's ratio

ρ_l Liquid density, kg/m^3

ρ_v Vapor density, kg/m^3

ρ_m Mixture density, kg/m^3

σ_{ij} Strain rate tensor, 1/s

σ_{ij} Strain rate tensor, 1/s

τ_{ij} Reynolds stress, Pa

TABLE OF CONTENTS

ABSTRACT

Cavitation occurs in flow regions where the hydrodynamic effect reduces the local pressure below the saturation vapor pressure of the liquid, causing the formation of vapor bubbles. When these vapor bubbles enter the region of higher pressure, they collapse violently producing enough force to damage the solid body. In case of hydrofoils, cavitation can affect the hydrodynamic and structural performance potentially. In injector nozzles, cavitation can cause a fuel injection instability and decreased fuel efficiency. Cavitation on hydrofoils and nozzles mainly depends on the flow parameters, shape and material of the hydrofoil or nozzle. In the present work to study the cavitation phenomenon three different studies have been made on hydrofoils and in injector nozzle. In first part of the work, the performance of two different cavitation model and four different turbulence models is compared with the available experimental data on cavitating NACA4412 and Clark-y hydrofoil in terms of lift coefficient, drag coefficient, Strouhal number and velocity profiles using ANSYS Fluent. Among all the turbulence models, the Realizable k-ϵ turbulence was found to be more accurate, whereas the Zwart-Gerber-Belamri cavitation model is found to be more reliable. Using the Realizable k-ϵ and Zwart-Gerber-Belamri cavitation model, the research was further extended to study the hydrodynamic and structural performance of 3D stainless steel MHKF-180 and NACA4418 cavitating hydrofoils using one-way fluid structure interaction (FSI). The simulation is performed at a chord-based Reynolds number, Re = 750000, for different cavitation numbers and angles of attack. On comparing the hydrodynamic performance of both the foils, in terms of lift coefficient, MHKF-180 found to perform better than NACA4418 under the cavitating condition. Whereas, from structural point of view, the MHKF-180 shows larger tip deformation and von Mises stress than NACA4418 hydrofoil. Further, in the last part of the work, the numerical investigation of cavitation characteristics of conventional (n-dodecane fuel) is compared with the alternative fuel (Oxymethylene ether, OME_3) in Engine Combustion Network (ECN) Spray C037 nozzle using CONVERGE code. RNG $\kappa - \epsilon$ turbulence model is used to determine the effect of turbulence, and phase change inside the nozzle is predicted using the Homogeneous Relaxation Model (HRM) coupled with a multiphase mixture model. For model validation, the simulated mass flow rate and cavitation contour shape of n-dodecane fuel are compared with the experimental result provided in the literature. Among both the fuels OME_3 found to be more cavitating as compared to n-dodecane fuel.

CHAPTER 1

INTRODUCTION

Cavitation, which is defined as a phenomenon of the formation of vapor bubbles in a liquid flow, has been a subject of intensive research because of its complex multiphase flow dynamics and the destruction it can do to the adjacent solid surfaces (Brennen 2005). Cavitation occurs in flow regions where the hydrodynamic effect reduces the local pressure below the saturation vapor pressure of the liquid, causing the formation of vapor bubbles. When these vapor bubbles enter the region of higher pressure, they collapse violently producing enough force to damage the solid body. Cavitation can be commonly seen around the propellers, hydrofoils, impellers, injector nozzles etc.

In marine applications, the shape of the propellers is designed in a way that it can provide enough lift to keep the ship's hull on the water surface. The required lift can be achieved if the fluid on the top surface of the propeller flows at a higher velocity than its bottom surface, which in turn, reduces the pressure on the top surface (Štigler 2009). However, the reduced pressure on the top surface makes it prone to cavitation. Similarly, in injector nozzles during fuel injection process, a very large pressure differential acts across the injector. The fuel is passed through small orifice to form smaller droplets. Due to this, a large pressure drop occurs at the orifice's entry, resulting in cavitation inside the injector (Vijayakumar 2018).

A non-dimensional number which is used as an indicator of cavitation inception is called cavitation number (σ). The cavitation number is defined as the ratio of the difference of freestream pressure and vapor pressure to dynamic pressure, which is given by (Brennen 2005)

$$\sigma = \frac{p_\infty - p_v}{\frac{1}{2}\rho_l U_\infty^2}. \quad (1)$$

where p_∞ is the freestream pressure (Pa), p_v is the vapor pressure of liquid (Pa) at the reference temperature, ρ_l is density of liquid (kg/m^3), and U_∞ is the free stream velocity (m/s). From Eq. (1), it is clear that higher cavitation number means cavitation is less likely to occur, while a lower cavitation number means a higher likelihood of cavitation.

1.1 Cavitation Fundamentals

Cavitation is the process where phase change takes place due to local pressure drop. The phenomenon of cavitation was first observed in rotating machinery in the late 19th century by Torricelli, and later by Euler and Newton. The negative impact of cavitation phenomenon on the performance of a ship propeller was first observed by Parsons in 1893, who built the first cavitation tunnel. Understanding the causes of cavitation is crucial in managing its effects. Several important literatures have contributed to our understanding of cavitation. For instance, the work of Blake and Maga (1975) investigated the relationship between the velocity, pressure, and cavitation formation in a centrifugal pump, shedding light on the role of flow conditions in cavitation inception. Moreover, the study by Iwai and Li (2003) elucidated the impact of fluid properties, such a viscosity and surface tension, on cavitation behaviour, and highlighted the importance of considering fluid properties in predicting cavitation phenomena. The effect of cavitation can be detrimental to fluid systems. Cavitation erosion has been a significant concern in various industrial applications, including pumps, propellers, and hydraulic systems.

To mitigate the adverse effects of cavitation, engineers have developed numerous strategies like optimizing system design, and employing specialized materials. Although cavitation seems similar to boiling with respect to formation of vapor bubbles, there is basic difference. Boiling takes place when thermodynamics state change from liquid to vapor at constant pressure and by increasing the temperature. Whereas cavitation is a thermodynamic process where state change takes place at constant temperature due to sudden drop in pressure.

1.1.1 Types of Cavitation

Cavitation has different stages and types. There are two stages of cavitation one is *incipient*, and another is *the developed* stage (Brennen 2005). Incipient cavitation refers to the initial stage of cavitation, where bubbles are just detectable. The bubble size is very small, and it covers only a limited zone of the body. Cavitation inception is considered to take place when the bubble grew to an observable size of approximately 1 mm (Brennen 2005). Further, with changes in conditions (pressure, velocity, temperature) the cavitation grows and reaches a developed stage. Cavitation can be classified into various categories, including partial cavitation, supercavitation, traveling bubble cavitation, vortex cavitation, sheet cavitation, and cloud cavitation.

Partial cavitation (Fig. 1.1) refers to the phenomenon where cavitation only covers the partial surface of the hydrofoil surface in the fluid flow. The presence of partial cavitation on the hydrofoil reduces the hydrodynamic performance of the hydrofoil, leading to lower lift and increased drag. The occurrence of partial cavitation depends on various factors such as the shape of the hydrofoil, flow velocity, the fluid density, and the pressure of the fluid.

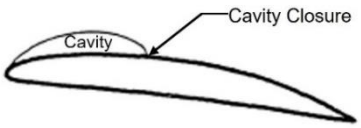

Fig. 1.1: Partial cavitation on hydrofoil (Fine 1988).

Supercavitation (Fig. 1.2) is a phenomenon where a cavity completely surrounds the body and separates it from the surrounding liquid. The supercavitation on hydrofoil reduces the drag force and allows the body to attain high speed. This can occur in high-speed underwater systems such as torpedoes and can provide significant improvement in performance. It is also considered beneficial in injector nozzles for the primary atomization as there is no shear resistance on the liquid jet due to injector walls, therefore liquid jet is able to exit at higher velocity (Saha 2014).

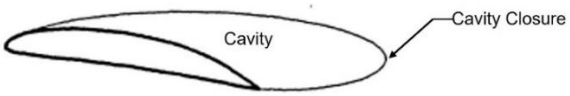

Fig. 1.2: Supercavitating hydrofoil (Fine 1988).

Traveling bubble cavitation (Fig. 1.3) refers to the movement of cavitation bubbles in the fluid flow. The bubble moves away from their nucleation site, expands, shrinks, and then collapses. The movement of bubbles is caused by the flow velocity, pressure gradients, or other parameters. Such traveling bubbles can occur in low-pressure areas along solid boundaries, or in the interior of the liquid, either at the center of moving vortices or in highly turbulent regions in turbulent shear fields.

Fig. 1.3: Traveling bubble cavitation on NACA4412 hydrofoil (Kermeen 1956).

Vortex cavitation (Fig. 1.4) is found in the applications where the entire vortex center is filled with the vapor bubble. In many high Reynolds number flows that are crucial in practical applications, there is an area of intense vorticity where pressure in the vortex center is much lower than in the rest of the flow. For instance, in the tip vortices of ship propellers or pump impellers, or in the swirling flow of water turbine's draft tube, cavitation inception often occurs in these vortices, and if the cavitation number decreases further, cavity fills the complete vortex center.

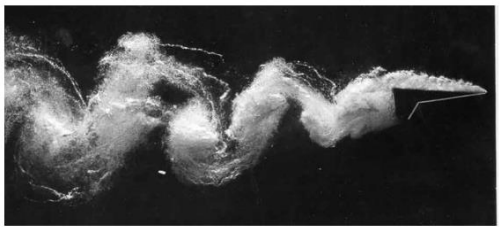

Fig. 1.4: Cavitation vortices in the wake of lift flat plate (Brennen 2014).

Sheet cavitation (Fig. 1.5) refers to the formation of thin, flat layer of vapor bubble that form along the surface of a hydrofoil or other underwater object. It is also referred to as fixed, attached or pocket cavitation. It is generally associated with high flow velocities and low liquid pressure, which results in low vapor pressure and high vapor formation. This vapor layer can then interact with the solid surface, causing erosion and others forms of surface damage.

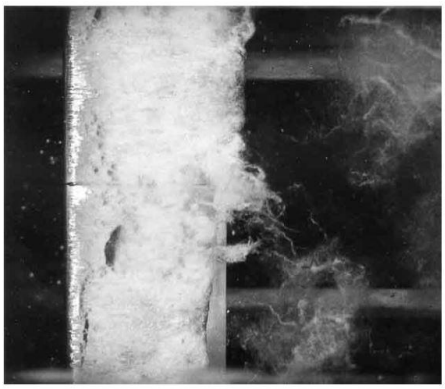

Fig. 1.5: Sheet cavitation on NACA4412 hydrofoil (Kermeen 1956).

Cloud cavitation (Fig. 1.6) is the phenomenon in which the unsteady sheet of cavity is periodically broken down into cloud-like structures which sheds into the wake of submerged body. These vapor clouds contain numerous microbubbles. The vapor cloud can cause significant increases in drag on the submerged body and can also damage the surface of the object due to implosion of the vapor bubbles.

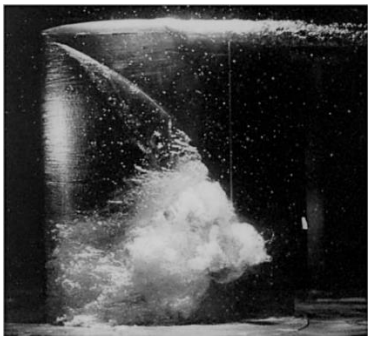

Fig. 1.6: Cloud cavitation on the hydrofoil (Brennen 2014).

1.1.2 Parameters Affecting Cavitation

The saturation pressure is mainly responsible for the inception of cavitation phenomenon, but there are other parameters also which affects the cavitation:

1. Cavitation number: The cavitation number affects cavitation because it determines the potential for the fluid to cavitate. When the cavitation number is low, there is a higher likelihood of cavitation occurrence. This is because the dynamic pressure of the fluid is closer to or even exceeds the vapor pressure of the fluid, causing the fluid to undergo phase change and form vapor bubbles.
2. Liquid temperature: The liquid temperature determines the saturation pressure of the liquid, which tells about the possibility of cavitation. Moreover, in our study an isothermal modelling approach is adopted.
3. Turbulence: If Reynolds number is high enough, the flow in general will be turbulent. Turbulence can have a significant impact on the formation and behaviour of cavitation. In turbulent flows, the velocity of the fluid varies randomly in both space and time. This randomness can lead to variations in pressure, and consequently, to the formation of cavitation bubbles.
4. Surface conditions of solid boundaries: The surface condition of the geometry can significantly affect the formation and behaviour of cavitation in several ways. For example, rough or irregular surfaces can promote the formation of cavitation bubbles by providing the nucleation sites for vapor bubbles to form. These bubbles can then grow and collapse, leading to increased erosion and damage.

1.2 Motivation

Cavitation can be harmful in several circumstances. Pumps, propellers, and hydraulic machinery, nozzles are examples of where cavitation can cause damage, as vibration and

surface erosion induced by cavitation not only contribute to poor performance but also diminishes overall structural integrity. In *pumps and turbines*, cavitation can reduce their lifespan by causing erosion and pitting of blades and surfaces (Noon et al. 2021). Cavitation also produced large noise due to collapse of vapor pockets near the solid surface, causing large impact stresses on the surface which can damage bearings, seals, and other components (Gnanaskandan 2015). Fig. 1.7 depicts the cavitation-damaged propeller blade and centrifugal pump. Take note of the concentrated damage on the tip of propeller blade, where the blade's speed is greatest. In *hydrofoils*, cavitation can affect the hydrodynamic performance by increasing the drag force and reducing the lift force (Brennen 2005). Cavitation can also cause vibrations and instabilities in hydrofoil, which can lead to failure of the hydrofoil in extreme cases. In *injector nozzles,* pressure drop can result in cavitation and may reduce the efficiency of the nozzle (Piehl and Bravo 2018). It may also cause wear and corrosion inside the nozzle leading to clogging of the nozzle and reduced performance. Fig. 1.8 shows the schematic of undamaged sac-type nozzle and damaged needle and sac due to cavitation.

However, cavitation has some advantageous effects also. In applications such as homogenizing liquids, mixing and breaking down particles, and in industry cleaning, the energy generated by cavitation is utilized to perform specific tasks. Shockwave lithotripsy, which is used to destroy kidney stones, is another example of cavitation being used to benefit a process. Supercavitation on torpedoes is another example of cavitation used for reducing drag, among different methods supercavitation is regarded as the most promising due to its ability to substantially decrease viscous drag by enveloping an underwater vehicle within a low-density gas bubble (Kim et al. 2021). Cavitation in diesel fuel injectors has the potential to improve the formation of the fuel spray by enhancing the initial breakup and subsequent atomization of the liquid fuel jet (Som et al. 2012). Cavitation can be employed in the food industry to enhance processes such as homogenization and emulsification. It can be used to break down particles and mix ingredients more effectively in food production (Kamal et al. 2022). Hydrodynamic cavitation can be used for degrading the complex contaminates for wastewater treatment. In this method certain pollutants move into expanding cavities with water molecules due to pressure changes, and when these cavities collapse, high pressure and temperature conditions cause pollutants to break down, forming free radicals and leading to degradation of pollutants (Darandale et al. 2023).

Understanding cavitation is crucial in order to minimize its detrimental effects while using its positive effects for different applications. A study of cavitation can be done both

through experimentation and numerical simulations. In recent years, experiments have greatly enhanced our understanding of cavitation, but conducting experimental measurements for cavitating flows is quite challenging. Numerical simulations can provide valuable insights and fill gaps in our understanding. They offer a cost-effective approach to simulating a large number of cases, testing, and predicting outcomes including scenarios that may be challenging to test experimentally. Furthermore, validated simulations can provide information that is difficult to attain through experimental means. Due to recent advances in parallel computing and numerical methods, it is now easier to simulate complex cavitating flows consisting of range of length scales and time scales. Advanced post-processing techniques also enable a deeper understanding of the three-dimensional nature of cavitating flows, as well as being able to predict the growth and collapse of vapor cavities of varying size and rates. With this motivation an overall objective of this thesis is to numerically investigate the cavitating flows on hydrofoils and injector nozzles.

Fig. 1.7: Damage due to cavitation (a) erosion near the tip of propeller blade (Britannica), (b) centrifugal pump impeller (Noon et al. 2021).

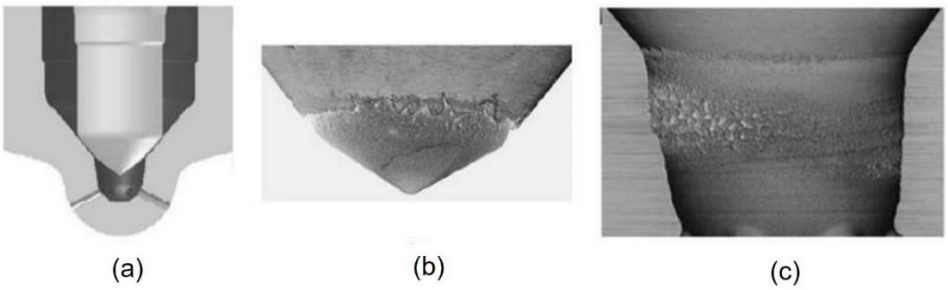

Fig. 1.8: Erosion induced due to cavitation (a) schematic of sac-type nozzle, (b) damaged needle due to erosion, and (c) damaged sac volume (Piehl and Bravo 2018).

1.3 Hydrofoil and Injector Nozzle Terminology

A typical shape of a hydrofoil, which resembles the shape of propeller, is shown in Fig. 1.9. Here the upper and lower surfaces of the hydrofoil are called as the suction side and the pressure side, respectively. The meeting points of pressure and suction sides at the front and back are termed as the leading and the trailing edge, respectively. The length of the straight line connecting the leading and trailing edges is termed as chord length, denoted by c. The curve which is the locus of the mid-points between the suction and the pressure surfaces is called as the camber line. The geometric angle between the relative velocity vector of the flow at the leading edge and the hydrofoil chord line is referred as the angle of attack (α) (Muratoglu and Ishak Yuce 2015). The hydrofoils are classified by the NACA standards, such as four-digit hydrofoils, NACA0006, NACA0009, NACA0012, NACA0015, NACA4418, NACA4412 etc, as shown in Fig. 1.10. Here, first digit describes the maximum percentage of the camber, second digit describes the distance of maximum camber from the hydrofoil leading edge in terms of percent of the chord, and the last two digits describe the maximum thickness as percent of the chord. For example, the NACA 4418 means a hydrofoil which has a maximum camber of 4% located 40% (0.4 chords) from the leading edge with a maximum thickness of 18% of the chord.

Injector nozzle is basically a fine sprayer consisting of a single hole or multiple holes through which fuel is injected at high pressure into an engine for fuel atomization (Mohan et al. 2017). The basic geometry of a Spray C injector nozzle is shown in Fig. 1.11. It mainly consists of a needle, injector body, sac, and nozzle hole. Here, a needle is used to close and open the valves for the proper amount of fuel injection. A seat is made of a single cone at the end of the needle valve that intersects with a conical surface on the injector body. The inner part of the nozzle that contains the injector needle valve, spring, and a thread is known as the injector body. A tiny cavity in the bottom of injector that maintains a small amount of fuel in the tip is named as sac, that helps to cool the nozzle and preserve the longevity. All these nozzle parameters affect the combustion characteristics of the engine, as well as the stability of the emissions, performance, and mechanical durability over the lifetime. Due to the complex geometry of the nozzle and the number of parameters on which the flow through the nozzle depends, it is of utmost importance to validate the numerical simulation using experimental data. A reliable source of such data is ECN, which is an international collaborative network between different universities and industries. ECN has experimental data for some standard nozzle which it categorizes depending on its geometry as non-cavitating (Spray A), mildly

cavitating (Spray B), and cavitating (Spray C). Our study will be focusing on cavitation in Spray C type nozzle.

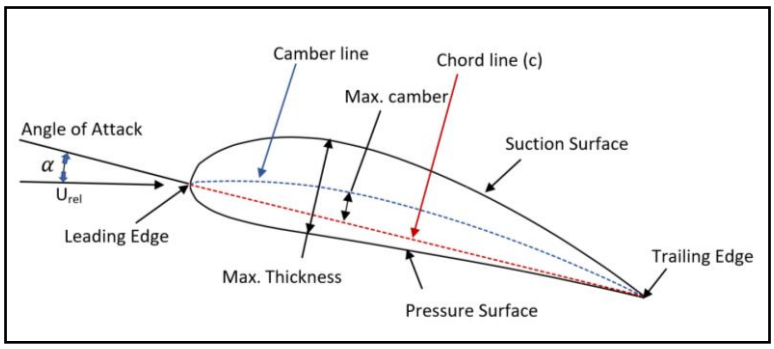

Fig. 1.9. Hydrofoil nomenclature.

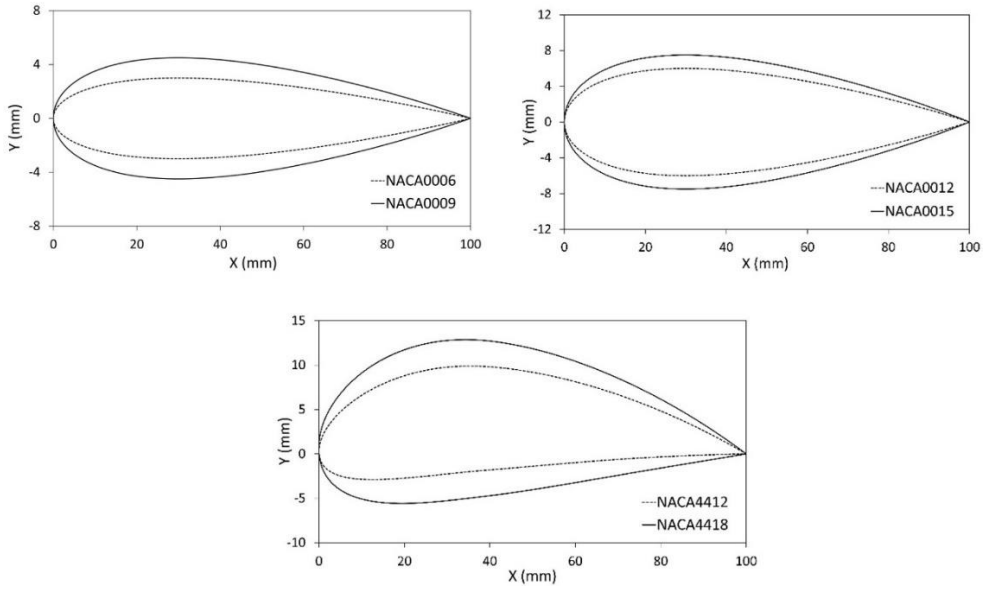

Fig. 1.10. 2D Profiles of different four-digit NACA hydrofoils.

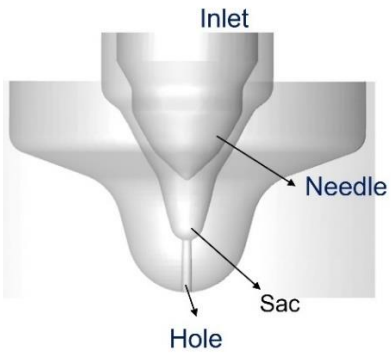

Fig. 1.11. Spray C injector nozzle.

1.4 Outline of the Thesis

This thesis has been organized into seven chapters. Chapter 1 covers the fundamentals of cavitation, types of cavitation, and motivation of the work. Chapter 2 presents the literature review which includes both the experimental and numerical work done on cavitating flows on hydrofoils, fluid-structure-interaction (FSI) on cavitating hydrofoils, and cavitation in injector nozzles. Chapter 3 describes the mathematical formulation which includes governing equations of mixture multiphase model, turbulence models, cavitation models, equations for structural analysis along with the material properties and solution methods. It also includes the assessment of different turbulence models and cavitation models on the cavitating hydrofoils. Chapter 4 presents the effect of Reynolds number on the cavitating hydrofoil, and the performance comparison of non-cavitating and cavitating hydrofoil at different angles of attack. Chapter 5 discuss the numerical investigation of fluid-structure-investigation (FSI) on NACA4418 and MHKF-180 hydrofoils at various angles and at different cavitation numbers. Chapter 6 explains the numerical study of cavitating flow in Spray C injector nozzle using conventional and alternate fuel. Finally, Chapter 7 highlights the conclusion of the present work, suggestions for future research work, followed by the list of publications.

Chapter 2

LITERATURE REVIEW

In line with the objectives of our work, in this chapter a detailed literature review containing experimental and numerical work is presented.

2.1 Cavitation on Hydrofoils

The turbulent cavitation flows are complex fluid dynamics problems, specifically unstable cloud cavitation observed on hydrofoils. This cavitation can cause strong hydrofoil vibrations, leading to solid structure erosion. Therefore, it is required to predict this unstable behaviour during the design stage only for the safe operation of hydraulic components like turbine blades, pumps, and injector nozzles. In past, several studies were carried out to analyse the effects of cavitation on hydrofoils, some were based on the analytical techniques, while others were based on the experimental observations and numerical simulations. Wu (1953) formulated the theory of finite span using lifting line theory to calculate the lift and drag force on the hydrofoil moving with constant velocity inside the incompressible and nonviscous liquid at a fixed depth. Fabula (1962) calculated the lift and drag force on the cavitating hydrofoil in steady incompressible flow as a function of cavitation number by applying the thin-airfoil theory and by conducting the experiment. They found good agreement between experimental and theoretical values. Woods (1964) extended the thin-airfoil theory to study the unsteady behaviour of cavitating and supercavitating flow on the two-dimensional hydrofoil and symmetrical wedge. Furuya (1975) also analysed the supercavitating hydrofoil, operating in the free surface to determine the gravity effect using three-dimensional non-linear free streamline theory and found that the shape of the cavity does not depend much on the gravity.

While some aspects of cavitation were successfully captured by the thin-airfoil theory, there was a need to further improve the understanding of cavitating flows, specifically in turbulent flows. For this purpose, Kermeen (1956) performed an experiment in high-speed water tunnel on 3-D NACA4412 hydrofoil and modified circular arc, flat plate hydrofoil named Walchner profile 7. Lift force, pitching moment and drag force were calculated for both non-cavitating and cavitating flow. Lohrberg et al. (2002) performed numerical simulation on the cascade of two-dimensional hydrofoils with a semi-circular nose using the RNG $k-\epsilon$ turbulence model. They found cloud cavitation on the topmost hydrofoil of the cascade while on the remaining two hydrofoils the sheet cavitation was observed. Through their numerical

results, they had been able to determine the two dominant frequencies and their dependence on the cavitation number. These results were then complemented by the experiment that they conducted in a water tunnel. Billet and Holl (1981) conducted experiments on hydrofoil families consisting of NACA0015 and a cambered (asymmetrical about chord line) NACA0010. Through these experiments, they demonstrated the existence of other types of cavitation, like bubble ring cavitation, traveling cavitation, tip-vortex cavitation, and sheet cavitation. Kubota et al. (1992) studied two-dimensional NACA0015 for experimental and numerical simulation at 8◦ and 20◦ angles of attack to develop Bubble Two-Phase Flow (BTF) model to understand the interaction between cavitation bubbles and viscous effects including large scale vortices. Kinnas and Fine (1993) analysed partial cavitation on 2D and 3D NACA16006 hydrofoils using BTF model and non-linear boundary element method (BEM) for two different cases. In the first case, length of cavity was determined for the known cavitation number while for the second case cavitation number was computed for the known cavity length. Comparing both models, they found that the BTF model has better convergence than the velocity-based BEM method.

It is evident from the above literature that with the increasing application of Computational Fluid Dynamics (CFD), different numerical tools can generate flow predictions precisely for practical problems. Therefore, researchers are moving from experiments to CFD. There are several reasons for use of CFD, it provides a cost-effective and time-saving way to simulate the complex fluid flow problems without conducting expensive experiments. CFD simulations can run much faster than experiments, allowing engineers to quickly evaluate multiple designs and optimize their performance. Moreover, CFD can be used to simulate a wide range of fluid flow problems, including complex geometries and multiphase systems. The CFD is required to accurately predict such flows, which depends on the turbulence model and cavitation model.

Many numerical studies have studied the effect of turbulence models on unsteady cavitating flows. Bensow (2011) numerically studied the unsteady cavitating flow on the Delft Twist 11 foil using Large Eddy Simulation (LES), Detached Eddy Simulation (DES), Reynolds-Averaged Navier Stokes (RANS) model. They concluded that the LES and DES were able to capture unsteady cavitation and vapor shedding more accurately as compared to RANS model. Similarly, Sedlar et al. (2016) studied unsteady cavitating flow around the NACA2412 hydrofoil using LES, Scale Adaptive Simulation (SAS) and DES model. They found that LES overestimated the dominant frequency of the oscillating cavitating flows more

than DES and SAS models. However, LES was able to describe vortex structure more accurately. Kinzel et al. (2007) used DES and the standard $k-\epsilon$ RANS model to study ventilated cavitation. They found that DES captures a broader spectrum of turbulent scales and cavitation than another model. Ji et al. (2015) employed the LES, Partially Averaged Navier Stokes (PANS), and RANS model on the cavitating twisted hydrofoil and compared the results with the experimental data. They pointed out that PANS and LES could better predict the primary and secondary cavity shedding patterns, while the RANS model yield almost steady flow with the constant shape of vapor cavities.

Even though the scale-resolving systems (LES and DES) have shown themselves to be superior, it has been claimed that their high computational resource requirement make them impracticable in high-volume industrial settings. RANS models are still the most often used technique in industrial CFD for hydraulic systems and machinery. Despite this the influence of different RANS models on the cavitating flow is sparse. For example, Deng et al. (2020) investigated the influence of different turbulence models (Std $k-\epsilon$, RNG $k-\epsilon$, and SST k-ω) on the thermosensitive cavitating flow. The RNG $k-\epsilon$ model was more accurate than other models for cavitating flow at different temperatures. Goncalvès and Charrière (2014) simulated the cavitating flow in a Venturi test section using four distinct RANS models. They found that the SST model best agrees with the experimental data. Nur-E-Mostafa et al. (2012) employed three RANS models i.e., Spalart-Allmaras (SA), RNG $k-\epsilon$, and SST $k-\omega$ to capture the turbulent boundary layer on CAV2003 hydrofoil using enhanced wall treatment. With enhanced wall treatment, they concluded that Spalart-Allmaras and RNG k-ϵ computed the lift coefficient accurately. Ahn et al. (2018) modified the RNG k-ϵ turbulence model to study the effect of turbulent viscosity on the cavitation phenomenon on 3D NACA0015 hydrofoil. They found that modified RNG model agreed well with experimental results compared to the standard model. Similar conclusions were drawn by Dular et al. (2005) that the standard RNG model overpredicts the turbulent viscosity and gives a cavity length half of the experimental one. Chebli et al. (2021) analyzed the cloud cavitation on 2D NACA66 hydrofoil using standard and modified RNG $k-\epsilon$, SST $k-\omega$ turbulence models. They found that $k-\epsilon$ model was unable to capture the unsteady cavitation as compared to modified models. Li et al. (2009) used modified RNG $\kappa-\epsilon$, SST $k-\omega$ turbulence models around 2D and 3D cavitating NACA0015 hydrofoils and compared the results with the experimental data. They remarked that modified SST model improves the prediction of essential features like shedding of cloud cavity microstructure and re-entrant jets. Similarly, Hong et al. (2017) performed numerical

simulation on 2D Clark-Y cavitating hydrofoil at an angle of attack $\alpha = 8^0$ using modified SST $\kappa - \omega$ turbulence models and found that this model can predict the formation, breakup, shedding, and collapse of sheet and cloud cavity.

2.2 Fluid Structure Interaction on Hydrofoils

In addition to hydrodynamic assessment of hydrofoils, it is also important to analyze them for structural response as during operation they are subjected to stress, strain, and unexpected loading that may cause structural deformations and oscillations. These deformations can be quite small or large depending upon the hydrofoil material properties and the flow characteristics. For underwater hydrofoils, the added fluid mass and hydrodynamic damping play a crucial role in the structural response. Also, as mentioned earlier, due to their typical shape, they can cavitate and forms vapor cavities. The collapse of these cavities may induce strong vibrations, noise, and instabilities in the hydrofoil structures. These effects can be studied and analyzed using fluid-structure-interaction (FSI) (Sedlar et al. 2011; Čupr et al. 2019).

In the past, several experimental and numerical studies have been conducted on metallic (rigid) and composite (flexible) hydrofoils to examine the effect of cavitation on the structural vibration. Traditionally hydrofoils are manufactured using metals, particularly aluminium and stainless steel. These metals provide the advantage of being homogeneous and isotropic, whereas the composite materials being lighter in weight are mostly used for aeronautical applications (Zarruk et al. 2014). Ausoni et al. (2007) carried out FSI experiment on truncated NACA0009 stainless steel hydrofoil and investigated the effect of cavitation within the core of Karman vortices. They found that there was a significant increase in the vibration amplitude and vortex shedding frequency due to cavitation, which may activate or delay the hydrofoil resonance. Young (2007) coupled the boundary element method (BEM) and finite element method (FEM) to investigate the performance of cavitating aluminum propeller blade 4148 in terms of added mass and deformation. They found that the added fluid mass caused a decrease in the fundamental frequency of blade and an increase in the blade stress, displacement, and oscillations. Young (2008) extended the BEM and FEM coupled approach on the flexible composite blade in subcavitating and cavitating conditions. They concluded that these blades may experience a resonant vibration and fatigue problems due to the added fluid mass.

Ducoin et al. (2010b) conducted experimental and numerical study to analyze the hydroelastic behavior of flexible POM polyacetate cantilevered hydrofoil in turbulent

subcavitating and cavitating flows. They found that elastic deformation resulted in an increase of effective angle of attack and decrease in lift to drag ratio. Ducoin et al. (2012b) extended their FSI experiment on NACA66312 flexible hydrofoil at different pitching velocities for both cavitating and non-cavitating conditions. They found that for non-cavitating condition, the hydrofoil vibration increases due to vortex shedding, whereas for the cavitating condition, the vibration increases due to instabilities caused by the vapor bubbles. Similarly, Ducoin et al. (2012a) performed experiment on rigid and flexible NACA66312 hydrofoil to study the effect of vortex shedding and laminar separation bubble (LSB) on the excitation of the hydrofoil. They found that LSB triggers the vibration, causing higher vortex shedding frequencies in flexible hydrofoil as compared to rigid hydrofoil. Akcabay and Young (2014) analyzed, experimentally and numerically, the cavitation-induced vibration of rigid and flexible NACA66 hydrofoil at 8^o angle of attack. They observed the frequency modulation in the flexible hydrofoil due to unsteady fluid-induced forces. Liaghat (2014) carried the experiment and two-way FSI numerical simulation on the hydrofoil structure to predict the vibration amplitudes and damping effect caused by the water added mass and computed the natural frequency and damping coefficient for the range of water velocity. They found that the damping ratio has a linear relation with fluid velocity while response frequency decreases with increased fluid velocity. Benaouicha et al. (2018) performed a numerical simulation on rectangular cantilevered NACA0015 flexible (polyacetate) hydrofoil at 8^o angle of attack. They concluded that hydrodynamic loading induces the bending displacement of hydrofoil. A summary of the literature related to the FSI study of hydrofoils is presented in Table 1.

In the above studies clearly, a large number of experimental and numerical works have been reported related to flow around the NACA hydrofoils. It should be noted that the NACA hydrofoils has different profiles as discussed in section 1.4. Among these profiles, NACA44 series has large leading radius which provides the advantage of good cavitation resistance (Phillips et al. 2012). While its sharp trailing edge leads to certain disadvantages when put in application like low structural efficiency, susceptibility to singing due to flexural vibration of the trailing edge. These vibrations are caused due to formation of vortices. These vortices are formed at a dominant frequency depending on water velocity and recirculation in the flow region. When the frequency of these vortex shedding matches the flexural resonance frequency of the hydrofoil the highly oscillating vibration occurs, named as singing Blake et al. (1976). To minimize these problems, recently researchers at Sandia National Laboratories developed Marine and Hydrokinetic (MHKF) hydrofoils by providing finite thickness to the trailing edge

of different hydrofoils of the NACA44 series. They assessed the performance of MHKF at a different angle of attack for non-cavitating flow using XFOIL and unsteady RANS solver named as OVERFLOW and found that hydrodynamic performance of MHKF hydrofoil is higher than NACA4418 for marine applications (Shiu et al. 2012). However, about MHKF, other relevant questions have not been reported yet, like how the hydrodynamic and structural performance of MHKF-180 is different from NACA4418 under cavitating conditions for various cavitation numbers and at a different angle of attack.

As evident from the literature presented, for underwater applications, the structural response of hydrofoils is expected to be different than air, which could further exacerbate under cavitation. Therefore, to analyze and understand the complex behavior of the interaction of structure with surrounding fluid under cavitating condition of MHKF-180, the three-dimensional cantilevered hydrofoils made of stainless-steel are studied numerically. The results of MHKF-180 are compared with the NACA4418 hydrofoil.

Table 2.1. Summary of cavitating flow studies on various hydrofoils

Literature	**Hydrofoil Material**	**Numerical/ Experimental**	**Objectives**	**Findings**
Ducoin et al. (2010b)	Stainless Steel and POM	Both	Studied hydroelastic response of cantilevered cavitating hydrofoil (NACA66)	Angle of attack increases for the POM as compared to steel, resulting in longer cavities, higher coefficient of lift, drag and lower l/d ratio.
Brandner and Pearce (2012)	Aluminium (Al) and Stainless Steel (SS)	Experiment	Investigated the hydroelastic behaviour of Al and SS hydrofoils (NACA0009) at different Reynolds numbers	Forces and deflections were found to be stable up to stall condition of hydrofoil.
De La Torre et al. (2013)	Stainless Steel	Experiment	Studied the effect of sheet cavitation and supercavitation the hydrofoil (NACA0009)	Minimum added mass effect was observed for supercavitation
Ducoin and Young (2013)	Stainless Steel and POM	Both	Studied the stability and hydroelastic response of hydrofoil (NACA66) in viscous flow.	The twisting moment limits due to viscous effect producing large scale flow separation.
Zarruk et al. (2014)	Stainless steel (SS), Aluminium	Experiment	Investigation of hydroelastic behaviour of different material	Composite material hydrofoil experiences larger bending and

	(AL), composites (CFRP)		hydrofoils (NACA0009).	twisting deformation than SS and Al hydrofoils.
Liu et al. (2018)	Stainless Steel	Both	The possibility of blade resonance condition is studied on the blade using Rotor Stator Interaction (RSI) phenomenon and acoustic FSI method.	Large volume of cavitation on the blade increases the natural frequencies by 10-15% resulting in resonance excitation.
Hao et al. (2019)	Aluminium, stainless steel, and epoxy coated stainless steel	Experiment	Investigated the effect of hydrofoil surface material on the cavitating flow.	Both steel and epoxy coated hydrofoils performs better than aluminium under cavitation.
Majnarić and Zamarin (2020)	Stainless Steel, Aluminium and Composite	Numerical	Studied the structural response of fully and partially submerged hydrofoils at different α and for different velocities.	For fully submerged condition Al and SS shows similar hydrodynamic behaviour. Composites found to withstand larger loads.
Geng et al. (2020)	Stainless Steel and Copper	Numerical	Investigated the effect of unsteady cloud cavitation on the erosion of hydrofoil through energy balance approach.	The driving pressure selection in the cavitation model has a significant role on the distribution and impact of cavity collapse.
Smith et al. (2020)	Stainless Steel	Experiment	Study of tip deformation and cavitation behaviour of NACA0009 hydrofoil for cloud, sheet and supercavitating regimes.	Oscillation frequencies found to be independent of cavitation number for lower value of σ (0.3-0.6). Lock-in occur at σ (0.65-0.75).
Ming et al. (2021)	Structural Steel	Numerical	Studied the influence of modified trailing edge on the added damping of Kaplan turbine.	Damping for Donaldson trailing edge is relatively more as compared to blunt trailing edge.
Giovannetti et al. (2022)	Composite (ZP0082)	Both	FSI study on hydrofoil (NACRA17 Z-foil).	Maximum deflection of foil is observed when 24% of span is covered with water.

2.3 Cavitation in Injector Nozzle

Cavitation in nozzle has been an extensive research topic for a few decades (Chen and Heister 1995; Arcoumanis et al. 1999, 2002; Schmidt et al. 1997). In certain regions, whenever the

local pressure of flowing liquid falls below the vapor pressure of the fuel concerned, the phenomenon of cavitation occurs (Saha 2014). The cavitation may affect the fuel spray characteristics, discharge coefficient, atomization process, and fluid flow field boundary conditions. Ranz (1958) carried out the primary experimental work on cavitating nozzles with the liquid jet spray system. The focus of this study was on the breaking of jet due to local inertial stresses and its effect on spray characteristics in front of an orifice. Dabiri et al. (2007) performed a numerical simulation of two-phase incompressible flow to discover the potential location of cavitation by comparing the conditions based on the total stress criterion and pressure criterion in an axis-symmetric orifice using the finite volume method. They observed the substantial cavitation region in the flow field for the total-stress criterion as compared to the pressure criterion. The accuracy of numerical results for multiphase flow in nozzles also depend on the type of cavitation model used. Saha and Li (2015) developed a cavitation model and tested its performance compared to two already existing cavitating models: Schnerr-Sauer and Zwart-Gerber-Belamri in Winklhofer et al. (2001). The model proposed by Saha and Li (2015) worked better than the existing models in ANSYS Fluent when a single-fluid or mixture multiphase approach was used. Battistoni et al. (2014) compared the prediction capabilities of two different cavitation models in a simple nozzle, one is a homogeneous mixture model, and another is the multi-fluid non-homogeneous model. They found that the quantitatively mixture model overpredicts the void fraction as compared to multi-fluid model when both results were compared with the experimental work.

The cavitation in injector nozzles is sensitive to geometric features such as inlet corner radius, degree of taper, surface roughness, etc. (Schmidt et al. 1997, 2014; Duke et al. 2014) performed the experimental and numerical study on different cavitating and non-cavitating injector nozzles like sharp-edged nozzle, round tip nozzle, and tapered nozzle hole as shown in Fig 1.12. They found that sharp inlet nozzles initiate the cavitation, whereas rounded nozzles delay the cavitation due to reduced flow separation. Tapered nozzles were found effective for suppressing the cavitation. Örley et al. (2017) numerically simulated the fully compressible two-phase homogeneous mixture model to examine the cavitation and turbulent scale effects in a nine-hole common rail-diesel injector using an implicit LES turbulence model. Small-scale turbulence was detected during opening and closing, and during the injection phase, a large vortical structure was formed. Moreover, vortex cavitation was observed at the outlet due to the tapered shape of nozzle holes. Chaves et al. (2010) conducted an experiment on transparent nozzles of different sizes to analyse the cavitation for sharp, tapered, and rough

surface geometries. A modified laser-two-focus velocimeter was used to measure flow velocity and discharge. They observed that sharp geometries are more prone to cavitation than tapered or rounded nozzles due to sudden flow separation. Additionally, they concluded that rough surfaces are more susceptible to cavitation wear due to the availability of more sites for bubble formation. These bubbles rapidly collapse, producing shock waves that are strong enough to generate consequential damage to the surface like pitting, erosion, etc. Andriotis et al. (2008) studied the origin, formation, development, lifetime, and influence of string cavitation on a three-dimensional transparent acrylic replica of the five-hole nozzle of vortex type. Their crucial observation was that there is an uneven dispersion of liquid due to string cavitation, and to prevent the sudden pressure drop tapered holes acts as a better alternative.

Sforzo et al. (2018) performed an experimental study on Engine Combustion Network (ECN) Spray C and Spray D diesel injectors using the optical and x-ray diagnostic technique to study the effect of geometrical features on cavitation formation. They observed the asymmetric sheath of fuel vapor in Spray C, which affects the fuel spray structure near the nozzle exit. In contrast, no cavitation was observed in Spray D. Similarly, Maes et al. (2020) performed experiments on Spray C and Spray D to study the effect of cavitation on spray penetration, combustion characteristics, and soot formation of n-dodecane fuel in the constant pressure vessel of multiple combustion facilities. They concluded that soot formation was sensitive to the main species of the ambient gas, i.e., carbon dioxide, water, and nitrogen, in the presence of constant oxygen. Tekawade et al. (2020) performed an experiment on a Spray C nozzle to study the 3D flow field inside the diesel injector using a synchrotron X-ray source. They found strong flow separation and vapor-filled cavities related to the nozzle's asymmetric inlet corner.

Pollutant emissions control in the automotive industry is becoming increasingly stringent, prompting the development of various innovative technologies in recent years. Current advanced aftertreatment systems are effective in reducing engine exhaust emissions in compression ignition engines, but their complexity and cost rises. Therefore, more focus is towards the use of alternative fuels in injector nozzles to minimize the NOx and soot emissions while maintaining the combustion efficiency. Among, all the synthetic fuels available nowadays, Oxymethylene ether (OME_n) is a considered to be a promising synthetic fuel that is produced from the renewable resources, making it an environmentally friendly alternative to conventional fuels. Many studies are available in the literature that studied the behaviour and characteristics of OME_n fuel on the NOx and soot emission in the recent years (Kulkarni et al.

2020; Pastor et al. 2020; Ferraro et al. 2021). However, to the authors knowledge, there are no studies that analysed the cavitation behaviour of OME_n in Spray C injector nozzle. Therefore, in the present work the cavitation characteristics of OME_3 fuel is compared with the conventional n-dodecane fuel in ECN Spray C nozzle using CONVERGE v3.0 code.

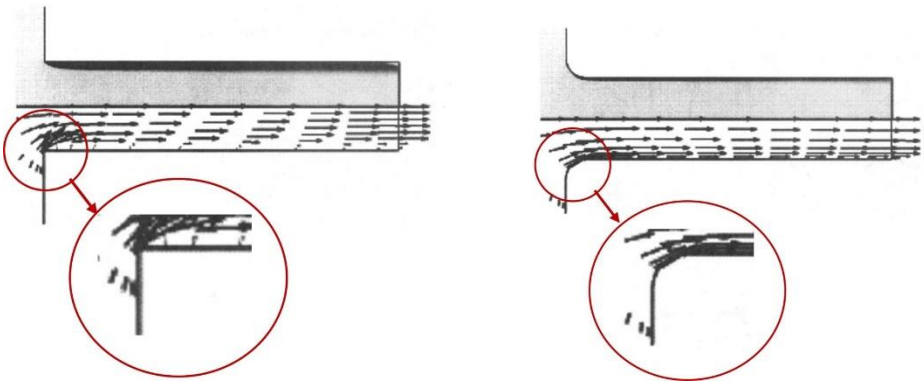

Fig. 2.1. Flow through sharp and round nozzle (Schmidt 1997).

2.4 Research Objectives

Based on the literature review presented above, the objectives of thesis are listed below:

(1) To assess the performance of different cavitation models and different turbulence models on the cavitating hydrofoils.

(2) To study the structural and hydrodynamic performance of 3D MHKF-180 and NACA4418 under cavitation using Fluid-Structure Interaction (FSI).

(3) To study the cavitation in Spray C injector nozzle using conventional and alternative fuel.

CHAPTER 3

GOVERNING EQUATIONS AND ASSESSMENT OF CAVITATION AND TURBULENCE MODELS ON CAVITATING HYDROFOILS

This chapter presents the model assumptions, governing equations, closure equations of mass source term, and turbulence models for cavitation on hydrofoils and in injector nozzles. The governing equations for the fluid structure interaction algorithm are also presented. Furthermore, the performance of four different turbulence models and two different cavitation models is compared with the available experimental data on 3D NACA4412 and Clark-y hydrofoils in the last section of this chapter.

The most common model used to solve the cavitating flow on hydrofoils is the homogeneous mixture model. There are two cavitation models available in ANSYS Fluent software i.e., Schnerr-Sauer model and Zwart-Gerber-Belamri model, that can be coupled with homogenous mixture model to calculate the vapor volume fraction. There are certain assumptions of homogeneous mixture model that are adopted in this study for cavitation on hydrofoils (Saha 2014).

1. The two-phase flow is isothermal.
2. The relative velocity between two-phases is assumed to be negligible with respect to mean flow velocity.
3. The cavitation model used in the study do not consider the existence of non-condensable gases. Therefore, fluid only consists of mixture of liquid and vapor such that:

$$\alpha_v + \alpha_l = 1 \, . \tag{3.1}$$

   where α_v and α_l are the volume fractions of vapor and liquid phase, respectively.
4. The Zwart-Gerber-Belamri cavitation model used in this thesis assumes the constant bubble size to calculate the total interphase mass transfer rate per unit volume.

3.1 Governing Equations

The governing equations for homogeneous mixture multiphase approach, involves solving the unsteady Reynolds averaged Navier-Stokes (URANS) equations using turbulence model.

$$\frac{\partial \rho_m}{\partial t} + \frac{\partial}{\partial x_j}\left(u_j \rho_m\right) = 0\,, \tag{3.2}$$

$$\frac{\partial}{\partial t}(\rho_m u_i) + \frac{\partial}{\partial x_j}\left(\rho_m u_i u_j\right) = -\frac{\partial p}{\partial x_i} + \frac{\partial}{\partial x_j}\left[\mu_{\text{eff}}\left(\frac{\partial u_i}{\partial x_j} + \frac{\partial u_j}{\partial x_i} - \frac{2}{3}\frac{\partial u_k}{\partial x_k}\delta_{ij}\right)\right], \tag{3.3}$$

where u_i is the Reynolds averaged velocity, p is the Reynolds averaged pressure, ρ_m is the fluid mixture density, and μ_{eff} is the effective viscosity. The mixture density and effective viscosity are defined as below:

$$\rho_m = \alpha_v \rho_v + (1 - \alpha_v)\rho_l, \tag{3.4}$$

$$\mu_{\text{eff}} = \mu + \mu_t\,. \tag{3.5}$$

Here α_v is the vapor volume fraction estimated with the help of cavitation model, ρ_v and ρ_l are the vapor and liquid density, respectively. μ is the molecular viscosity and μ_t is the turbulent eddy viscosity. μ_{t} in the above equation is estimated using different turbulence models. For example

$$\mu_t = \rho_m C_\mu \frac{k^2}{\epsilon}, \qquad (k-\epsilon \text{ model}) \tag{3.6}$$

$$\mu_t = \rho_m \alpha^* \frac{\kappa}{\omega}, \qquad (k-\omega \text{ model}) \tag{3.7}$$

where C_μ and α^* are the model constants for different turbulence models, k is turbulent kinetic energy, ϵ is the dissipation-rate of k, and ω is specific turbulent dissipation rate.

3.2 Turbulence Models

For turbulent cavitating flows, to determine the μ_t, there are different $k-\epsilon$ and k-ω turbulence models available. In last section of this chapter the comparison has been made on cavitating hydrofoils with four different turbulence models, (a) Standard $k-\epsilon$ model, (b) Re-Normalisation (RNG) $k-\epsilon$, (c) Realizable $k-\epsilon$ models, and (d) Shear-stress transport (SST) k-ω models. Among all four turbulence models for cavitating hydrofoils, the Realizable $k-\epsilon$ model has been found to predict the dissipation rate distribution more accurately and gives a better prediction of boundary layer characteristics in recirculation and adverse pressure gradient regions as it dynamically estimates the C_μ to satisfy the physics of turbulent flows (Shaheed et al. 2019). Therefore, Realizable $k-\epsilon$ model has been used for studying cavitating flows on hydrofoils. The turbulence modelling approach adopted with homogeneous mixture multiphase model are discussed here followed by discussion on near wall treatments.

3.2.1 Standard $k-\epsilon$ Model

This is the simplest two-equation model in which two separate transport equations are solved. The transport equations for turbulent kinetic energy (k) and its dissipation rate (ϵ) for Std. $k-\epsilon$ model are:

$$\frac{\partial}{\partial t}(\rho_m k) + \frac{\partial}{\partial x_i}(\rho_m k u_i) = \frac{\partial}{\partial x_j}\left[\left(\mu + \frac{\mu_t}{\sigma_k}\right)\frac{\partial k}{\partial x_j}\right] + G_k - \rho_m \epsilon - Y_M, \quad (3.8)$$

$$\frac{\partial}{\partial t}(\rho_m \epsilon) + \frac{\partial}{\partial x_i}(\rho_m \epsilon u_i) = \frac{\partial}{\partial x_j}\left[\left(\mu + \frac{\mu_t}{\sigma_\epsilon}\right)\frac{\partial \epsilon}{\partial x_j}\right] + C_{1\epsilon}\frac{\epsilon}{k}G_k - \rho_m C_{2\epsilon}\frac{\epsilon^2}{k}, \quad (3.9)$$

where, $G_k = \overline{u_i' u_j'}\frac{\partial u_j}{\partial x_i}$ corresponds to the production of turbulent kinetic energy (k) due to mean velocity gradients, $Y_M = 2\rho\epsilon M_t^2$ is the contribution of the fluctuating dilatation in compressible turbulence to the overall dissipation rate with $M_t^2 = (\kappa/a^2)$ and $a = \sqrt{\gamma RT}$. $C_{1\epsilon}$ and $C_{2\epsilon}$ are the constants. σ_k and σ_ϵ are the turbulent Prandtl numbers for k and ϵ, respectively. The model constants $C_{1\epsilon}, C_{2\epsilon}, C_\mu, \sigma_k$, and σ_ϵ values are :

$$C_{1\epsilon} = 1.44;\ C_{2\epsilon} = 1.92;\ C_\mu = 0.09;\ \sigma_k = 1.0;\ \sigma_\epsilon = 1.3.$$

3.2.2 RNG k-ϵ Model

In contrast to the standard k-ϵ model, which estimates eddy viscosity on the basis of a single turbulence length scale, the RNG k-ϵ model seeks to account for the impacts of different flow-scales by using the production term. In RNG k-ϵ model, the model equations are:

$$\frac{\partial}{\partial t}(\rho_m k) + \frac{\partial}{\partial x_j}(\rho_m k u_j) = \frac{\partial}{\partial x_j}\left[\alpha_k(\mu + \mu_t)\frac{\partial k}{\partial x_j}\right] + G_k - \rho_m \epsilon - Y_M, \quad (3.10)$$

$$\frac{\partial}{\partial t}(\rho_m \epsilon) + \frac{\partial}{\partial x_j}(\rho_m \epsilon u_j) = \frac{\partial}{\partial x_j}\left[\alpha_\epsilon(\mu + \mu_t)\frac{\partial \epsilon}{\partial x_j}\right] + C_{1\epsilon}\frac{\epsilon}{k}G_k - \rho_m C_{2\epsilon}\frac{\epsilon^2}{k} - R_\epsilon, \quad (3.11)$$

where R_ϵ is a special term in the model accounts for low, medium, and high strain rates. The quantities α_k and α_ϵ are the inverse effective Prandtl numbers for k and ϵ. The model constants for RNG $k-\epsilon$ model are:

$$C_{1\epsilon} = 1.42;\ C_{2\epsilon} = 1.68;\ C_\mu = 0.0845.$$

3.2.3 Realizable $k-\epsilon$ Model

This model does not assume C_μ as constant, it varies according to the flow field to satisfy the physics of turbulent flows. The Realizable $k-\epsilon$ model has the immediate advantage of more precisely predicting the spreading rate of both planar and round jets. It is also likely to

outperform other flow types such as rotation, boundary layers under high adverse pressure gradients, separation, and recirculation. The transport equations for Realizable $k-\epsilon$ turbulence model are:

$$\frac{\partial}{\partial t}(\rho_m k) + \frac{\partial}{\partial x_j}(\rho_m k u_j) = \frac{\partial}{\partial x_j}\left[\left(\mu + \frac{\mu_t}{\sigma_k}\right)\frac{\partial k}{\partial x_j}\right] + G_k - \rho_m \epsilon - Y_{M,} \qquad (3.12)$$

$$\frac{\partial}{\partial t}(\rho_m \epsilon) + \frac{\partial}{\partial x_j}(\rho_m \epsilon u_j) = \frac{\partial}{\partial x_j}\left[(\mu + \mu_t)\frac{\partial \epsilon}{\partial x_j}\right] + \rho C_1 S\epsilon - \rho_m C_2 \frac{\epsilon^2}{k+\sqrt{\nu\epsilon}}, \quad (3.13)$$

where C_1 = max [0.43, $\frac{\eta}{\eta+5}$], $\eta = S\frac{k}{\epsilon}$, $S = \sqrt{2S_{ij}S_{ij}}$. S is the modulus of the mean rate of strain tensor. The model constants for Realizable κ-ϵ model are:

$$C_2 = 1.9;\ \sigma_k = 1.0;\ \sigma_\epsilon = 1.2.$$

3.2.4 SST $k-\omega$ Model

This model uses $k-\omega$ model in the boundary layer till viscous sub-layer and $k-\epsilon$ approach away from the wall to generate a hybrid and adaptable modelling solution. For shear-stress transport (SST $k-\omega$) model, the turbulent kinetic energy (k), and the specific turbulent dissipation rate (ω) are determined by:

$$\frac{\partial}{\partial t}(\rho_m k) + \frac{\partial}{\partial x_j}(\rho_m k u_j) = \frac{\partial}{\partial x_j}\left[\left(\mu + \frac{\mu_t}{\sigma_k}\right)\frac{\partial k}{\partial x_j}\right] + G_k - Y_{k,} \qquad (3.14)$$

$$\frac{\partial}{\partial t}(\rho_m \omega) + \frac{\partial}{\partial x_j}(\rho_m \omega u_j) = \frac{\partial}{\partial x_j}\left[\left(\mu + \frac{\mu_t}{\sigma_\omega}\right)\frac{\partial \omega}{\partial x_j}\right] + G_\omega - Y_\omega + D_{\omega,} \quad (3.15)$$

where G_ω corresponds to the production of ω, Y_k and Y_ω represents dissipation of κ and ω due to turbulence and D_ω takes care about the cross-diffusion terms that helps SST $k-\omega$ model to work well in the near wall regions as well regions far away from the walls. The model constants are:

$$\sigma_{\kappa,1} = 1.176;\ \sigma_{\omega,1} = 2.0;\ \sigma_{\kappa,2} = 1.0;\ \sigma_{\omega,2} = 1.168.$$

$$a_1 = 0.31;\ \beta_{i,1} = 0.075;\ \beta_{i,2} = 0.0828.$$

Turbulent flows are mainly affected by the presence of walls, as walls are the primary source of mean vorticity and turbulence. Near-wall modelling using different wall functions has a considerable impact on the fidelity of the numerical solutions. A wall function is required to accurately predict the boundary layer. Boundary layer is a tiny zone near a wall with strong velocity gradient in the normal direction to the wall. A turbulent boundary layer consists of a

very thin viscous sub-layer near the wall, a transition layer (buffer zone), and the turbulent boundary layer (log-layer) as shown in Fig. 3.1. The viscous sub-layer needs to be captured with the help of wall function, for which the first cell (y) has to be located within the viscous sublayer. The distance of first cell y is measured in non-dimensional units, $y^+ \equiv \rho u_\tau y/\mu$. In the present work, for cavitating flow over hydrofoils, enhanced wall treatment has been used for near wall modelling and $y^+ < 4$ is maintained, which is inside the viscous sublayer (Pope 2000).

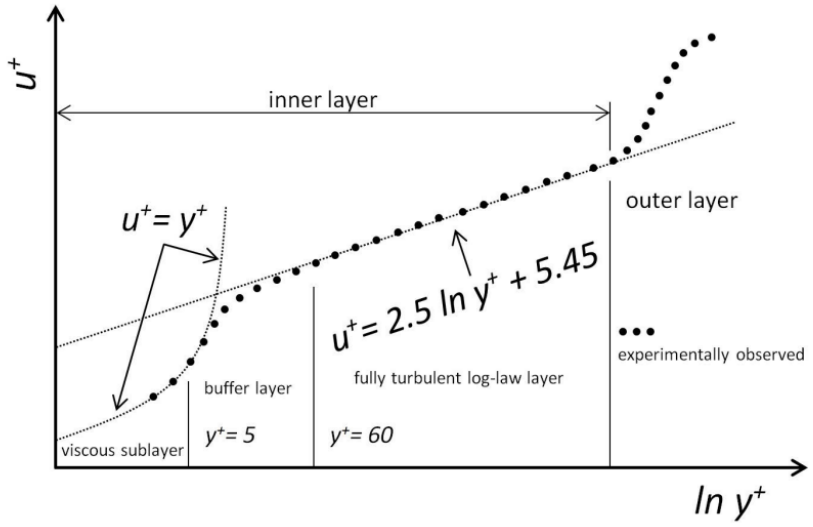

Fig. 3.1 The universal law of wall with dimensionless velocity (u^+) and dimensionless wall distance (y^+) (Pope 2000).

3.3 Cavitation Models

Cavitation takes place when a liquid at constant temperature subjected to decreasing pressure, such that the pressure falls below the vapor pressure of liquid. The cavitation model is required for solving the cavitating flows by determining the vapor volume fraction (α_v). The α_v on the hydrofoil given in the governing equation is defined as the ratio of vapor volume to the cell volume derived from vapor mass conservation equation:

$$\frac{\partial}{\partial t}(\alpha_v \rho_v) + \frac{\partial}{\partial x_j}\left(u_j \rho_v \alpha_v\right) = R_e - R_c, \tag{3.16}$$

where R_e and R_c are the evaporation and condensation source terms, respectively, which accounts for the mass transfer rate between the vapor and liquid phase. The vapor volume fraction can be determined using two cavitation models in ANSYS Fluent i.e., Schnerr-Sauer model and Zwart-Gerber-Belamri model. These cavitation models are based on the Rayleigh-Plesset equation, that describes the growth of single vapor bubble in a liquid. In practical

conditions it is assumed that there are plenty of nuclei of bubbles that are present during inception of cavitation. Therefore, our prime focus is on determining the bubble growth and collapse. In homogenous mixture model for the flowing fluid with no slip between liquid and bubble, the bubble dynamics equation can be derived from the generalised Rayleigh- Plesset equation as (Brennen 2005):

$$\frac{p_b - p}{\rho_l} = R_b \frac{d^2 R_b}{dt^2} + \frac{3}{2}\left(\frac{dR_b}{dt}\right)^2 + \frac{4\nu_l}{R_b}\frac{dR_b}{dt} + \frac{2S}{\rho_l R_b}, \tag{3.17}$$

where R_b is the bubble radius, p_b is the bubble surface pressure, ν_l is the kinematic viscosity of liquid. This equation further can be simplified to introduce the effect of bubble dynamics into cavitation model by neglecting higher order terms as:

$$\frac{dR_b}{dt} = \sqrt{\frac{2}{3}\frac{p_b - p}{\rho_l}}. \tag{3.18}$$

3.3.1 Schnerr-Sauer (SS) Model

This model is primarily dependent on numerical values of physical parameters rather than empirical constants. Schnerr-Sauer model does not consider the presence of non-condensable gases, and defines the vapor volume fraction (α_v) in terms of bubble density per cubic meter (n_o) and bubble radius (R_b) (Sauer and Schnerr 2000):

$$\alpha_v = \frac{n_o \frac{4}{3}\pi R_b^3}{1 + n_o \frac{4}{3}\pi R_b^3}, \tag{3.19}$$

The following are the vaporization and condensation source terms for Schnerr-Sauer model:

$$R_e = \frac{\rho_v \rho_l}{\rho_m}\frac{3\alpha_v(1-\alpha_v)}{R_b}\sqrt{\frac{2}{3}\frac{(p - p_{\text{sat}})}{\rho_l}}, \tag{3.20}$$

$$R_c = -\frac{\rho_v \rho_l}{\rho_m}\frac{3\alpha_v(1-\alpha_v)}{R_b}\sqrt{\frac{2}{3}\frac{(p_{\text{sat}} - p)}{\rho_l}}. \tag{3.21}$$

where R_b is the radius of bubble, p_{sat} is the saturation pressure of the liquid.

3.3.2 Zwart-Gerber-Belamri (ZGB) Model

This model assumes the constant bubble size to determine the total interphase mass transfer rate per unit volume and do not consider the presence of non-condensable gases (Saha 2014). For ZGB model, the vapor volume fraction (α_v) is connected to bubble radius and to the number of bubbles per unit volume (n_b) as (Zwart et al. 2004):

$$\alpha_v = n_b \frac{4}{3}\pi R_b^3, \tag{3.22}$$

In this model the vapor volume fraction (α_v) in the evaporation term is replaced with the product of nucleation site volume fraction (α_{nuc}) and remaining liquid volume fraction (1-α_v). The generalized vaporization and condensation source terms for ZGB model are expressed as:

$$R_e = F_{vap} \frac{3\alpha_{nuc}(1-\alpha_v)\,\rho_v}{R_b} \sqrt{\frac{2}{3}\frac{(p-p_{\text{sat}})}{\rho_l}}, \tag{3.23}$$

$$R_c = -F_{cond} \frac{3\alpha_v\,\rho_v}{R_b} \sqrt{\frac{2}{3}\frac{(p_{\text{sat}}-p)}{\rho_l}}, \tag{3.24}$$

F_{vap} and F_{cond} are the empirical coefficients of vaporization and condensation, respectively. The value for model constants are $R_b = 10^{-6}$ m, α_{nuc} = 0.0005, F_{vap} = 50 and F_{cond} = 0.01.

3.4 Fluid-Structure Model

The fluid-structure-interaction (FSI) can be categorized by the degree of coupling between the fluid and solid structure field depending upon how sensitive one field to a change in another field is. Based on this, FSI can be solved by two approaches: two-way coupling and one-way coupling. Solution of both the approaches depends on the partitioned method where separate solutions are prepared for different physical fields. One field has to be solved for fluid dynamics and the other for the structure dynamics. At the interface of fluid and solid, the information is exchanged which depends on the coupling method. For large deformation in the structure, the two-way coupling is preferred where the pressure field is transferred to the structure and structure displacement is transferred back to the fluid through remeshing. However, for small structural deformation, the one-way coupling is a suitable approach where pressure from fluid domain is transferred to the structure and subsequently equation of motion is solved (Monette et al. 2014; Huang et al. 2019). Since, for stainless-steel hydrofoil, the deformation is anticipated to be small, so one-way FSI approach is adopted in the present work.

In Fig. 3.2, the algorithm for solving one-way FSI coupling is demonstrated. The fluid field is initially solved until the convergence condition is met. Then at any required time the structural deformation is computed by applying the fluid pressure load on the structure. However, one-way coupling has some limitations like the fluid domain remains unaffected by the structural deformation, the one-way coupling should not be used if the hydrofoil is made of flexible material (Huang et al. 2019).

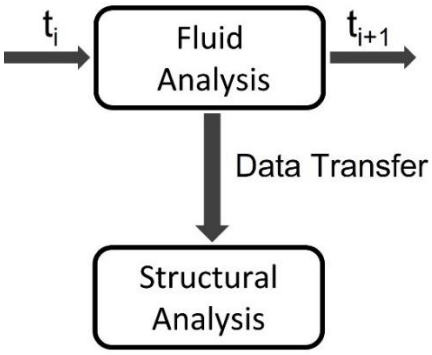

Fig. 3.2. Solution algorithm for one-way FSI coupling.

For fluid-structure interaction the governing equations used are based on the equation of motion. For structure equation of motion can be written as (Zeng et al. 2019b)

$$[M_s]\{\ddot{x}\} + [D_s]\{\dot{x}\} + [K_s]\{x\} = \{F(t)\}, \tag{3.25}$$

where $\{\ddot{x}\}$, $\{\dot{x}\}$ and $\{x\}$ are the nodal acceleration, velocity, and displacement vectors, respectively. The matrices $[M_s]$, $[D_s]$ and $[K_s]$ are the structural mass, damping and stiffness matrices, respectively. Since, the hydrofoil structure is immersed in the water, so to account the effect of water, the equation of motion is modified as (Zeng et al. 2019b).

$$[M_s + M_w]\{\ddot{x}\} + [D_s + D_w]\{\dot{x}\} + [K_s + K_w]\{x\} = 0, \tag{3.26}$$

where M_w is the added mass of still water, D_w is the damping due to viscous effect and K_w is the added stiffness due to compressibility effects of the fluid flow. It is evident from Eq. (3.26) that the frequency of oscillation will be affected by the mass of water. Therefore, in the presence of still water, the natural frequency of fully wetted hydrofoil is obtained as(Zeng et al. 2019a).

$$f_{nw} = \frac{1}{2\pi}\sqrt{\frac{(K_s+K_w)}{(M_s+M_w)}}. \tag{3.27}$$

3.5 Quantities of Interest

There are different non-dimensional parameters that are used to assess the performance of cavitating hydrofoils, like cavitation number (σ), pressure coefficient (C_p), coefficient of lift (C_l), coefficient of drag (C_d), and Strouhal number (St). The cavitation number (σ) is used as an indicator for the inception of cavitation on hydrofoil. The cavitation number is defined as the ratio of the difference of freestream pressure and vapor pressure to dynamic pressure, which is given by (Brennen 2005).

$$\sigma = \frac{p_\infty - p_v}{\frac{1}{2}\rho_l U_\infty^2}, \tag{3.40}$$

where p_∞ is the freestream pressure (Pa), p_v is the vapor pressure of liquid (Pa) at the reference temperature, ρ_l is density of liquid (kg/m^3), and U_∞ is the free stream velocity (m/s).

The pressure distribution on the surface of the hydrofoil is represented by its non-dimensional quantity, termed as pressure coefficient (C_p) which is defined as

$$C_p = \frac{p - p_\infty}{\frac{1}{2}\rho_l U_\infty^2}. \tag{3.41}$$

It should be noted that the hydrofoil with positive angle of attack, its upper surface owing to lower pressure, will have negative value of C_p, whereas its lower surface will have positive value of C_p. The lower pressure on the upper surface leads to the formation of vapor cavity, and this cavity is computed in terms of cavity length with the help of C_p curve. The length over which the pressure coefficient remains constant defines the cavity length. Further, the integration of pressure and shear stress distribution over the entire surface of the hydrofoil gives the total force, which can be resolved in perpendicular and parallel to freestream velocity. The force perpendicular to freestream velocity is called lift force (F_L) and the one parallel to freestream velocity is called drag force (F_D) (Anderson 2011). In non-dimensional form, these forces are represented by lift coefficient (C_l) and drag coefficient (C_d). The coefficients C_l and C_d are the crucial parameters for assessing the performance of hydrofoil, which are defined as

$$C_l = \frac{F_L}{\frac{1}{2}\rho_l A U_\infty^2}, \tag{3.42}$$

$$C_d = \frac{F_D}{\frac{1}{2}\rho_l A U_\infty^2}, \tag{3.43}$$

Since the flow behaviour past a hydrofoil is primarily unsteady, oscillating in nature due to formation and shedding of vortices downstream of the flow. Thus, such flows are not only characterized by the free-stream velocity and chord length of the hydrofoil but also by the frequency of vortex shedding. A non-dimensional number used for this purpose is called Strouhal number (*St*), which is defined as (Dular and Bachert 2009).

$$St = \frac{fc}{U_\infty}, \tag{3.44}$$

where *f* is the oscillating frequency (Hz), and c is the chord length (m).

3.6 Model Assessment

On the basis of mathematical formulation mentioned in the earlier sections of this chapter, in the present section, the assessment of four different turbulence models (Standard $k-\epsilon$, RNG $k-\epsilon$, Realizable $k-\epsilon$, and SST $k-\omega$) and two different cavitation models (Schnerr-Sauer and Zwart-Gerber-Belamri) is performed by comparing the numerical results with the available experimental data on 3D cavitating NACA4412 and Clark-y hydrofoils at $\alpha = 8^{o}$.

3.6.1 Computational Domain and Boundary Conditions

In this section, the NACA4412 hydrofoil is used for the analysis. The 2D profile of NACA4412 is shown in Fig 1.10 in chapter 1. The computational domain is displayed in Fig. 3.3. The dimensions in x, y, and z directions are 18c and 10c, and 1.135 c respectively, where c is the chord length of the hydrofoil which is kept as 0.1 m. These dimensions are used to minimize the impact of wall boundaries on the hydrofoil (Wu et al. 2011; Uddin and Karim 2017; Yu et al. 2019). The outlet is at 12c distance in the downstream direction of the leading edge, while the inlet is situated at 6c from the leading edge. Unstructured tetrahedral elements are used to create the computational mesh for the fluid zone, as shown in Fig. 3.4. Tetrahedral mesh is typically favorable for 3D curved bodies because the grids fit very well along the curves, providing better results (Wu 1953). The mesh around the hydrofoil is refined to capture the flow behaviour, and inflation layers are generated on the hydrofoil surface. To resolve the viscous sublayer on the hydrofoil, $y^{+} \leq 2$ is maintained. The first layer height of mesh is given as 0.007 mm, and the maximum inflation layers are 12 with a growth rate of 1.6. Fig. 3.5 depicts the y^{+} plot on NACA4412 hydrofoil. The average value of y^{+} on NACA4412 obtained is 1.1.

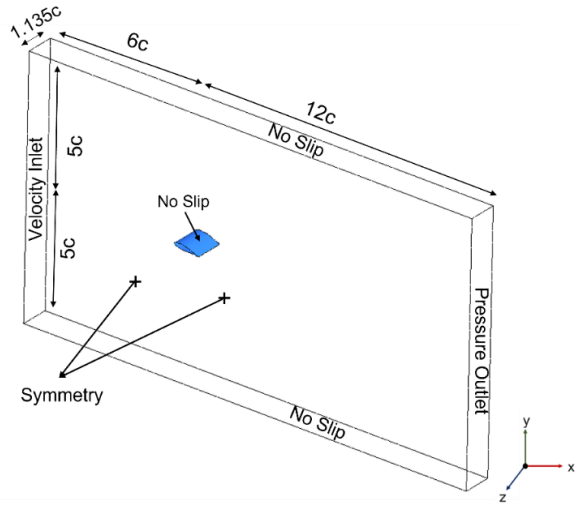

Fig. 3.3. Computational domain with boundary conditions.

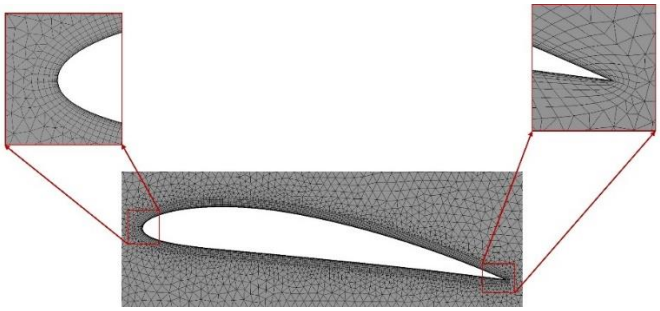

Fig.3.4. Meshing around NACA4412 hydrofoil.

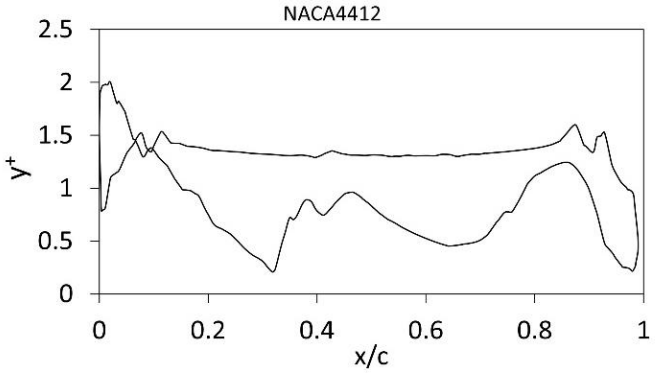

Fig. 3.5. y^+ distribution for the first layer of NACA4412 hydrofoil at $\alpha = 8^0$.

In the computational domain, the inlet is set as velocity inlet, and outlet is set as pressure outlet corresponding to cavitation number. The hydrofoil surfaces and upper and lower walls are kept as no slip condition. The front and back walls are set as symmetric boundary condition to avoid the wall effects on the hydrofoil as shown in Fig. 3.3. At the inlet the turbulent intensity is given as 5% (Ye et al. 2021; Zhang et al. 2021) which is reduced to 0.13% near the hydrofoil. Table 3.1 presents the reference values used for the simulation. For pressure and velocity

coupling, a coupled scheme is used whereas, PRESTO (Pressure Staggering Option) scheme is set for pressure. For volume fraction, momentum, turbulent kinetic energy, turbulent dissipation rate, the higher order scheme QUICK (Quadratic Upstream Interpolation for Convective Kinetics) is used. The time step size is kept as 10^{-3} second, and all results are simulated for physical time of 1 sec, while time averaging is performed after 0.5 sec when flow gets fully developed as shown for lift coefficient in Fig. 3.6, when convergence for continuity, velocity, and turbulent kinetic energy has reached smaller than 10^{-4}.

Table 3.1. Reference values

c = 0.1 m	p_v= 3169 Pa
ρ_l = 997 kg/m^3	μ_l= 0.894× 10^{-3} Pa. s
ρ_v= 0.023 kg/m^3	μ_v= 9.84× 10^{-6} Pa.s

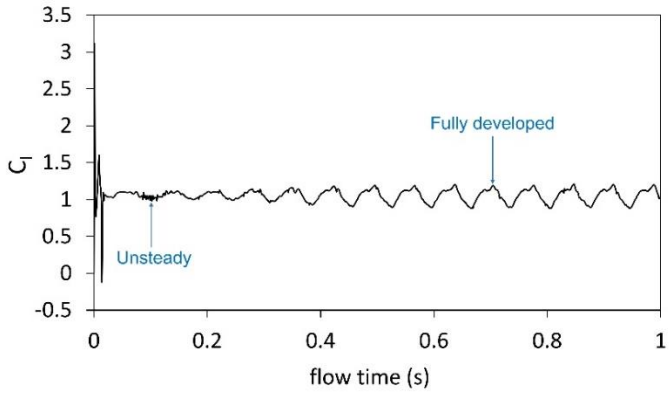

Fig. 3.6. Time evolution of lift coefficient of NACA4412 at α = 8º, σ = 1.5.

3.6.2 Grid Independency Test

The grid independence test, which is conducted to establish the appropriate number of cells, so that the results are independent of the grid size, is a crucial step in every numerical simulation. In this study on cavitating NACA4412 hydrofoil at $\sigma = 1$, four different grids are used varying from coarse (Grid 1) to very fine grids (Grid 4). Grid 1 has 0.8 million cells, Grid 2 has 1 million cells, Grid 3 has 1.4 million cells, and Grid 4 has 1.8 million cells. The drag coefficient (C_d) is used for the grid independency test using Realizable $k - \epsilon$ turbulence model. The angle of attack for NACA4412 is 8º. Table 3.2, and Fig. 3.7 presents the drag coefficient data for NACA4412 hydrofoil at different grids. From the table and figure, it can be observed that the minimum percentage error with respect to Grid 4 is obtained for Grid 3 and value for the same is 0.83 %. Therefore, Grid 3 with 1.4 million cell is grid independent, and it is used for further

simulations. Similarly, the grid convergence index (GCI) is calculated using drag coefficients of Grid 2, Grid 3, and Grid 4 as shown in Table 3.3. There is reduction in GCI with successive grid refinement (GCI43<GCI32), which indicates that the dependency of numerical results on the grid size has been reduced and solution has reached to grid-independent solution (Celik et al. 2008).

Table 3.2. Time averaged drag coefficient (C_d) at different grids for NACA4412 hydrofoil.

S. No	No. of grids (Million)	Time averaged drag coefficient (C_d)	Percentage error relative to Grid 4
Grid 1	0.8	0.111	8.26
Grid 2	1.0	0.126	4.13
Grid 3	1.4	0.122	0.83
Grid 4	1.8	0.121	-----

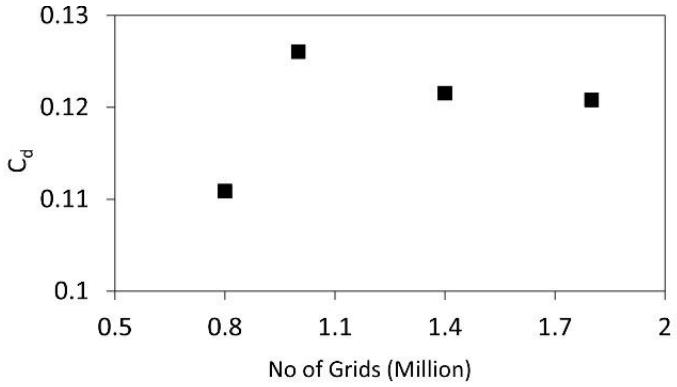

Fig. 3.7. Drag coefficient for grid independence test on NACA4412 hydrofoils.

Table 3.3. Grid Convergence index (GCI) for different grids.

Grids	Grid 2 (Millions)	Grid 3 (Millions)	Grid 4 (Millions)	**GCI^{32}**	**GCI^{43}**
No. of Grids	1.0	1.4	1.8		
C_d	0.1261	0.122	0.121	**0.016891**	**0.00670**

3.6.3 Comparison of Schnerr-Sauer and Zwart-Gerber Cavitation Model on 3D NACA4412 Hydrofoil

In Fig. 3.8, a comparison of time-averaged lift coefficient of 3D NACA4412 hydrofoil using Schnerr-Sauer (SS) and Zwart-Gerber-Belamri (ZGB) cavitation models and Realizable $k-\epsilon$

turbulence model is presented at $\alpha = 8^0$ with the experimental work done by Kermeen (1956) for different cavitation numbers ranging from 0.3 to 1 at Re = 0.8 x 10^6. It is observed that with an increase in the cavitation number, the lift coefficient increases due to smaller cavity on the suction side of hydrofoil. Similarly, in Fig.3.9, the time averaged drag coefficient is presented for different cavitation numbers. It is observed that drag coefficient also increases with σ, as observed for the experimental results also. In Fig. 3.10, the comparison of lift to drag ratio (l/d) is presented at $\alpha = 8^0$ for different cavitation numbers. It can be observed that both the models are predicting very close results with each other for both C_l, C_d, and l/d. Although both the models are giving closer results to the experimental values, ZGB model is known for its accuracy and robustness. One of the key difference between the two models is that the ZGB model uses different approach to model the bubble dynamics. Specifically, the ZGB model includes the correction term in the mass transfer equation that accounts for the effect of bubble deformation on the bubble growth rate. This correction term allows the model to capture the bubble dynamics more accurately in regions where the flow is highly turbulent and bubble shapes are complex. Moreover, F_{vap} and F_{cond} in the source term of ZGB model were rigorously tuned to obtain desired results. Overall, the ZGB cavitation is considered to be more accurate and robust than the Schnerr Sauer cavitation model particularly in situations where the flow is highly turbulent, and the cavitation is more intense. Therefore, we have selected Zwart-Gerber-Belamri model for our simulations which is also consistent with the reported work in the literature (Hidalgo et al. 2014; Liu et al. 2016; Capurso et al. 2017).

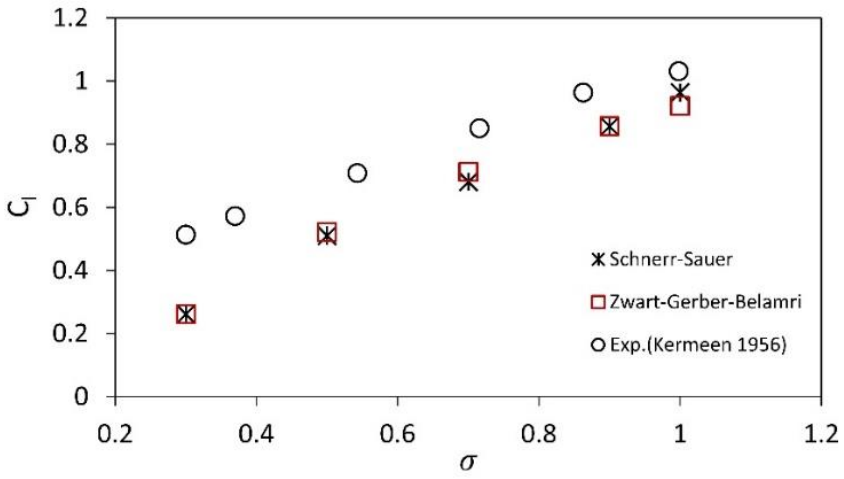

Fig. 3.8. Lift coefficient of NACA4412 using different cavitation models for $\alpha = 8^0$, at different σ.

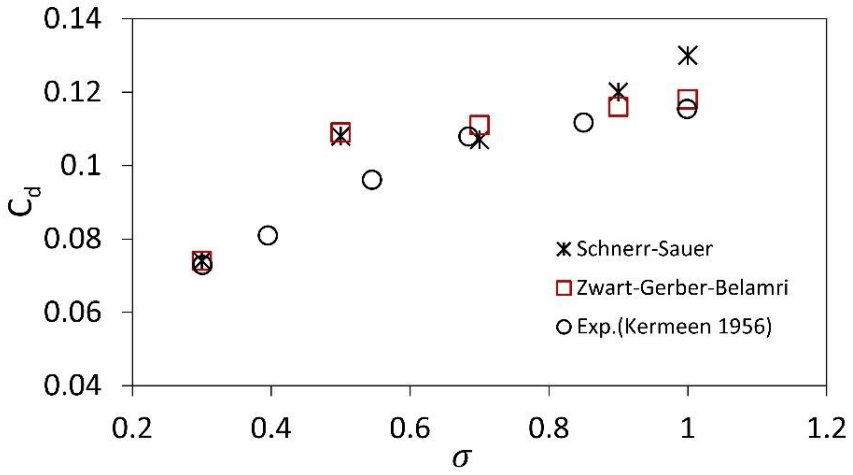

Fig. 3.9. Drag coefficient of NACA4412 using different cavitation models for $\alpha = 8^0$, at different σ.

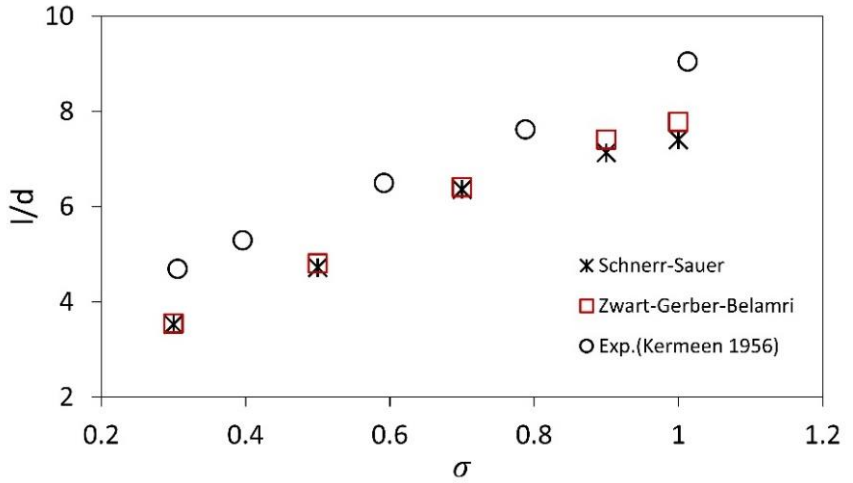

Fig. 3.10. lift to drag ratio of NACA4412 using different cavitation models for $\alpha = 8^0$, at different σ.

3.6.4 Comparison of Different Turbulence Models on NACA4412 and Clark-Y Hydrofoil

In Fig. 3.11, a comparison of time-averaged lift coefficient on 3D NACA4412 hydrofoil using four different turbulence models is presented at $\alpha = 8^0$ with the experimental data of Kermeen (1956) for different cavitation numbers ranging from 0.3 to 1.5 at Re = 0.8 x 10^6. It is observed that with an increase in the cavitation number, the lift coefficient increases, and it became constant as it moves towards non-cavitating condition with almost constant value of C_l. It can be observed that among all the turbulence models Realizable k-ϵ turbulence model and SST $k-\omega$ turbulence model are giving more closer values to the experimental data as compared to other turbulence models.

Similarly, in Fig. 3.12, the comparison of time averaged drag coefficient of 3D NACA4412 hydrofoil with experimental data is presented at $\alpha = 8^0$ for different cavitation numbers using different turbulence models. It is observed that drag coefficient increases with the increasing

cavitation number and attains its peak value and it again decreases on increasing the cavitation number. The maximum value of C_d is attained at $\sigma = 1$. Among all the turbulence models, Realizable $k - \epsilon$ model is giving closer values to the experimental data for almost all cavitation numbers. The other important parameter for studying the hydrodynamic performance is lift-to-drag ratio (l/d) which is shown in Fig. 3.13. The l/d increases with increasing cavitation number, its maximum value is obtained for $\sigma = 1.5$. From this comparison also, it is observed that Realizable $k - \epsilon$ turbulence model is giving closer values to the experimental data. Overall, for NACA4412 the Realizable $k - \epsilon$ model is giving accurate values than other models.

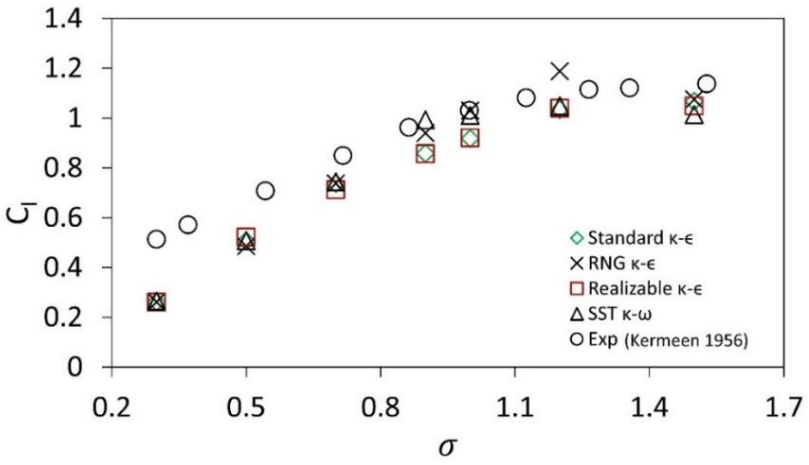

Fig. 3.11. Lift coefficient of NACA4412 at different σ for $\alpha = 8^0$.

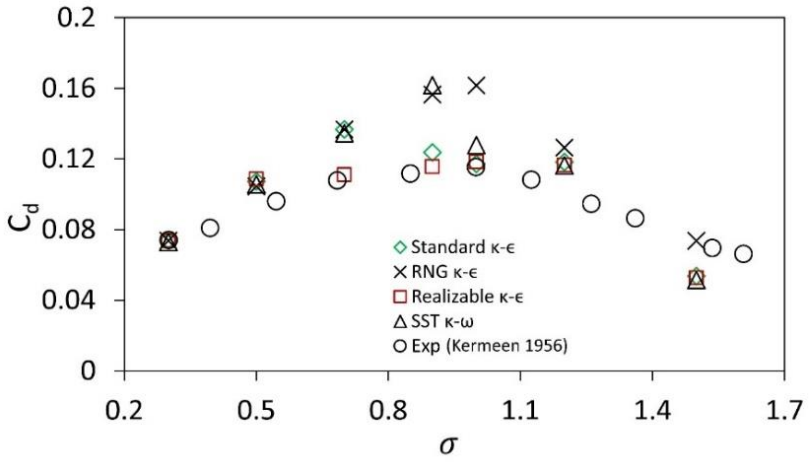

Fig. 3.12. Drag coefficient of NACA4412 at different σ for $\alpha = 8^0$.

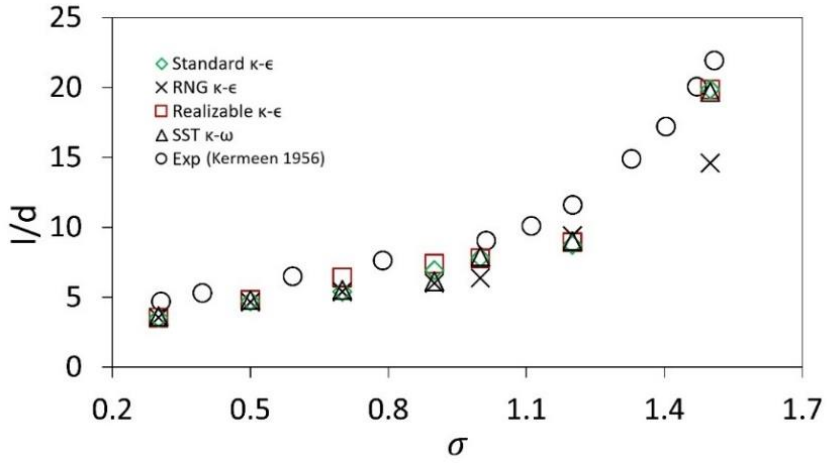

Fig. 3.13. Lift to Drag (l/d) of NACA4412 at different σ for $\alpha = 8^0$.

To get more insight into the performance of different turbulence models, the comparison of numerical results of cavitating Clark-y hydrofoil is presented with the experimental data in the literature (Wang et al. 2001) at an angle of attack 8^o, σ = 0.8 and Re = 0.7 X 10^6. In Table 3.4, the comparison of lift coefficient, drag coefficient, and Strouhal number with experimental values are given. Among all the turbulence models, Realizable $k-\epsilon$ model is giving closer values to experimental values (Wang et al. 2001).

Fig. 3.14 (a) and (b) shows the normalized streamwise velocity profiles at chordwise location of x/c = 0.2 and x/c =0.4 on cavitating Clark-y hydrofoil. At these locations, the Standard $k-\epsilon$, RNG k-ϵ, and SST $k-\omega$ models under-predict the velocities indicating the diffusiveness of the models, whereas Realizable $k-\epsilon$ predicts the velocity gradients accurately showing good correlation with the experimental data. From these comparisons also, it is observed that Realizable $k-\epsilon$ turbulence model is giving closer values to the experimental data. Realizable $k-\epsilon$ model incorporates a modified turbulence dissipation rate equation that more accurately captures the behaviour of turbulence near walls and in regions of high shear, such as those that occur near the surface of the hydrofoil experiencing cavitating. This modification account for the effects of turbulence anisotropy, which is important in these types of flow regimes. In addition, the Realizable $k-\epsilon$ model includes a more detailed representation of the turbulence length scale, which is important parameter in predicting the onset and development of cavitation. This parameter is particularly important in regions where the flow is accelerating or decelerating rapidly, such as vicinity of the hydrofoil. Furthermore, this model is based on more rigorous mathematical formulation than other two-equation models as C_μ is calculated dynamically based on the variation of flow field to satisfy the physics of

turbulent flow. Overall, this model is more accurate to determine the turbulent intensity and velocity profiles. Therefore, this model is recommended for the flow separation and swirling flows, and hence we have used Realizable $k-\epsilon$ turbulence model for our numerical study for all further cases on hydrofoils.

Table 3.4. Comparison of lift coefficient, drag coefficient and Strouhal number for different turbulence model on Clark – Y hydrofoil at $\alpha = 8^0$, $\sigma = 0.8$.

	Standard $k-\epsilon$	RNG $k-\epsilon$	Realizable $k-\epsilon$	SST $k-\omega$	**Experimental** (Wang et al. 2001)
C_l	0.710	0.850	0.742	0.704	**0.760**
C_d	0.104	0.152	0.102	0.101	**0.119**
St	0.184	0.210	0.179	0.186	**0.168**

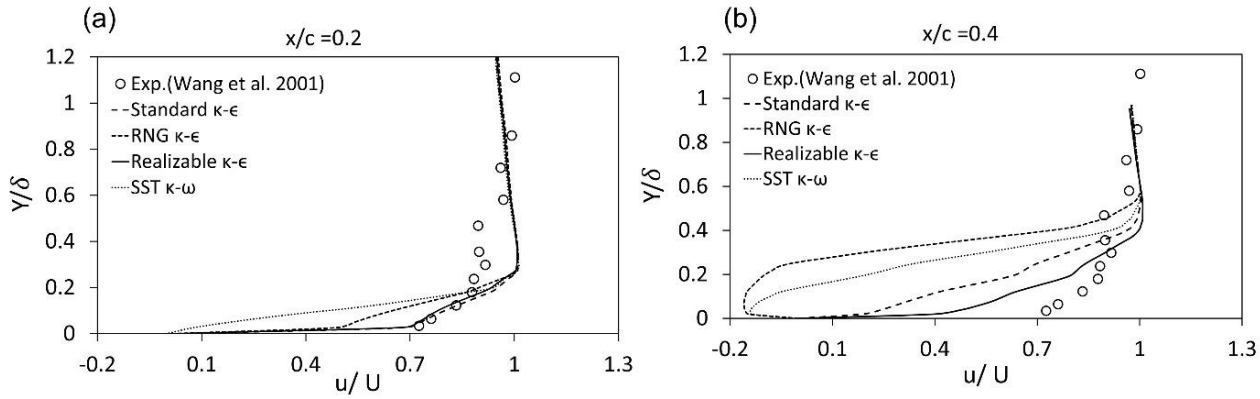

Fig. 3.14. Normalized velocity profile on Clark-Y hydrofoil at (a) x/c = 0.2, and (b) x/c = 0.4.

3.7 Conclusions

In this chapter, the governing equations, turbulence model equations, equations for cavitation models, and fluid structure interaction algorithm is presented. It also presents the systematic investigation of two different cavitation models i.e., Schnerr -Sauer and Zwart-Gerber-Belamri and four of four different turbulence models i.e., Standard $k-\epsilon$, RNG $k-\epsilon$, Realizable $k-\epsilon$, and SST $k-\omega$ on cavitating 3D NACA4412 and Clark-y hydrofoil. The performance is computed in terms of lift coefficient, drag coefficient, lift-to-drag ratio, and velocity profiles.

The major findings, based on the results presented in the chapter, are given below:

(1) Comparing the performance of Schnerr-Sauer and Zwart-Gerber-Belamri cavitation model on cavitating NACA4412 hydrofoil, both models were found to give similar performance.

(2) On comparing performance of different turbulence models on cavitating NACA4412 and Clark-y hydrofoil, Realizable $k-\epsilon$ was found to be more accurate than others.

On the basis of above analysis, in the next chapter of this thesis the hydrodynamic performance of cavitating MHKF-180s hydrofoil is studied at different Reynolds number using Realizable $k-\epsilon$ turbulence model and Zwart-Gerber-Belamri cavitation model. Also, the performance of cavitating MHKF-180s hydrofoil is compared with non-cavitating case at different angles of attack.

CHAPTER 4

PERFORMANCE OF CAVITATING MHKF-180s HYDROFOIL AT DIFFERENT REYNOLDS NUMBER AND COMPARISON WITH NON-CAVITATING CONDITION

In this chapter, the hydrodynamic performance of cavitating MHKF-180s hydrofoil is studied at different Reynolds numbers ranging from 1.1×10^6–2.6×10^6 at different angles of attack. Additionally, the numerical simulation of unsteady cavitating and non-cavitating flows on 3D MHKF-180s hydrofoils is studied using the Realizable k-ϵ turbulence model and Zwart-Gerber-Belamri cavitation model at Re = 1.3×10^6. In the last part of this chapter the hydrodynamic performance of MHKF-180s is compared with the blunt trailing edge MHKF-180 hydrofoil. The performance is computed in terms of lift coefficient, drag coefficient, lift-to-drag ratio, pressure coefficient, cavity shedding, and frequency of the oscillating cavity.

4.1 Geometry, Boundary Conditions and Grid Independency Test

In Fig. 4.1, the 2D profiles of NACA4418, MHKF-180s, and MHKF-180 hydrofoils at an angle of attack 0^0 having chord length of 100 mm is shown. MHKF-180s and MHKF-180 hydrofoils are modified NACA4418 hydrofoil with curved and blunt trailing edge, respectively. NACA4418 foil has maximum camber of 4% located at 40% of chord length with 18% maximum chord thickness and sharp trailing edge. MHKF-180 has finite blunt trailing edge with thickness of 1.88 mm, whereas MHKF-180s has curved trailing edge. The "s" at the end stands for the anti-singing trailing edge profile (Phillips 2012).

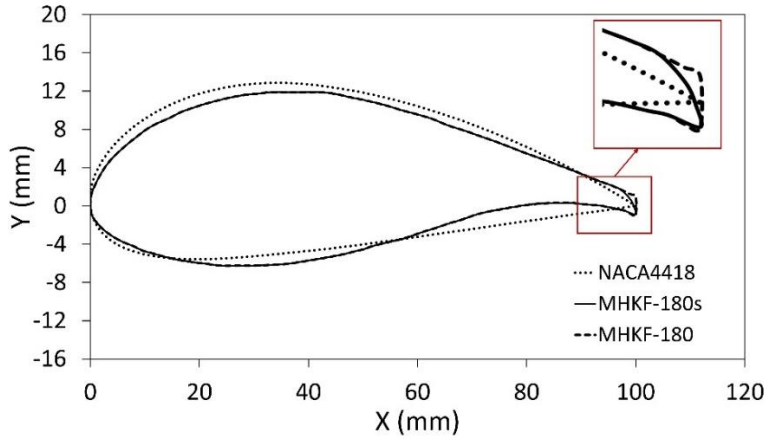

Fig. 4.1. 2D Profiles of NACA4418, MHKF-180s and MHKF-180 hydrofoils.

The computational domain and boundary conditions are kept same as mentioned in section 3.6.1. The velocity at the inlet of domain is given according to the Reynolds number varying from 1.1×10^6-2.6×10^6. In Fig. 4.2, the unstructured tetrahedral elements are shown around MHKF-180s hydrofoil. Fig. 4.3 depicts the y^+ plot, the average value of y^+ obtained is 1.6. The Realizable k-ϵ turbulence model is used along with Zwart-Gerber-Belamri cavitation model. The reference values and all other parameters are provided in section 3.6 of chapter 3.

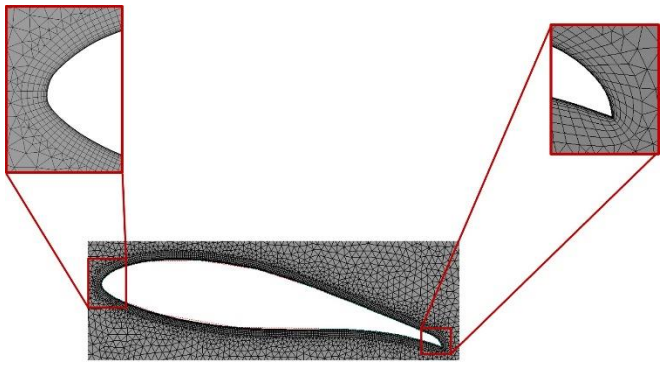

Fig. 4.2. Meshing around hydrofoil.

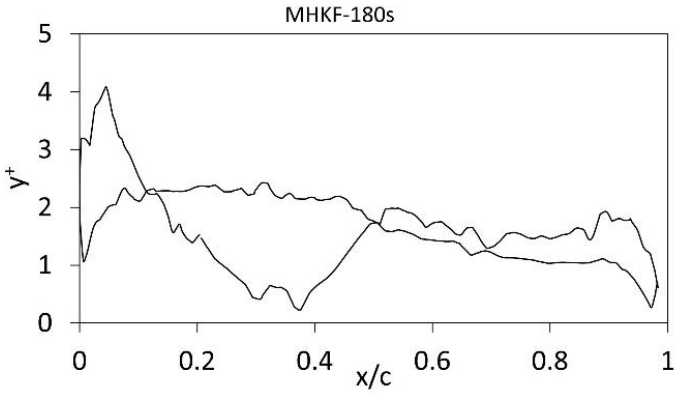

Fig. 4.3. y^+ distribution of first layer on MHKF-180s hydrofoil surface at $\alpha = 10^0$.

For Grid Independency test on cavitating MHKF-180s hydrofoil at $\sigma = 1$, four different grids are used varying from coarse (Grid 1) to very fine grids (Grid 4). Grid 1 has 0.8 million cells, Grid 2 has 1 million cells, Grid 3 has 1.4 million cells, and Grid 4 has 1.8 million cells. The angle of attack for MHKF-180s hydrofoil is kept as 10^o. Table 4.1, and Fig. 4.4 presents the drag coefficient data at different grids. It can be observed that the minimum percentage error with respect to Grid 4 is obtained for Grid 3 and value for the same is 0.12 %. Therefore, Grid 3 with 1.4 million cell is grid independent. The grid convergence index (GCI) of drag coefficients of Grid 2, Grid 3, and Grid 4 as shown in Table 4.2. There is reduction in GCI with

successive grid refinement (GCI43<GCI32), it shows that solution has reached to grid-independent solution.

Table 4.1. Time averaged drag coefficient (C_d) at different grids for MHKF-180s.

S. No	No. of grids (Million)	Time averaged drag coefficient (C_d)	Percentage error relative to Grid 4
Grid 1	0.8	0.1788	3.47
Grid 2	1.0	0.1747	1.11
Grid 3	1.4	0.1726	0.12
Grid 4	1.8	0.1728	-----

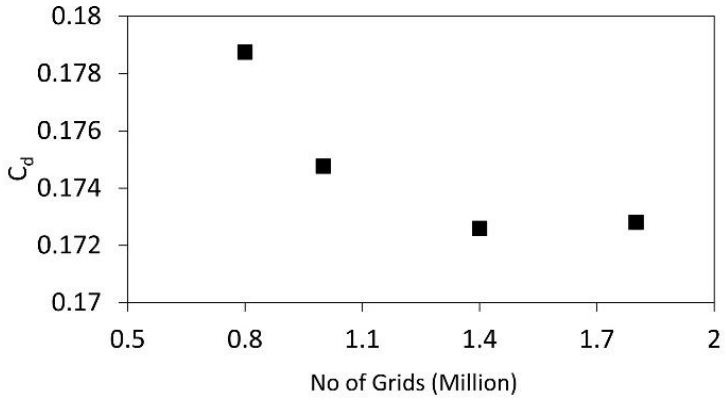

Fig. 4.4. Drag coefficient for grid independence test on MHKF-180s hydrofoils.

Table 4.2. Grid Convergence index (GCI) for different grids.

Grids	Grid 2 (Millions)	Grid 3 (Millions)	Grid 4 (Millions)	**GCI^{32}**	**GCI^{43}**
No. of Grids	1.0	1.4	1.8		
C_d	0.1747	0.1726	0.1728	**0.001487**	**0.000284**

4.2 Performance of Cavitating MHKF-180s Hydrofoil at Different Reynolds Number

The performance of cavitating 3D MHKF-180s hydrofoil at σ =1 is studied at different angles of attack for Reynolds number ranging from 1.1×10^6 to 2.6×10^6. In Fig. 4.5, the time averaged lift coefficient at different angles of attack (α = -5°, 0°, 5°, 7°, 10°, and 12°) is presented. It is observed that C_l increases almost linearly with α till 5°, until effect of flow separation begins,

and curve becomes non-linear. The maximum value of lift is obtained at α = 12°. MHKF-180s being unsymmetrical hydrofoil has non-zero value of lift coefficient at α = 0°. However, C_l moves to zero at negative value of α, as it can be seen for α = -5°. The lift coefficient slope is not influenced by Reynolds number and the same behaviour is observed by the researchers in the past (Goundar and Ahmed 2014).

Similarly, in Fig. 4.6, the time averaged drag coefficient is shown as a function of angle of attack at σ =1. The drag coefficient is the sum of pressure drag, skin friction drag, and induced drag. The pressure drag is due to shape and size of hydrofoil, skin friction drag is due to viscous effect, and induced drag is the drag generated due to lift. Because of increasing pressure drag brought on by flow separation and more cavity at higher angles of attack as well as lift-induced drag, the overall drag coefficient likewise rises with the angle of attack. Overall, the drag coefficient is found to be independent of Reynolds number. The minimum value of C_d is obtained at 0° and maximum value at 12° for the given range of Reynolds number.

The ratio of lift-to-drag (l/d), is an important parameter to measure the hydrodynamic efficiency; higher l/d means better hydrofoil performance. Fig. 4.7, present the l/d of cavitating MHKF-180s along angles of attack at σ =1. The maximum l/d is obtained at α = 0°, due to large value of C_l and minimum C_d at this angle. For σ =1, MHKF-180s is giving higher performance at 0° as observed in terms of l/d. The Reynolds number effect on l/d can also be observed at 0°, with minimum l/d of 38 at Re =1.1 million, maximum l/d of 44 at Re = 2.6 million. At all other angles of attack, there is negligible effect of Reynolds number on lift to drag ratio.

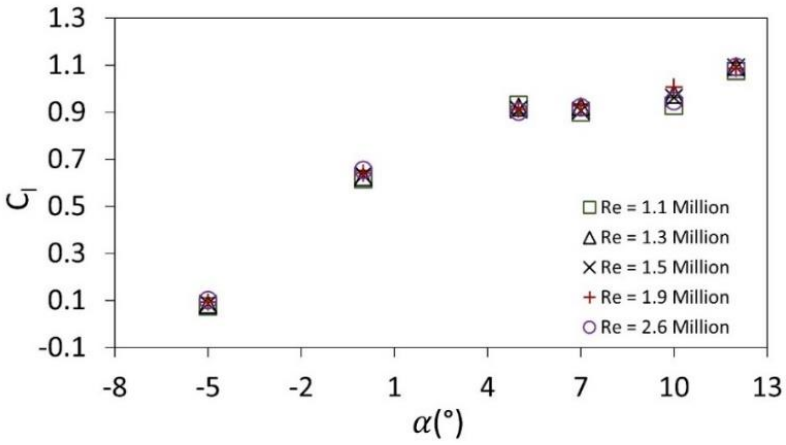

Fig. 4.5. Lift coefficient of cavitating MHKF-180s hydrofoil at different Reynolds numbers.

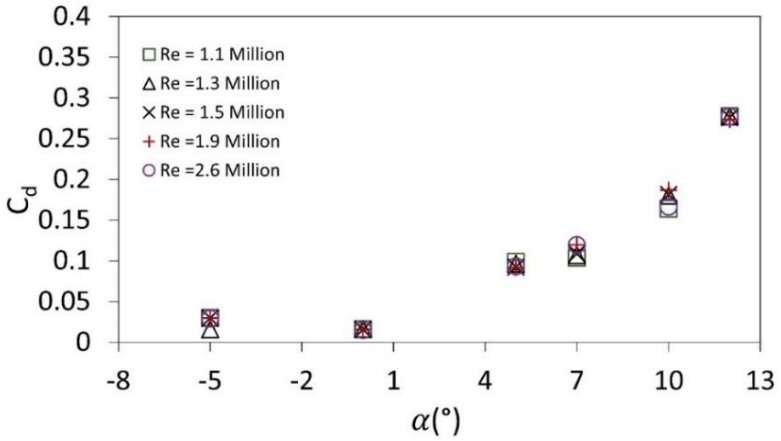

Fig. 4.6. Drag coefficient of cavitating MHKF-180s hydrofoil at different Reynolds numbers.

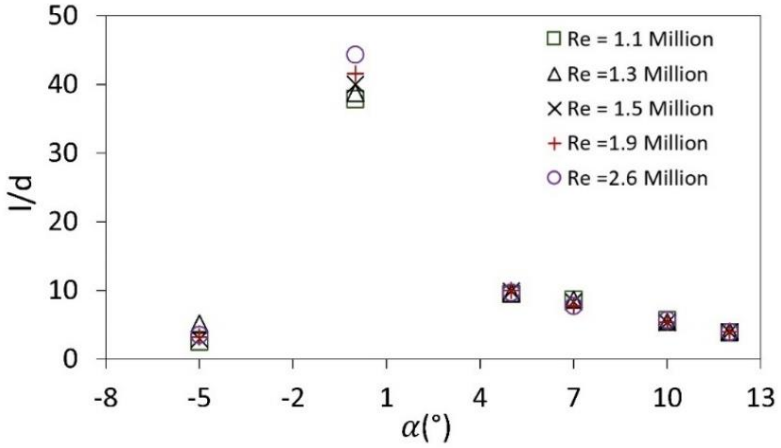

Fig. 4.7. Lift to Drag ratio of cavitating MHKF-180s hydrofoil at different Reynolds numbers.

The distribution of vapor cavity on MHKF-180s hydrofoil at an angle of attack (α = 5°, 7°, 10°, and 12°) is shown in Fig. 4.8 for Re = 1.3, 1.5, and 1.9 million. For σ =1, the cavitation starts at $\alpha = 5^0$, and it increases with angle of attack due to pressure drop on the suction side of the hydrofoil. For all Reynolds numbers, the maximum length of cavity is observed at 12°, which sheds along the trailing edge of the hydrofoil. Similarly, the streamlines over MHKF-180s hydrofoil at different angles of attack are shown in Fig. 4.9. For low angles of attack, the streamlines are relatively undisturbed, and as α is increased from 5°, the streamlines exhibit a considerable upward deflection in the region of leading edge, and then subsequent downward deflection in the region of trailing edge as observed for 7°, 10°, and 12°. The stagnation point gradually shifts from leading edge to the bottom surface of the hydrofoil as angle of attack increases. Overall, the flow separation location and stagnation point do not change with Reynolds number resulting in negligible effect on the C_l and C_d.

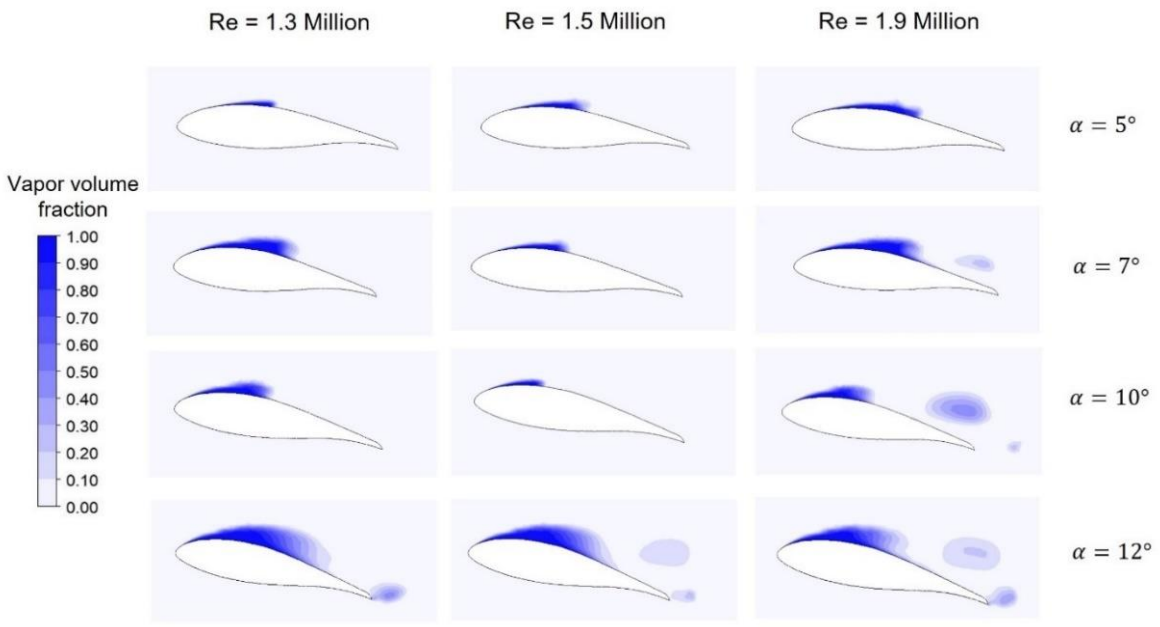

Fig. 4.8. Vapor fraction on MHKF-180s hydrofoil for σ = 1 at different Reynolds numbers.

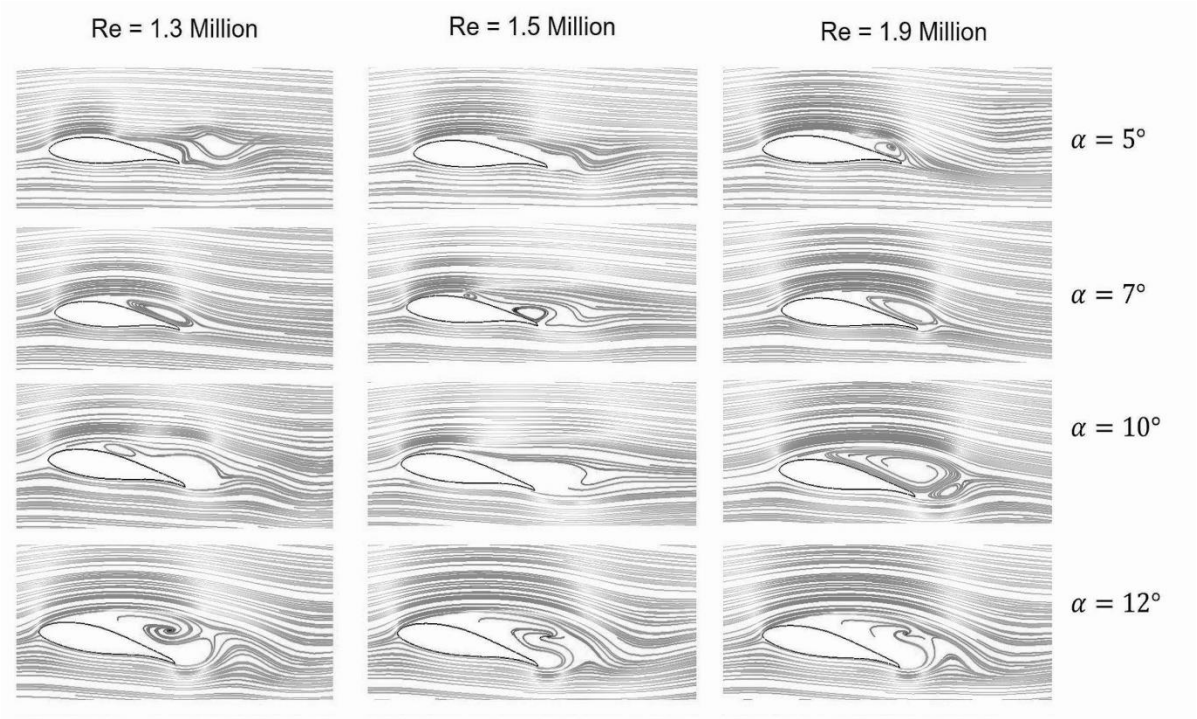

Fig. 4.9. Velocity streamlines on MHKF-180s hydrofoil for σ =1 at different Re.

4.3 Comparison of Performance of Cavitating and Non-Cavitating MHKF-180s hydrofoil at Re = 1.3 Million

In this section, the performance of cavitating and non-cavitating MHKF-180s hydrofoil is studied at different angles of attack (-5^o, 0^o, 5^o, 7^o, 10^o, and 12^o) at Reynolds number 1.3 X 10^6

using Realizable k-ϵ turbulence model. Fig. 4.10 (a) compares the time averaged lift coefficient, and it is observed that at α = -5^o, and 0^o there is no cavitation on the hydrofoil. Therefore, both cases have the same value of C_l. The cavitation starts at α = 5^o and remains for further larger angles. There is drop in the C_l value for the cavitating case with the maximum drop of 40.5% at 10^o. Similarly, Fig 4.10 (b) gives the comparison for drag coefficient, and it is observed that C_d for cavitating case is higher than the non-cavitating case for all angles of attack. The increase in C_d is attributed to the increase in pressure drag due to flow separation as a result of cavity on the hydrofoil. The maximum cavity is observed at 12^o as shown in Fig.4.8, which results in almost seven times higher C_d than the non-cavitating case. Other researchers in the past observed the same behaviour (Kashyap and Jaiman 2021).

Fig. 4.10 (c) shows the lift-to-drag ratio for the cavitating and non-cavitating conditions. The l/d for cavitating conditions reduces mainly due to much higher drag and lower lift. The maximum reduction is observed at 12^o, which has the largest cavity. Overall, the hydrodynamic performance of MHKF-180s hydrofoil was reduced for the cavitating condition.

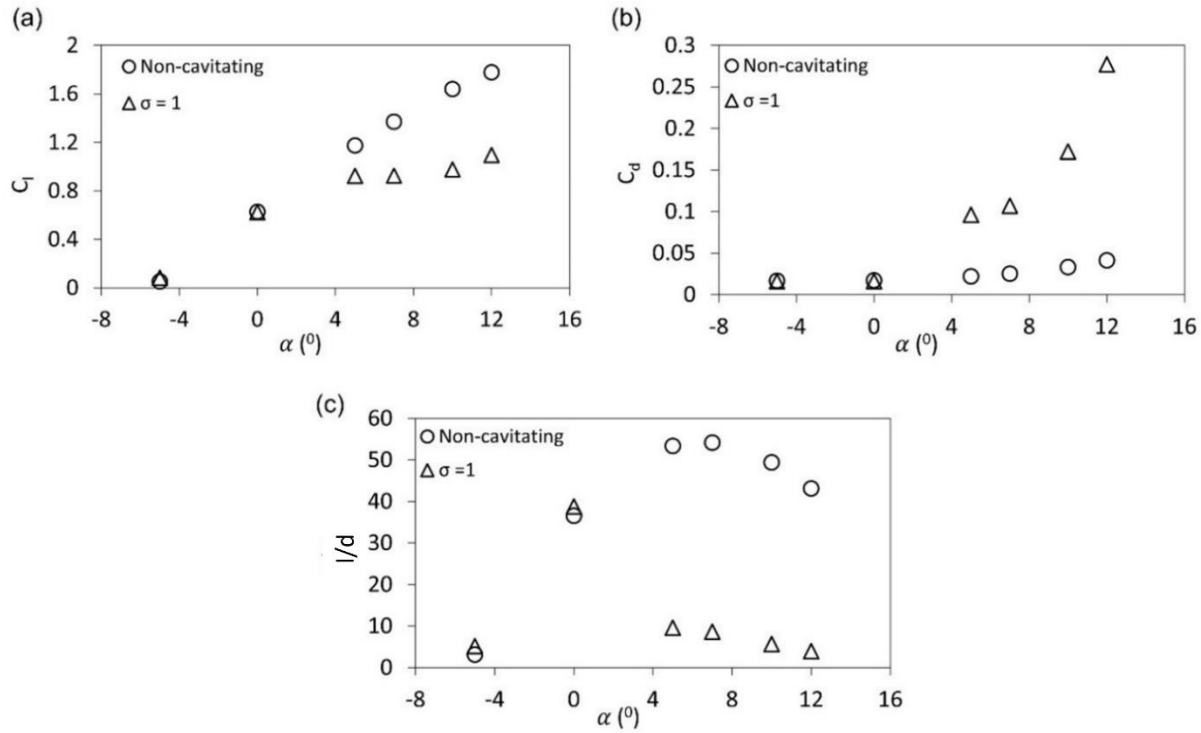

Fig. 4.10. Comparison of (a) lift coefficient, (b) drag coefficient, and (c) lift to drag ratio for the cavitating (σ =1) and non-cavitating conditions of MHKF-180s hydrofoil at different angles of attack.

Next, the pressure coefficient (-C_p) curve for the non-cavitating and cavitating conditions are compared for MHKF-180s hydrofoil at Reynolds number 1.3×10^6 for different angles of attack as shown in Fig. 4.11. At the leading edge there is stagnation, which has a

maximum value of $-C_p$ as -1, for both cavitating and non-cavitating conditions, which shift to the lower side of the hydrofoil at larger angles. The hydrofoil pressure gradually increases towards the trailing edge, where an adverse pressure gradient is observed. As the angle of attack increases, the flow starts separating from the hydrofoil upper surface, leading to a sudden pressure drop near the leading edge like $-C_p \approx 5$ at $\alpha = 12^o$ for non-cavitating case, and then rapidly increasing downstream of the leading edge. For the cavitating condition, the presence of cavity is represented by the constant C_p curve along the chord length (Štigler 2009; Wu and Chen 2016). The largest cavity is observed at $\alpha = 12^o$, covering almost 80% of the upper surface of the hydrofoil. The more significant difference between the cavitating and non-cavitating curve is observed on the upper surface of the MHKF-180s hydrofoil, where cavity forms and flow separation occurs. Flow separation does not affect the bottom surface of the hydrofoil; therefore, C_p curves have a minimal difference on the bottom side for cavitating and non-cavitating conditions.

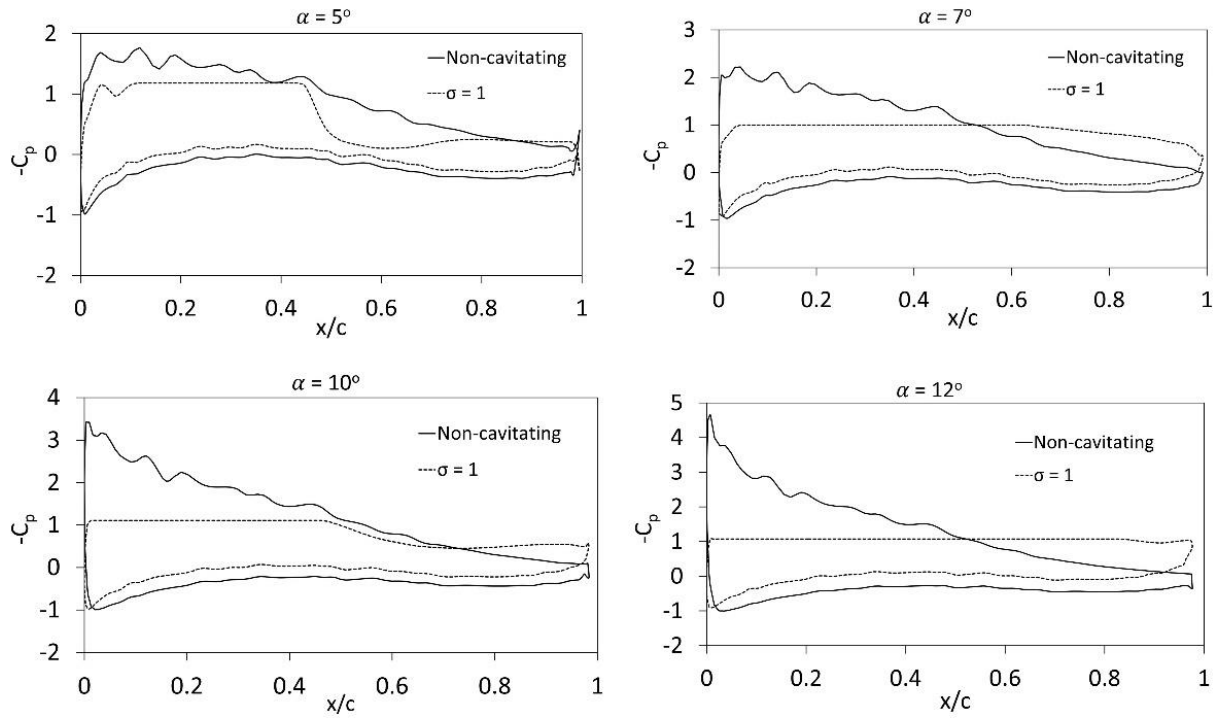

Fig. 4.11. Comparison of pressure coefficient curves for the cavitating (σ =1) and non-cavitating conditions of MHKF-180s hydrofoil at different angles of attack.

In Fig. 4.12, the comparison of lift and drag coefficient periodic fluctuations of MHKF-180s hydrofoil is presented at different angles of attack for cavitating and non-cavitating condition along the normalized flow time. For the cavitating case, there is upper and lower peaks about which the lift coefficient and drag coefficient values fluctuate whereas, for the non-cavitating condition it is more like single value that is attained along the time. This may

be attributed to the flow separation due to cavities on the hydrofoil and the vortex shedding. As the cavity on the hydrofoil increase with the increase in angle of attack, the difference between the C_l and C_d of the cavitating and non-cavitating condition increases.

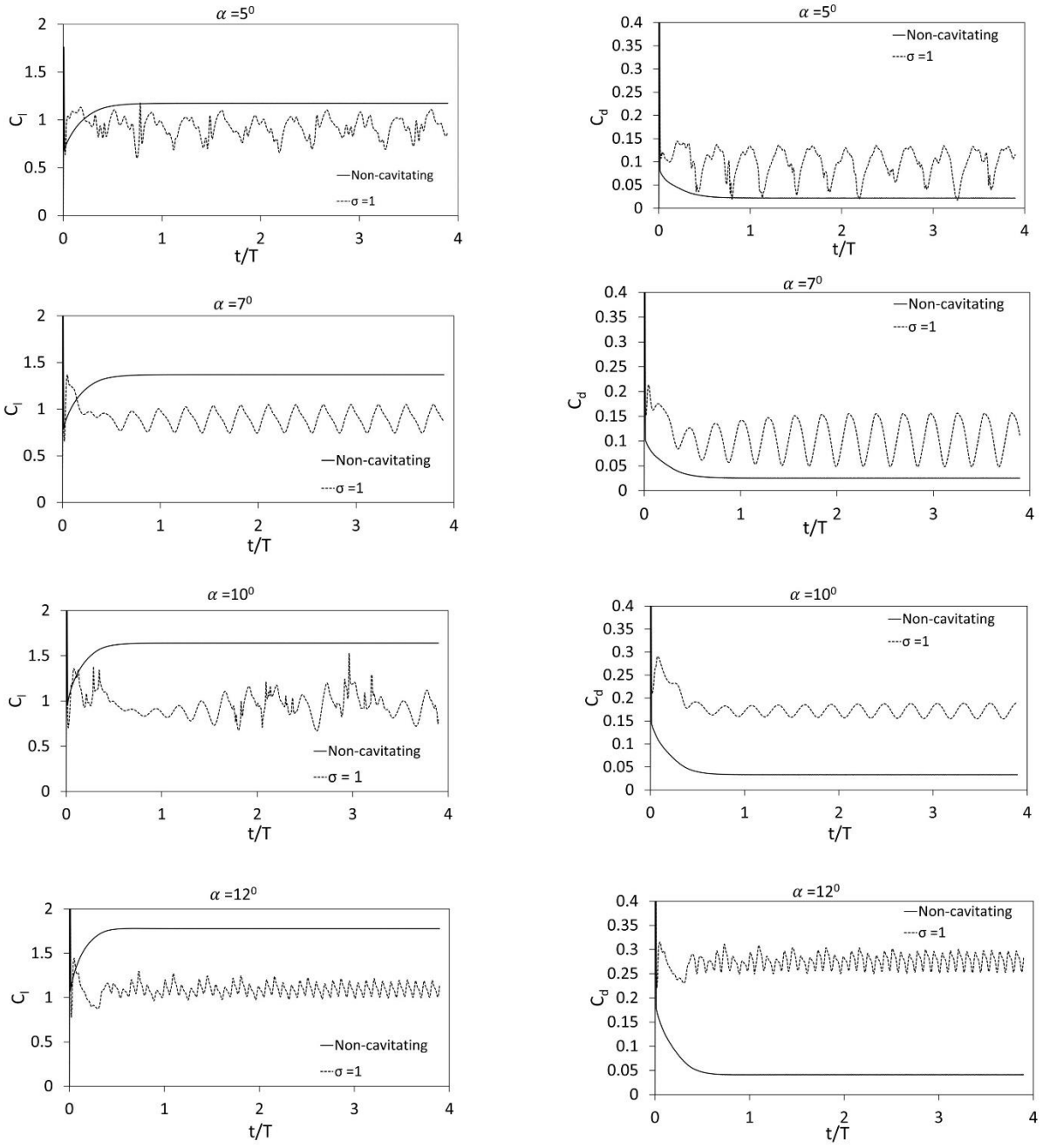

Fig. 4.12. Comparison of lift coefficient and drag coefficient along the time for different α.

The skin friction coefficient is plotted in Fig. 4.13 for cavitating and non-cavitating conditions. The location at which $C_f = 0$, is considered the point of flow separation (Kundu et al. 2019). At lower angles of attack, the flow is attached to the hydrofoil. With the increase in the angle of attack, the flow separation point is shifted from the trailing edge towards the leading edge as shown in Fig. 4.9. There is an increase in the C_f value at the trailing edge of

the hydrofoil. For the non-cavitating case, the skin friction coefficient is higher at both the leading and trailing edges. For the cavitating case, the local wall shear stress is lower on the hydrofoil due to the presence of a cavity. It remains constant for cavity length, similar to pressure coefficient curves in cavitating condition.

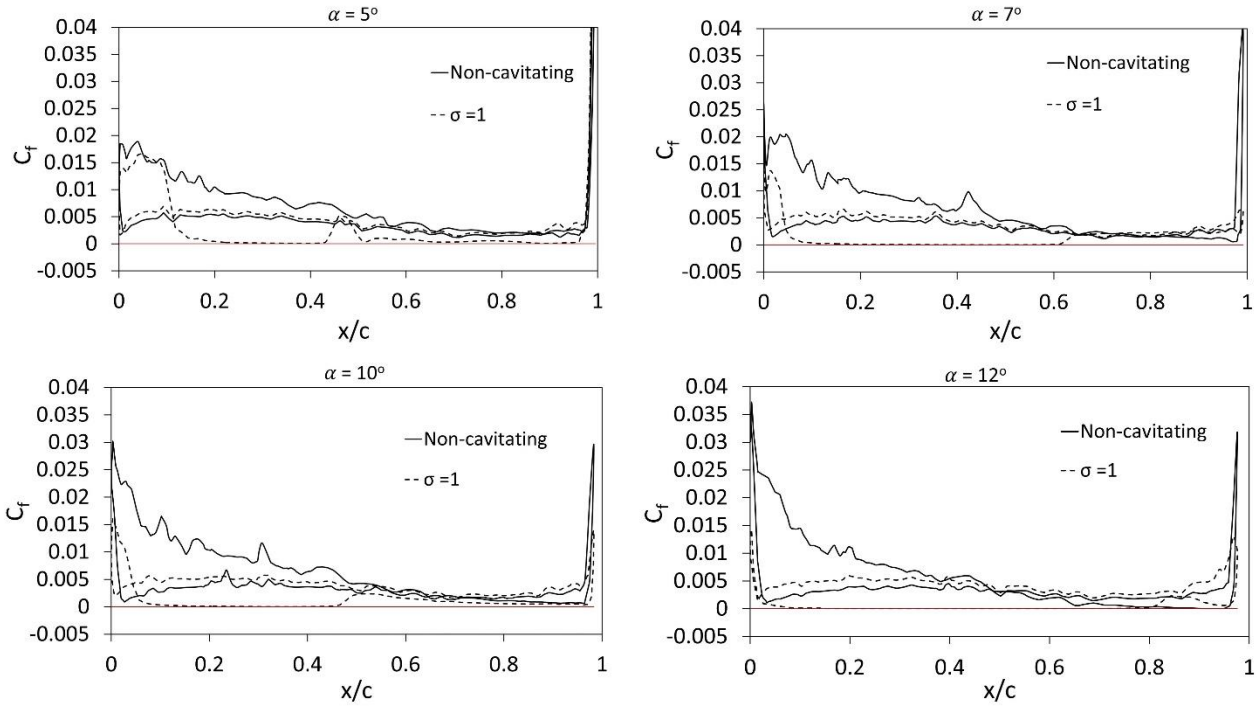

Fig. 4.13. Comparison of skin friction coefficient curves for the cavitating (σ =1) and non-cavitating conditions of MHKF-180s hydrofoil at different angles of attack.

In Fig. 4.14 the turbulent kinetic energy (T.K.E) around the non-cavitating and cavitating MHKF-180s hydrofoil at 12°, and Re = 1.3 X 10^6 is presented. For the non-cavitating case, the maximum turbulent kinetic energy is around 4 m^2/s^2 obtained in the wake region of the hydrofoil. The T.K.E transitions for this condition occurs on the upper surface at 70% of the chord length. For cavitating case, the turbulent kinetic energy is much higher, around 25 m^2/s^2, due to the formation and collapse of the vapor cavity on the hydrofoil. The dynamic viscosity of water vapor (μ_v = 9.87 x10−6kg/(ms)) at 25^0C is approximately 90 times lower than the viscosity of water (μ_l = 8.9 x10−4kg/(ms)). In general, lower viscosity fluids tends to have higher turbulent kinetic energy than higher viscosity fluid. This is because lower viscosity fluids have weaker internal friction and therefore, easier to deform and create turbulence within. In lower viscosity fluids, the energy transfer through the energy cascade can occur more efficiently, leading to higher T.K.E levels. On the other hand, higher viscosity fluids have stronger internal friction, which makes it more difficult for the kinetic energy to be transferred

between different scales of eddies and causes a dampening effect on the turbulence. The cavity closure region is highly unsteady which increases the turbulent kinetic energy at the cavity interface, particularly at the rear portion of the cavity around the trailing edge (Li et al. 2019).

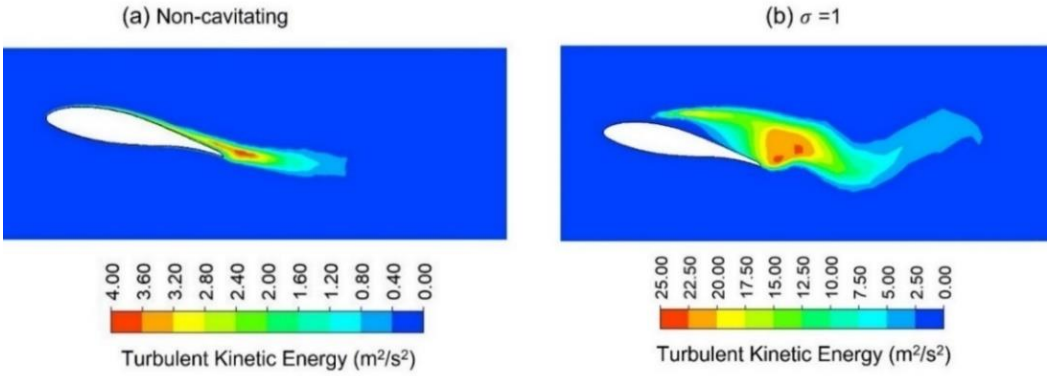

Fig. 4.14. Turbulent kinetic energy on (a) non-cavitating and (b) cavitating MHKF-180s hydrofoil at α =12°.

In Fig. 4.15, the comparison of streamline distribution on cavitating and non-cavitating MHKF-180s hydrofoil is shown at an angle of attack 12°, and at Reynolds number 1.3 X 10^6. For non-cavitating conditions, the streamlines follow the hydrofoil profile with higher velocity values. The flow remains attached for almost 80% of the chord length, whereas, for the cavitating condition, the flow gets separated at almost 25% of chord length due to the presence of the attached cavity. There is a recirculation zone between the attached cavity and a cavitation cloud near the trailing edge of the hydrofoil.

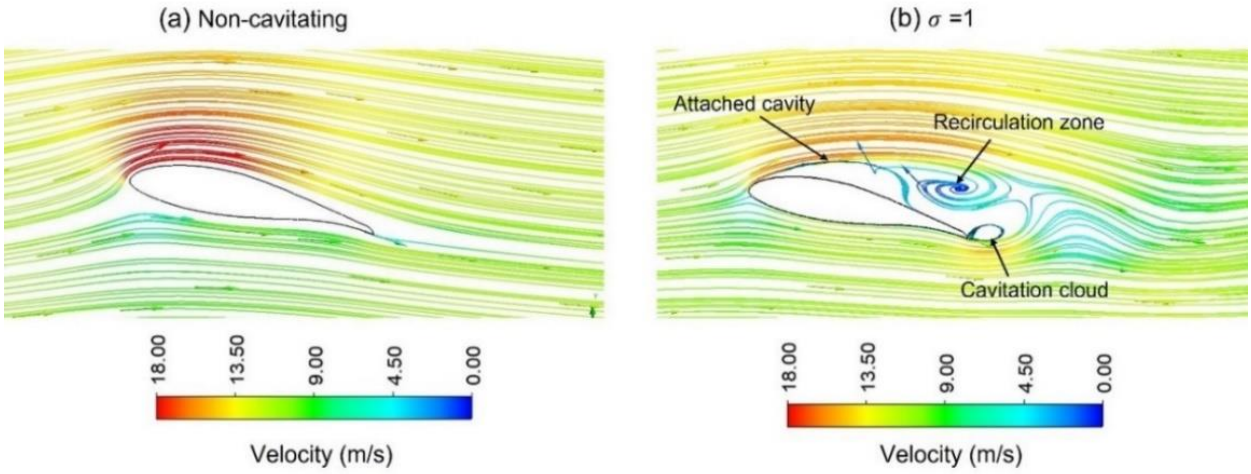

Fig. 4.15. Velocity streamlines (a) non-cavitating and (b) cavitating MHKF-180s hydrofoil, α =12°.

The comparison of normalized x-component velocity (u/U_∞) profiles on cavitating and non-cavitating MHKF-180s hydrofoil along the normalized vertical lines (y/c) on the suction side is presented in Fig. 4.16, at α =12°. The velocity gradient with positive values shows that

flow remains attached to the hydrofoil surface, whereas flow separation is shown with negative values. It is observed that for the non-cavitating condition, the flow remains attached to the hydrofoil surface till x/c = 0.8, and the flow gets separated at the trailing edge only, as shown for x/c = 1. For cavitating conditions due to the presence of a cavity, the flow separation starts at x/c = 0.4, indicated by negative velocity gradients. Overall, for all locations of x/c, the non-cavitating case has a higher velocity than cavitating condition along the vertical line, i.e., y/c = 0.25. The maximum difference between velocity profiles is observed at x/c =0.8 near the trailing edge where the recirculation zone is developed, as shown in Fig. 4.15.

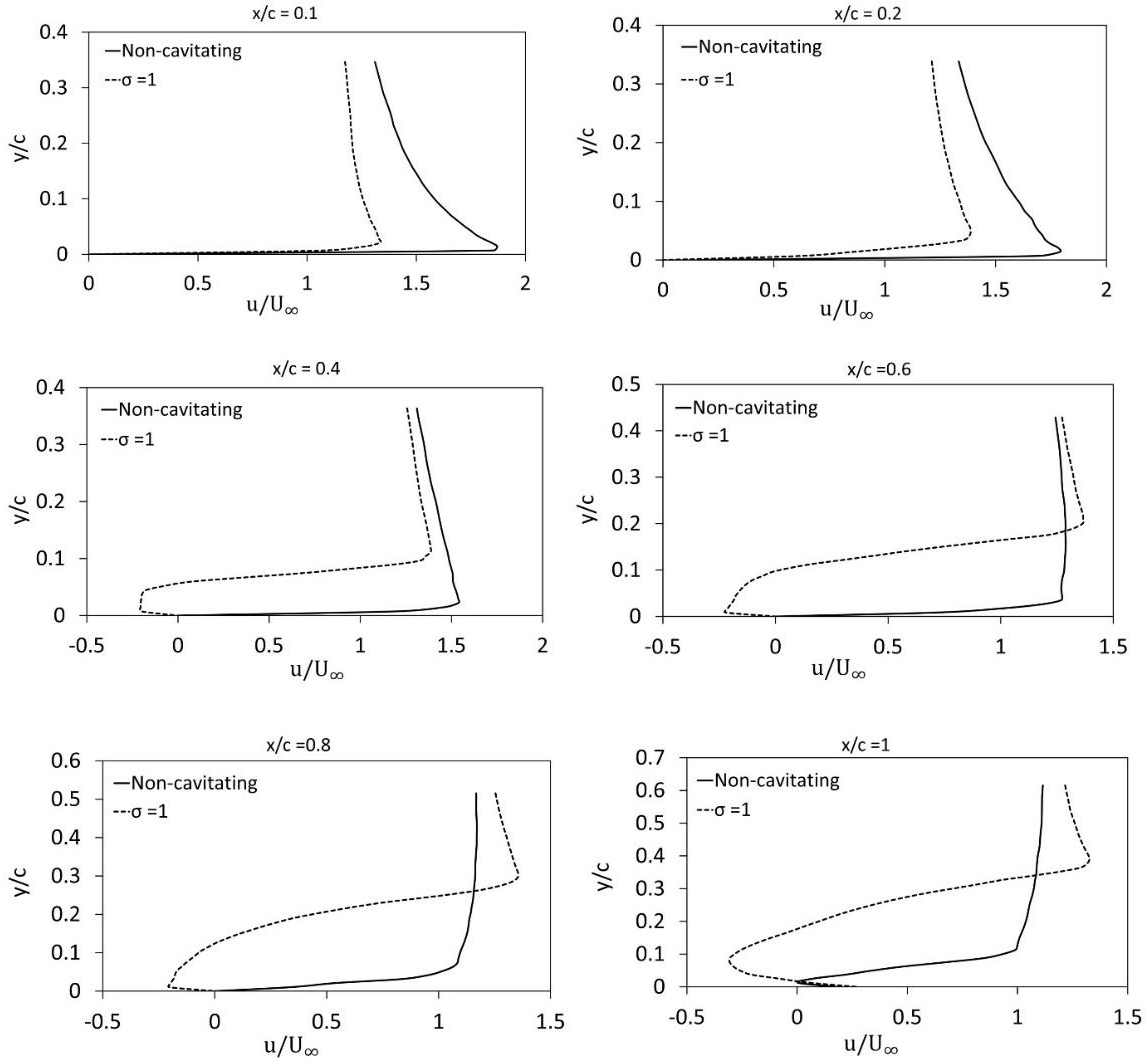

Fig 4.16. Comparison of normalized x-velocity profiles on upper surface of non-cavitating and cavitating MHKF-180s hydrofoil at α =12^o at locations (x/c = 0.1, 0.2, 0.4, 0.6, 0.8, and 1).

Fig. 4.17, shows the one cycle of unsteady cavity development and its breakdown on MHKF-180s hydrofoil at 12^o angle of attack and σ = 1 using iso-surface. The cavity starts near

the leading edge and covers more than half of the suction surface of the hydrofoil in the form of attached sheet cavity (t = 0.5 sec). Sheet cavity mostly starts around the leading edge, extends along the chord. There is formation of cavitation cloud on the trailing edge of the hydrofoil, due to periodic disturbance of sheet cavitation. This cavitation cloud sheds and collapses from the trailing edge in the form of rolling sheet and dispersed bubbles (t = 0.52 sec). These bubbles travel with the flow, expand and shrink as they encounter varying local pressure. On the edge of the attached cavity there are small regions of bubble which move rapidly in the downstream direction away from the hydrofoil.

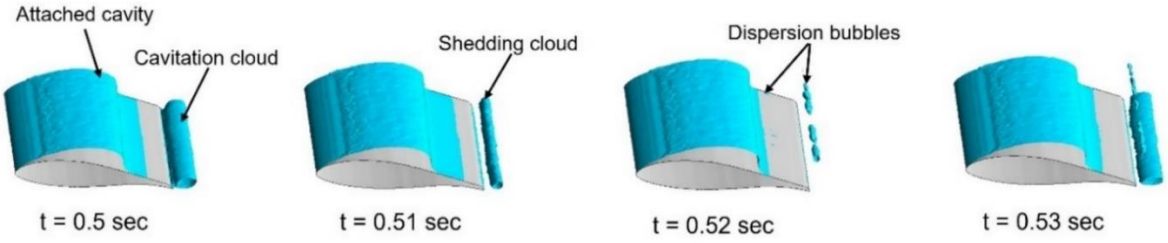

Fig 4.17. Instantaneous cavity shape in a cycle (iso-surface of α_v = 0.2) on cavitating MHKF-180s hydrofoil at α =12°, σ =1.

Lastly, in Fig. 4.18 performance of MHKF-180s hydrofoil is compared with MHKF-180 hydrofoil at different angles of attack for Re =750000, and σ =1, in terms of lift coefficient, drag coefficient, and lift to drag ratio. MHKF-180s and MHKF-180 are the modified NACA4418 hydrofoils as shown in Fig. 4.1. The difference in both the foils is at the trailing edge only where MHKF-180s has curved trailing edge and MHKF-180 has blunt trailing edge. On comparing the C_l, C_d, and l/d ratio, it is observed that there is negligible difference in the performance of both the hydrofoils due to change in the trailing edge profile of the hydrofoils. Therefore, on the basis of this analysis in the next chapter of thesis the hydrodynamic and structural performance of the 3D MHKF-180 hydrofoil with blunt trailing edge is studied at different angles of attack and at different cavitation numbers.

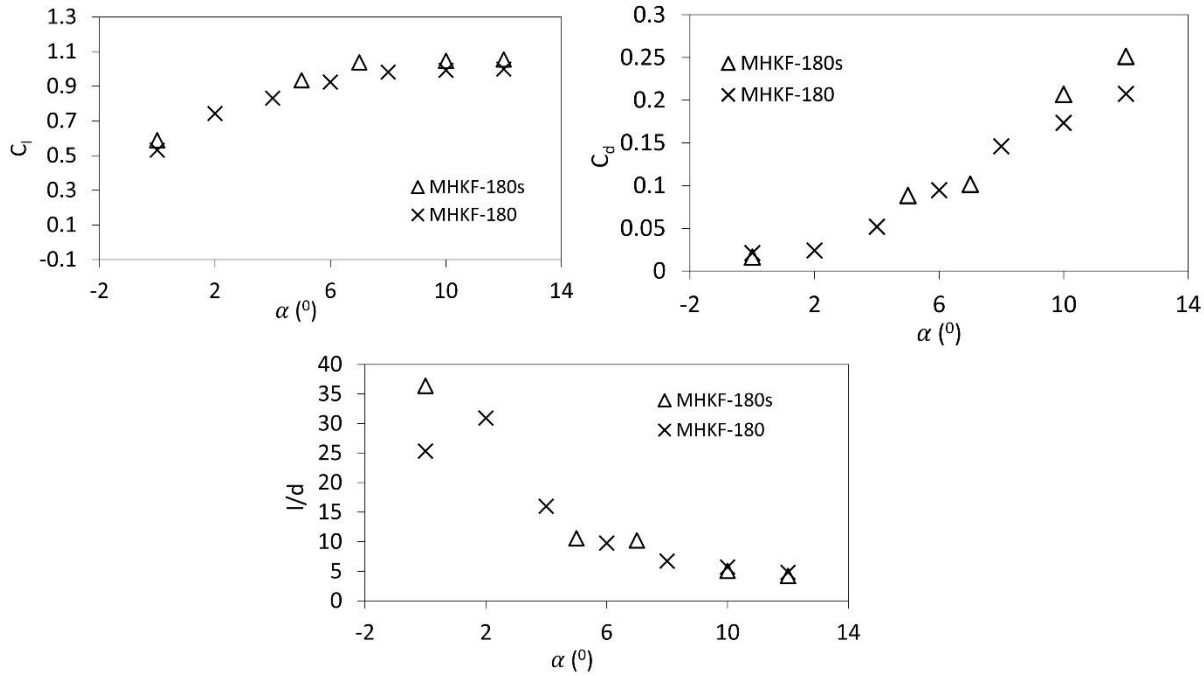

Fig 4.18 Comparison of lift coefficient, drag coefficient, and lift to drag ratio at σ =1 for MHKF-180s and MHKF-180 hydrofoils at different angles of attack.

4.4 Conclusions

In this chapter, to study the effect of Reynolds number on the hydrodynamic performance of cavitating MHKF-180s hydrofoil at different angles of attack, the results are compared for Reynolds number ranging from 1.1 X 10^6 – 2.6 X 10^6. Also, comparative study of hydrodynamic performance of 3D cavitating and non-cavitating MHKF-180s hydrofoil is carried out numerically using ANSYS Fluent at different angles of attack varying from -5^o to +12^o using Realizable $k-\epsilon$ turbulence model at Re = 1.3 X 10^6. The performance is computed in terms of lift coefficient, drag coefficient, lift-to-drag ratio, pressure coefficient, skin friction coefficient, velocity profiles, vapor volume fraction, shedding frequency. Vapor volume fraction is calculated using Zwart-Gerber-Belamri cavitation model. Additionally, the performance comparison of MHKF-180s and MHKF-180 is made at different angles of attack for σ =1. The major findings, based on the results presented in the chapter, are given below:

(1) The hydrodynamic performance of cavitating 3D MHKF-180s hydrofoil at different angles of attack and σ = 1, found to be independent of Reynolds number.

(2) For σ =1, the MHKF-180s has maximum cavity at an angle of attack 12^o at all Reynolds number.

(3) On comparing the hydrodynamic performance of non-cavitating and cavitating (σ =1) MHKF-180s hydrofoil at different angle of attack (α = -5^o, 0^o, 5^o, 7^o, 10^o, and 12^o) at Re = 1.3 X 10^6, it was found that:

(i) There is no cavitation on MHKF-180s hydrofoil at α = -5^o and 0^o for σ =1.

(ii) Lift coefficient for cavitating case is reduced as compared to non-cavitating condition with maximum reduction of 40.5% at α = 10^o.

(iii) The drag coefficient for cavitating cases is higher at almost all angles of attack when compared to non-cavitating conditions due to increase in pressure drag. The maximum increment in C_d value is obtained at α =12^o which is almost 7 times of non-cavitating C_d.

(iv) Lift-to-drag ratio for cavitating condition is found to be lower than non-cavitating condition. The maximum reduction is observed at α =12^o, due to maximum cavity.

(v) For cavitating condition, the skin friction coefficient (C_f) is found to be lower due to presence of cavity on the upper surface of hydrofoil.

(vi) At α = 12^o, the x-component velocity on vertical lines of hydrofoil upper surface was found to be lower at σ =1, with much earlier flow separation along the chord.

(vii) At α = 12^o, the maximum turbulent kinetic energy present at the wake of cavitating hydrofoil was much higher (25 m^2/s^2) than non-cavitating hydrofoil (4 m^2/s^2).

(4) On comparing the hydrodynamic performance of MHKF-180s and MHKF-180 at different angles of attack and σ =1, the negligible change in the performance is found between two foils, and therefore on the basis of this analysis, in the next chapter of the thesis the hydrodynamic and structural performance of 3D MHKF-180 hydrofoil is studied at different angles of attack and at different cavitation numbers.

CHAPTER 5

FLUID-STRUCTURE INTERACTION (FSI) ON CAVITATING 3D MHKF-180 AND NACA4418 HYDROFOILS[1]

In this chapter a numerical investigation of structural and hydrodynamic performance of 3D stainless steel MHKF-180 and NACA4418 cavitating hydrofoils has been carried out using one-way fluid-structure interaction (FSI) for different angles of attack and at different cavitation numbers. The simulation is performed at a chord-based Reynolds number, Re = 750000, in ANSYS software. Under the application of hydrodynamic load, the structural performance of MHKF-180 is compared with NACA4418 in terms of natural frequency, maximum tip deformation, and von Mises stress, whereas hydrodynamic performance is compared in terms of lift coefficient, drag coefficient, lift to drag ratio, pressure coefficient, and Strouhal number. The fluid flow is simulated using the unsteady-Reynolds-averaged-Navier-Stokes (URANS) equations and Realizable $k-\epsilon$ turbulence model. The cavitation effect on the hydrofoil is studied using the Zwart-Gerber-Belamri cavitation model. The present results are validated by comparing the natural frequency and pressure coefficient curve of the non-cavitating NACA66 hydrofoil and lift coefficient and drag coefficient of cavitating NACA4412 hydrofoil with the available experimental data (Kermeen 1956; Akcabay et al. 2014).

5.1 Computational Domain, Boundary Conditions and Grid Generation

The computational domain is shown in Fig. 5.1. Here, the lengths along x, y, and z directions are taken as 18c, 10c, and 1.92c, respectively where c is the chord length of hydrofoil. The domain size for the hydrofoil is selected on the basis of internal assessment and literature review (Huang et al. 2020) such that there is minimal effect of the wall boundaries on the hydrofoil. We have analysed different dimensions of domain varying from 4c to 15c in y direction, as upper and lower surface of the domain are set as no slip condition. The optimum dimension that works for our simulation is 10c, with negligible effect of upper and lower walls

[1] Reprinted with permission from "Numerical simulation and analysis of fluid-structure interaction on 3D MHKF-180 and NACA4418 cavitating hydrofoils by S. Singh, M. Danish, K. Saha, and B.N. Singh, Ocean Engineering 272 (2023)", Copyright 2023 Elsevier Ltd.

on the flow around hydrofoil. The inlet is located at a distance of 6c from the leading edge, whereas the outlet is located at a distance of 12c in the downstream direction of the leading edge. The 3D profiles of NACA66, NACA4418 and MHKF-180 are shown in Fig. 5.2.

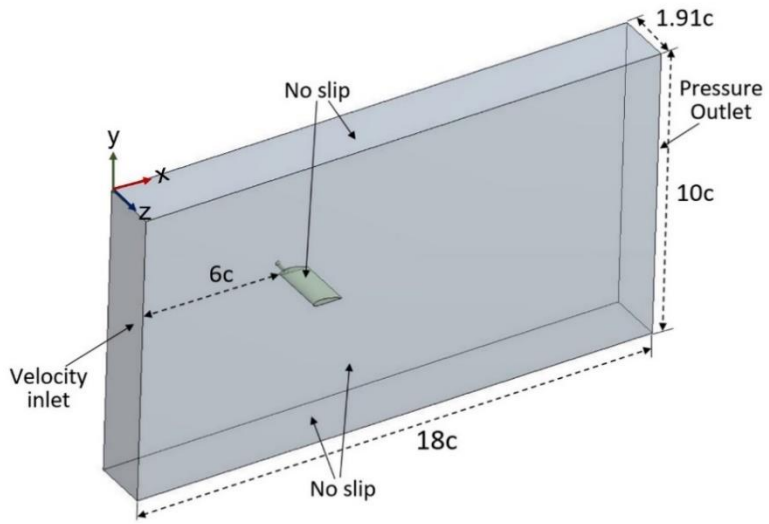

Fig. 5.1. Dimensions and boundary conditions of computational domain around hydrofoil.

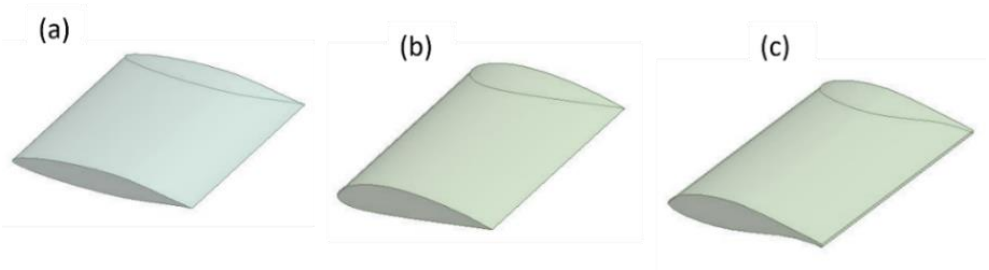

Fig. 5.2. 3D profiles of (a) NACA66, (b) NACA4418 and (c) MHKF-180 hydrofoils.

The computational mesh for fluid zone is generated using unstructured tetrahedral grids as mentioned in section 3.7 of chapter 3. The first cell from the hydrofoil surface is kept as 0.0167 mm and maximum number of layers are 12 with growth rate of 1.81. On the other hand, the hydrofoil structure is discretised using SOLID186 elements, as shown in Fig. 5.3. SOLID186 elements are higher order 20 node hexahedron elements with three degrees of freedom per node in all three directions x, y, and z (Cao et al. 2015; Suzuki et al. 2016; Čupr et al. 2019).

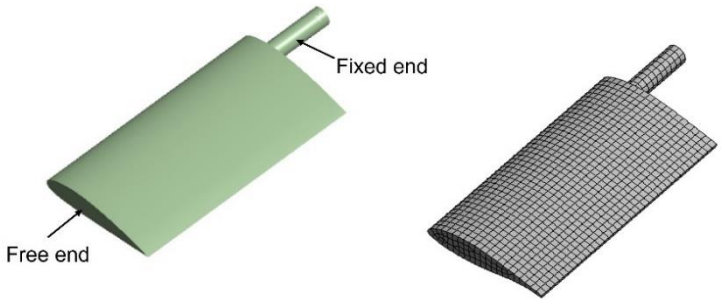

Fig. 5.3. Boundary conditions and meshing of hydrofoil structure.

In the present work, the simulations are performed at Reynolds number (*Re*) 750000, where Reynolds number is defined based on the chord length and freestream velocity. For this Reynolds number, the inlet velocity is found to be 6.7 m/s. The outlet is set at different pressures corresponding to the required cavitation numbers. At the inlet the turbulent intensity of 5% is used. Table 5.1 shows the outlet pressure for all the cavitation number chosen in this work. The hydrofoil and the upper & lower walls of the domain are set as no-slip boundary condition. The specified boundary conditions are shown in Fig. 5.1. For pressure and velocity coupling, the coupled scheme is used. This scheme gives robust solutions by solving the pressure and momentum-based continuity equations simultaneously. PRESTO (Pressure Staggering Option) scheme is used for pressure. The higher order scheme QUICK (Quadratic Upstream Interpolation for Convective Kinetics) is used for volume fraction, momentum, turbulent kinetic energy, turbulent dissipation rate. The time step size is set to 0.001 second and all the results are simulated for physical time of 1.5 sec, while time-averaging is performed after 0.7 sec when the flow get stabilized, where the residuals for the continuity, velocity, and turbulent quantities have reached smaller than 10^{-4}. For transient flow, second order implicit method has been used and for the time step taken the average Courant number comes out to be ≤ 2.4.

For the structural part, one end of the hydrofoil is kept as free, while the other end is fixed using a cylinder of diameter 0.015 m, as shown in Fig. 5.3 (Huang et al. 2019). Other properties of fluid and structure, like density, dynamic viscosity, Young's modulus, Poisson's ratio etc are given in Table 5.2.

Table 5.1. Outlet pressure for different cavitation numbers

Cavitation number (σ)	**Outlet Pressure (Pa)**
0.5	14358
0.8	21072
1.0	25547
1.2	30023
1.5	36736
2.0	47925
2.3	54638
2.5	59114

Table 5.2. Fluid and structure properties

p_v = 3169 Pa	ρ_l = 997 kg/m³
ρ_v= 0.02308 kg/m³	μ_l = 8.9 x10^{-4} kg/(ms)
μ_v = 9.87 x 10^{-6} kg/(ms)	ρ_s = 7800 kg/m³
E = 210 GPa	ν = 0.3

5.2 Grid Independency Test and Result Validation

In this section the grid independence test and result validation has been presented for non cavitating NACA66 and NACA4412 hydrofoils.

5.2.1 Grid-Independency Test

The grid independency test is a crucial step in any numerical simulation which is performed to obtain the optimum number of cells such that the results become independent of the grid size. For this purpose, four different grids are taken for hydrodynamic simulation, where Grid 1 has 0.6 million cells, Grid 2 has 1 million cells, Grid 3 has 1.3 million cells, and Grid 4 has 1.5 million cells. On the other hand, for structural analysis, the four different grids having the number of elements as 7k, 12k, 18k, and 23k are taken.

The grid-independency test for hydrodynamic simulation is performed in terms of cavity length and pressure coefficient. The cavity length on the suction side of the hydrofoil at 4^0 angle of attack with $\sigma = 1$ and Re =750000 computed using four different grids is presented in Fig. 5.4. Similarly, in Fig. 5.5, the pressure coefficient curves obtained by using these grids are presented. Here x-axis represents the normalized distance from the nose of hydrofoil and

y-axis represents the negative of pressure coefficient (-C_p). From these results, it can be observed that the cavity length and pressure coefficient (-Cp) for grids Grid 3 and Grid 4 are almost overlapping with each other, therefore Grid 3 with 1.3 million cells can be considered as grid independent for hydrodynamic analysis. Hence, all the results presented here onward in this paper are performed using 1.3 million cells.

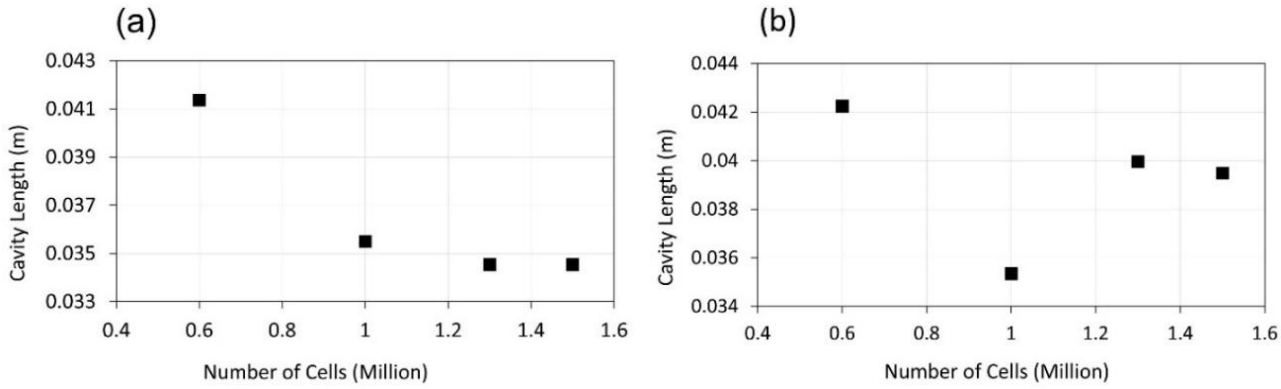

Fig. 5.4. Variation of cavity length with number of grids for (a) NACA4418 and (b) MHKF-180 hydrofoil for α = 4^0, $\sigma = 1$.

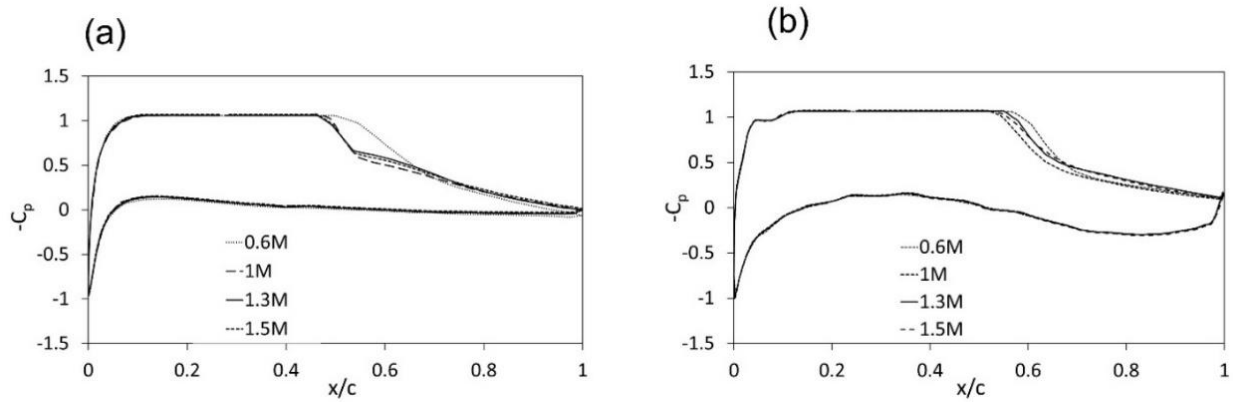

Fig. 5.5. Pressure coefficient curve for (a) NACA4418 and (b) MHKF-180 hydrofoil at different grids for α = 4^0, $\sigma = 1$.

For the grid-independency test of structural analysis, the natural frequency is computed using grids of elements 7k, 12k, 18k, and 23k. The natural frequency of stainless steel MHKF-180 and NACA4418 hydrofoil is determined using the acoustic modal analysis for fully wetted condition under still water. Both the hydrofoils are considered as cantilever beam of chord length 0.1 m, span 0.191 m, and 4^0 angle of attack. The hydrofoil is fixed at one end using 0.015 m diameter cylinder extension located at 25% of chord length (Huang et al. 2019). Fig. 5.6, shows the first bending and torsional frequencies for NACA4418 and MHKF-180

hydrofoils with respect to different number of elements. Comparing the values, we find that there is slight difference between the results for 18k and 23k, so the grid of 18k elements can be treated as grid independent. Thus, for structural analysis, the grid with 18k elements is used in this paper. The bending and torsional deformation corresponding to 18k elements for both the hydrofoils are shown in Fig. 5.7 and 5.8. It can be observed in Fig. 5.7, that the deformation due to bending of the hydrofoils is gradually increasing from root to tip. In case of NACA4418 the maximum tip deformation is found as 46.32 mm whereas for MHKF-180 it is found as 48.40 mm. Thus, based on tip deformation we can say that the MHKF-180 is bending more as compared to NACA4418. For torsional deformation it is observed that maximum deformation for both the hydrofoils is at mid-section of the trailing edge and at the nose of the hydrofoil near the tip as shown in Fig 5.8. The maximum torsional deformation of NACA4418 is 66.30 mm and for MHKF-180 it is 71.50 mm. From this comparison it is observed that MHKF-180 is deforming more under torsion also.

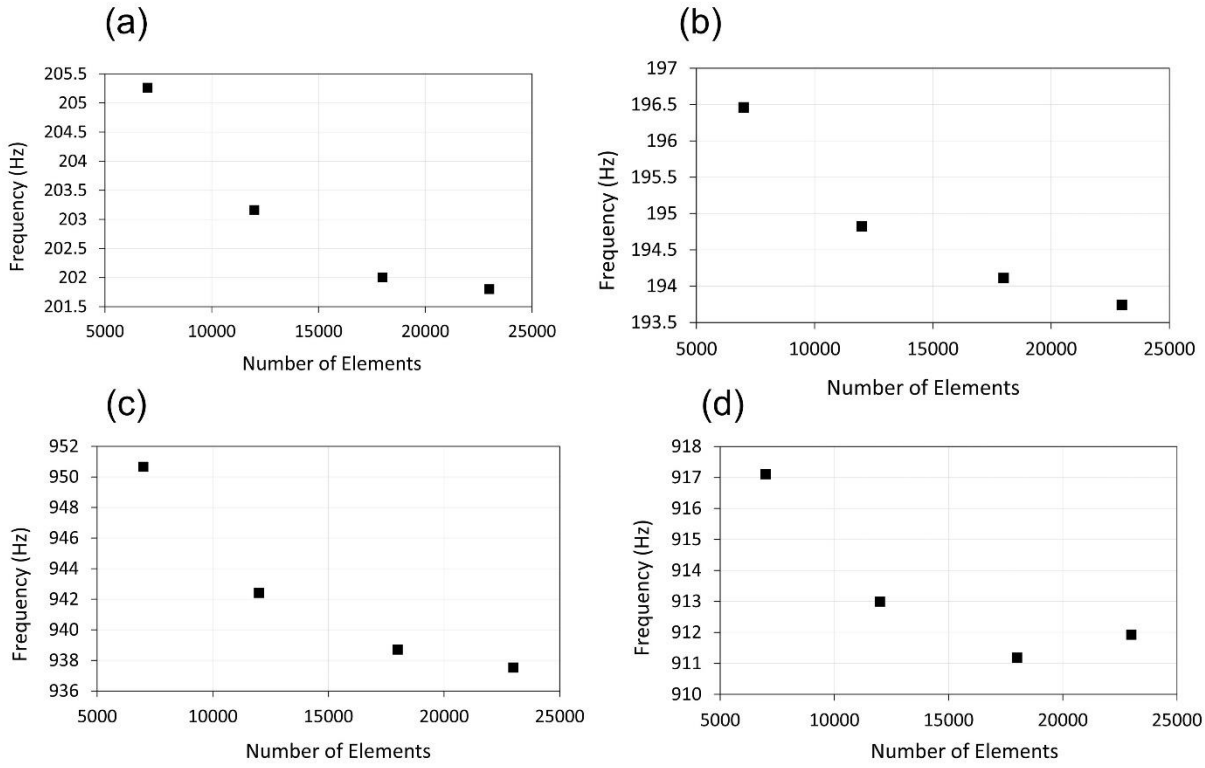

Fig. 5.6. Frequency of first bending modes ((a) NACA4418, (b) MHKF-180) and first torsional mode ((c) NACA4418, (d) MHKF-180) at different grids elements.

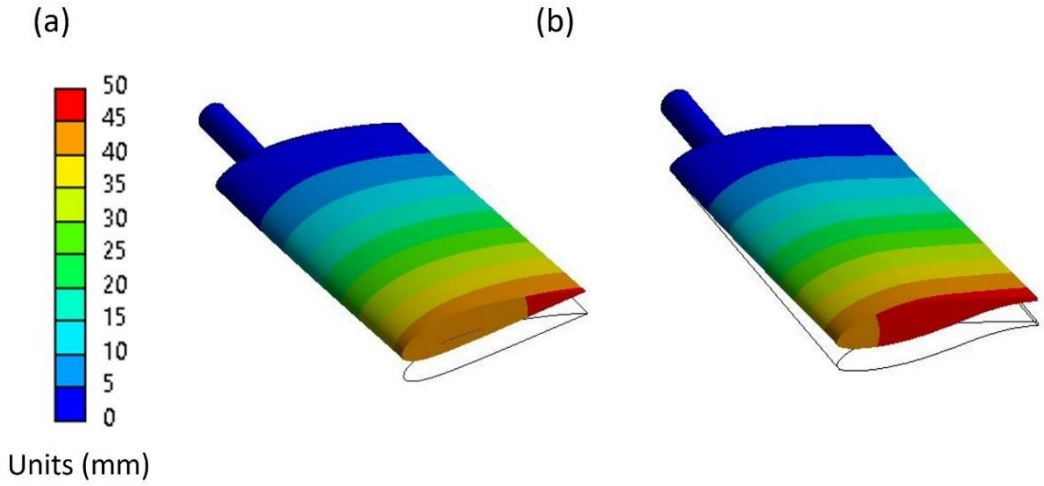

Fig. 5.7. First bending mode shapes of (a) NACA4418 and (b) MHKF-180 hydrofoils at $\alpha = 4^0$.

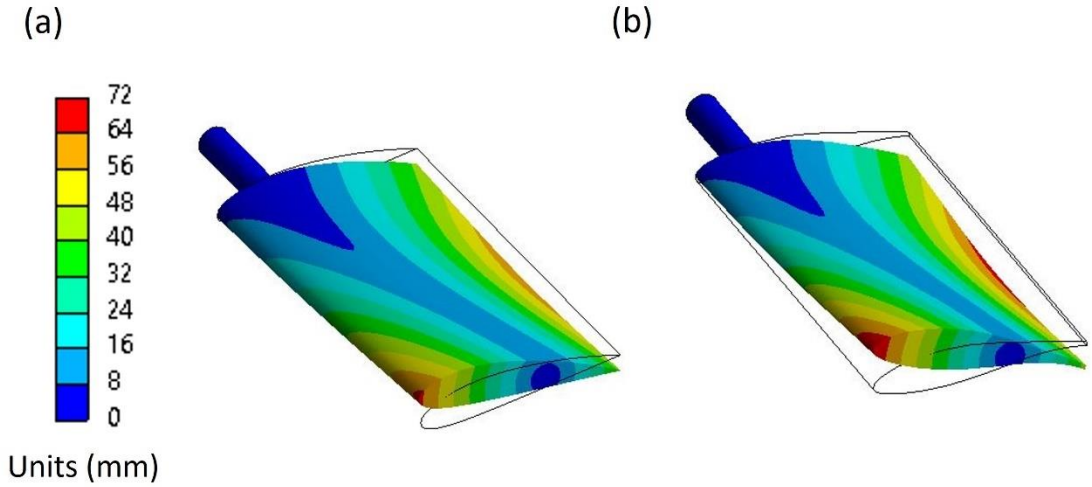

Fig. 5.8. First torsional mode shapes (a) NACA4418 and (b) MHKF-180 hydrofoils at $\alpha = 4^0$.

5.2.2 Results Validation

In this section, the results are validated for pressure coefficient *(C_p)* and the natural frequency of 3D NACA66 hydrofoil of chord length 0.15 m, span 0.191 m, and angle of attack as 8º. The C_p results are compared against experimental results reported by Akcabay et al. (2014). Fig. 5.9 compares the negative pressure coefficient curve *(-C_p)* with the experimental result along the hydrofoil surface. The solid line represents the numerical result, and the symbols show the experimental data. Clearly, from the comparison, it can be concluded that the present result is in good agreement with the experimental result.

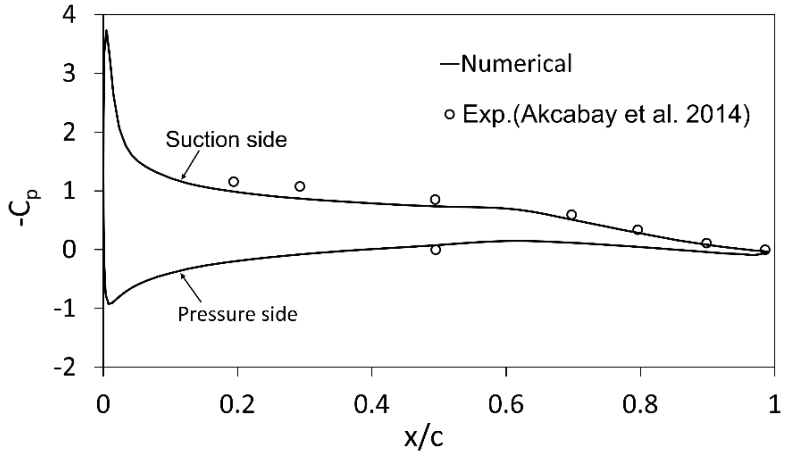

Fig. 5.9. Comparison of negative pressure coefficient (-C_p) curve with experimental data along 3D NACA66 hydrofoil at $\alpha = 8^0$.

For structural model validation, the natural frequency of NACA66 stainless-steel hydrofoil in still water for fully wetted condition, is compared with the experimental data given by Ducoin et al. (2012a). The acoustic modal analysis is used to determine the natural frequency of the hydrofoil. The stainless-steel hydrofoil is partially fixed at one end using cylindrical extension of diameter 0.015 m at x/c =0.25, and the tip section is set as free (Ducoin et al. 2012a; Huang et al. 2019). Ducoin et al. (2012a) have reported the range for the first and second natural frequency as 115-120 Hz and 410-430 Hz, respectively. In the present work these frequencies are found as 113.44 Hz and 409 Hz. Clearly, these values are close to the values mentioned by Ducoin et al. (2012a).

Similarly, for validating the results for cavitating case, the numerically computed results on hydrofoil NACA4412 are compared with the experimental work done by Kermeen (1956) as shown in Fig. 5.10. Kermeen performed his experiment on 3D NACA4412 at Re = 0.8 x 10^6 for different cavitation numbers at an angle of attack $\alpha = 8^0$. Fig. 5.10 (a) shows the comparison of time averaged lift coefficient (C_l) for varying σ ranging from 0.3 to 1.5. It is observed that with the increasing σ there is increase in the pressure difference on the hydrofoil surface which gradually increases the C_l values, which become almost constant for larger cavitation numbers. Similarly, Fig. 5.10 (b) shows the comparison of time averaged drag coefficient (C_d) at different value of σ. Initially with the increase in cavitation number the C_d increases and attains it maximum value, and then again starts decreasing. Clearly, from the above comparison, it is observed that our numerical results are in good agreement with the experimental data (Kermeen 1956). Next, in the following sections, the hydrodynamic and structural results for MHKF-180 and NACA4418 hydrofoils are presented and discussed.

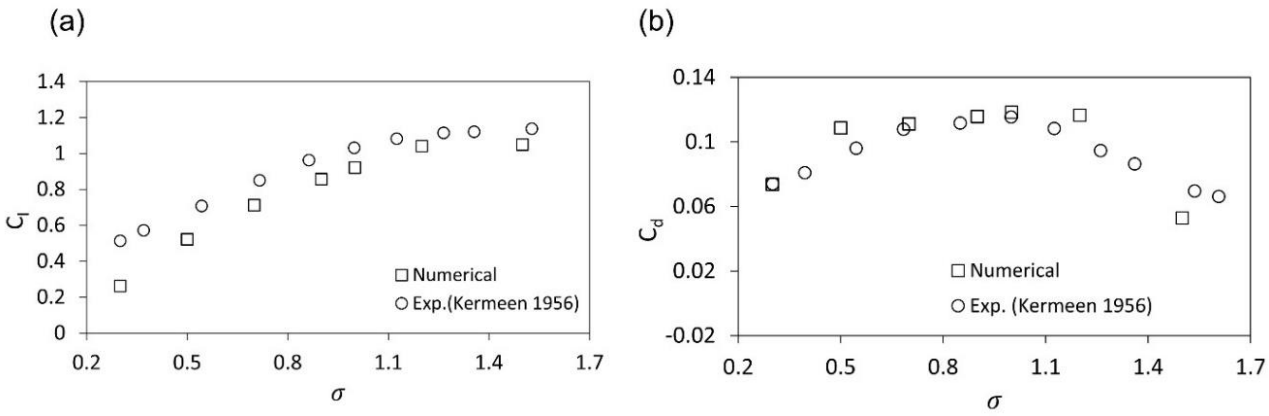

Fig. 5.10. Time averaged lift coefficient of NACA4412 hydrofoil for different cavitation numbers at $\alpha = 8^0$.

5.3 Hydrodynamic and Structural Performance of Cavitating MHKF-180 and NACA4418 Hydrofoils

5.3.1 Transient Behaviour of Cavitating Flow at $\sigma = 1$ and $\alpha = 8°$

The cavity formation is a cyclic behaviour consisting of three stages i.e., initiation, growth, and extinction. At the beginning of cycle, the cavity starts forming near the leading edge, and then extend towards the trailing edge. During growth stage, the fully developed cavity tries to cover the entire span of hydrofoil. The maximum length of cavity is observed during growth stage (Kim et al. 2018). Fig. 5.11 shows one cycle of cavity growth on MHKF-180 and NACA4418 hydrofoil at 8^0 angle of attack and σ =1. After this cavity breaks and shed from the hydrofoil. The growth and shedding of cavity on hydrofoil is the continuous process and most of the time the cavity is not uniform along the spanwise direction (Wu et al. 2018). At t =1.11 sec, the cavity on NACA4418 hydrofoil is unstable and covering the hydrofoil partially, while MHKF-180 has comparatively stable cavity covering almost 80% of chord length of the hydrofoil along the span. At t = 1.17 sec, the NACA4418 has larger cavity as compared to MHKF-180 till t =1.23 sec, after which it starts decreasing and covers only 40% of the chord for t=1.29 and t =1.35 sec. For MHKF-180, at t=1.29 sec and t=1.35 sec the cavity is unstable, hence it is curled into a concave shape at the trailing edge before it gets separated from the hydrofoil. Overall, the cavity on the NACA4418 hydrofoil is mostly attached to the hydrofoil surface, whereas the cavity on MHKF-180 gets separated along the thick trailing edge.

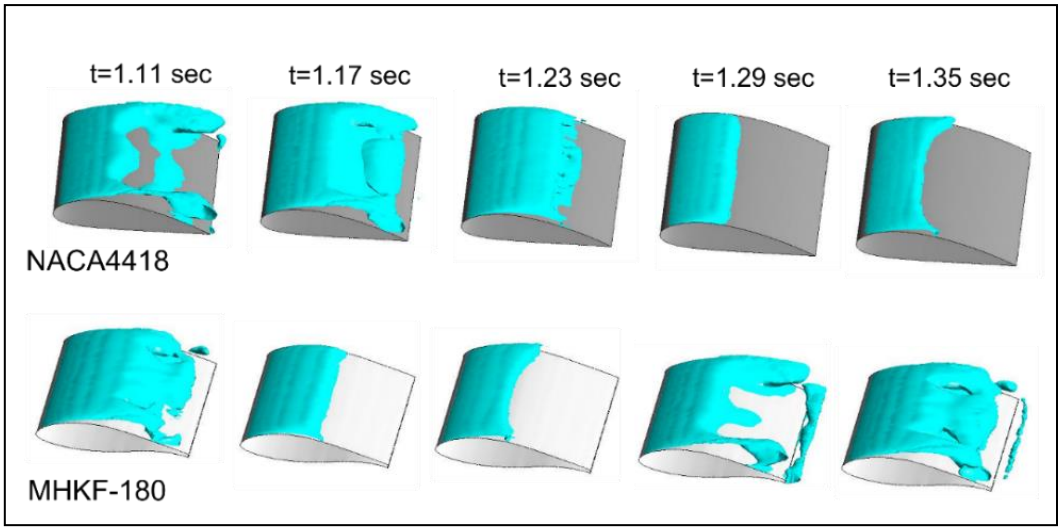

Fig. 5.11. Cavity growth with time for NACA4418 and MHKF-180 at α = 10^0 and σ = 1.

Fig. 5.12 presents the normalized x-component velocity profiles along the vertical lines on MHKF-180 and NACA4418 hydrofoils at different chord-based locations for α =8^0 and σ =1 at time instant t =1.5sec. The chord-based locations are x/c =0, 0.2 0.4, 0.6, 0.8, 1, where x/c = 0 is the leading edge of the hydrofoil and x/c =1 is the trailing edge. The positive velocity gradient represents that the flow is attached to the hydrofoil surface, while the negative gradient shows the flow separation. It is observed that near the nose of both the hydrofoils (x/c=0, 0.2), the flow is attached to the hydrofoil surface hence, the velocity gradients are positive at these locations. On MHKF-180, the flow gets separated at locations x/c =0.6, 0.8 and 1 as shown in Fig. 5.12 (d-f). For NACA4418 the flow gets separated completely at the sharp trailing edge, x/c=1. There is a reverse flow at the trailing edge of both the hydrofoils therefore, giving negative velocity gradients. For most of the locations on the hydrofoil, the MHKF-180 has larger gradients due to the thicker cavity in a spanwise direction (Hong et al. 2017).

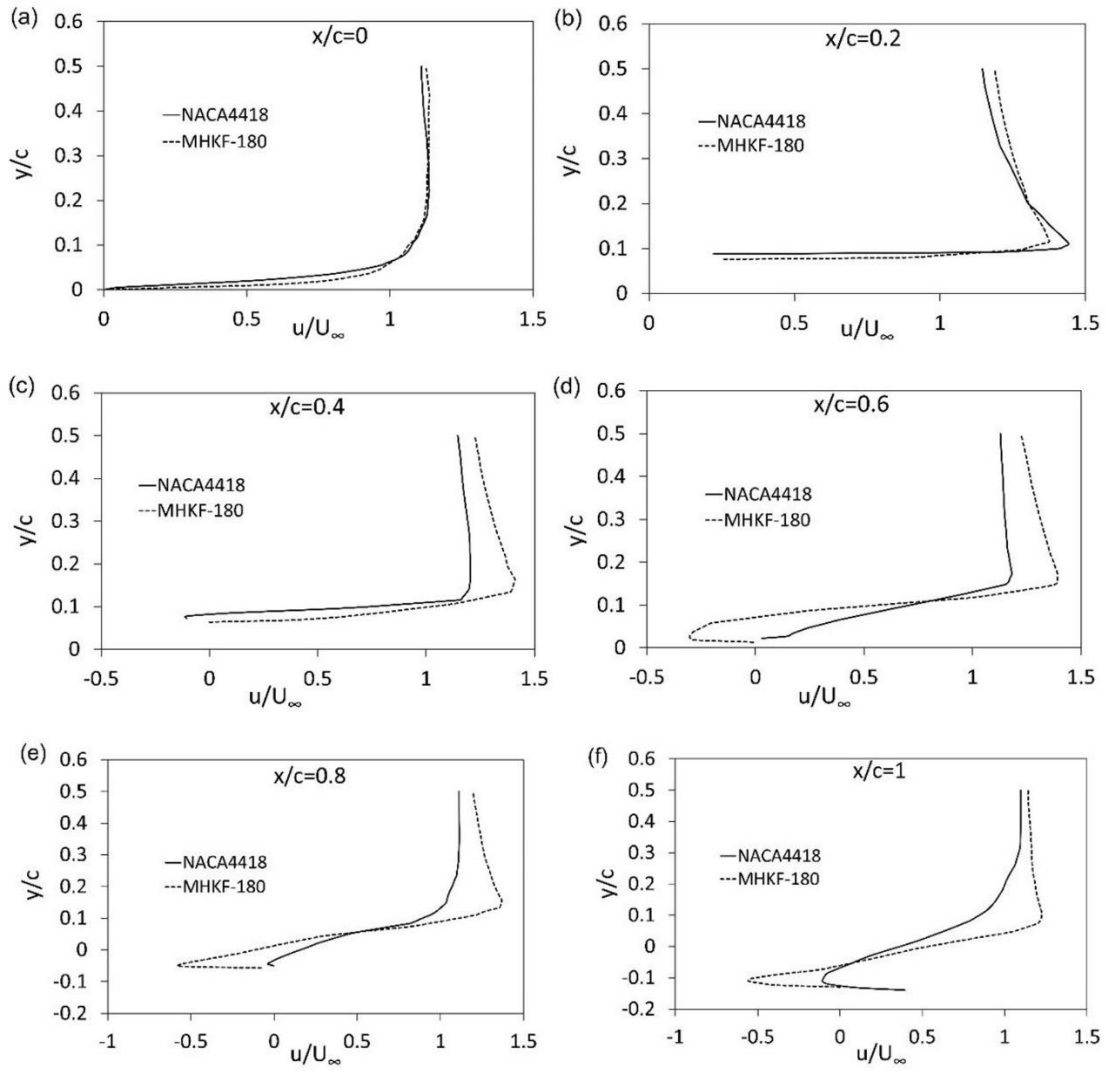

Fig. 5.12. Comparison of axial velocity profiles at (a) x/c=0, (b) x/c=0.2, (c) x/c=0.4, (d) x/c= 0.6, (e) x/c=0.8, (f) x/c=1 along the MHKF-180 and NACA4418 hydrofoils at $\alpha = 8,^{0}$ and $\sigma = 1$ at time instant t=1.5 sec.

Fig. 5.13. shows the instantaneous streamlines distribution at three different planes (z/c = -0.7, 0 and 0.7) along the span wise direction for NACA4418 and MHKF-180 at $\alpha = 8^{0}$ and σ =1. For both the hydrofoils the streamlines are irregular at these three planes. The upper surface of the hydrofoil has the maximum velocity, and it decreases along the trailing edge where reverse flow can be observed. At z/c = 0, a larger recirculation zone can be observed for NACA4418 hydrofoil, whereas MHKF-180 has comparatively smoother flow. MHKF-180 has some flow recirculation at z/c = -0.7. On comparing the flow separation patterns near the trailing edge, it is observed that streamline curvature of NACA4418 is more abrupt than MHKF-180 hydrofoil due to its sharp trailing edge.

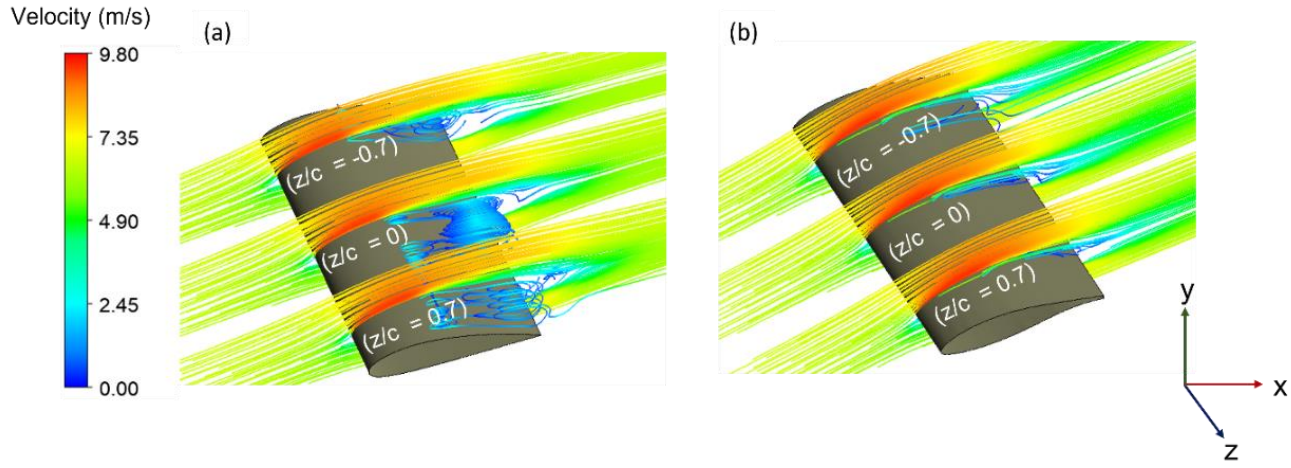

Fig. 5.13. Streamline distribution for (a) NACA4418 and (b) MHKF-180 at α = 8^0 and σ =1 at time instant t =1.5 sec.

5.3.2 Time-Averaged Results at Different Angles of Attack with Fixed Cavitation Number ($\sigma = 1$)

The time-averaged lift coefficient for 3D MHKF-180 and NACA4418 hydrofoils is shown in Fig. 5.14 (a) at seven different angles of attack in the range 0^0 to 12^0 with $\sigma = 1$. It is observed that there is an increase in lift coefficient with an increase in angle of attack. Since, the increase in the angle of attack increases the pressure difference between upper and lower hydrofoil surface, thus results in the higher value of lift coefficient. The minimum value of lift coefficient is obtained at 0^0 for both MHKF-180 and NACA4418 hydrofoil with the value of 0.58 and 0.38, respectively, while the maximum value of lift coefficient for MHKF-180 is found as 1 and 0.86 for NACA4418. At α = 0^0, the maximum percentage difference of 29% is obtained between the lift coefficient values of NACA4418 and MHKF-180 hydrofoils. Further, it can be seen from the figure that for all angles of attack the C_l is always higher for MHKF-180 than NACA4418. Thus, based on these results, it can be concluded that MHKF-180 performs better in terms of C_l than NACA4418.

Next, the time-averaged drag coefficient of 3D MHKF-180 and NACA4418 is shown in Fig. 5.14 (b). The drag force on hydrofoil is the sum of skin friction drag and pressure drag. The skin friction drag is developed due to the viscous drag, while pressure drag is developed because of shape and size of the hydrofoil. The thicker is the hydrofoil, higher the pressure drag (Anderson 2011). Like C_l, C_d is also found to increase with an increase in angle of attack. Further, the value of C_d for MHKF-180 is slightly higher than that for NACA4418. The reason for higher drag in case of MHKF-180 may be attributed to its trailing edge thickness and its

increased frontal contact area. Fig. 5.14 (c) presents the lift to drag ratio of hydrofoils at different angles of attack. Initially, the l/d is increases with increase in angle of attack and attains it maximum value. For 0^0 and 2^0, the lift of MHKF-180 is higher than the NACA4418, while drag is almost same which is results in higher l/d ratio of MHKF-180 hydrofoil. The maximum value of l/d is obtained at 2^0 for MHKF-180 and NACA4418 hydrofoil. For higher angle of attack the l/d ratio is almost same for both the hydrofoil which decrease with increase in angle of attack.

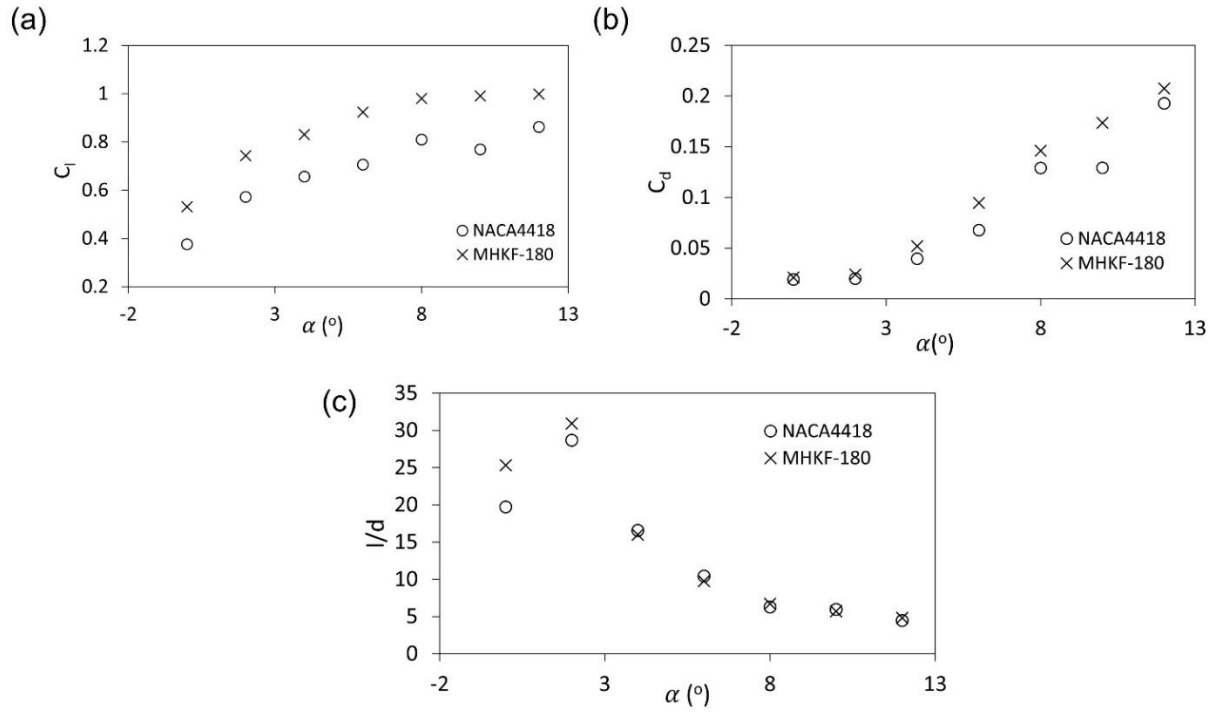

Fig. 5.14. Comparison of (a) lift coefficient, (b) drag coefficient, and (c) l/d for MHKF-180 and NACA4418 for different α at $\sigma = 1$.

In Fig. 5.15 (a), the vapor cavity length for MHKF-180 and NACA4418 is shown at different angles of attack varying between 0^0 and 12^0 with $\sigma = 1$. The vapor cavity is generally formed on the suction surface of the hydrofoil for positive angles of attack, as it has lower pressure compared to the pressure surface. The cavity length is calculated on the suction surface of midplane of the hydrofoils. The vapor fraction is also shown on this plane in Fig. 5.15 (b). It is observed that the cavity length is increasing with the angle of attack. At 0^0 there is no cavity formation on both the hydrofoils, however it starts forming at 2^0. The maximum length of the cavity is observed at 6^0 for MHKF-180 while at 12^0 for NACA4418.

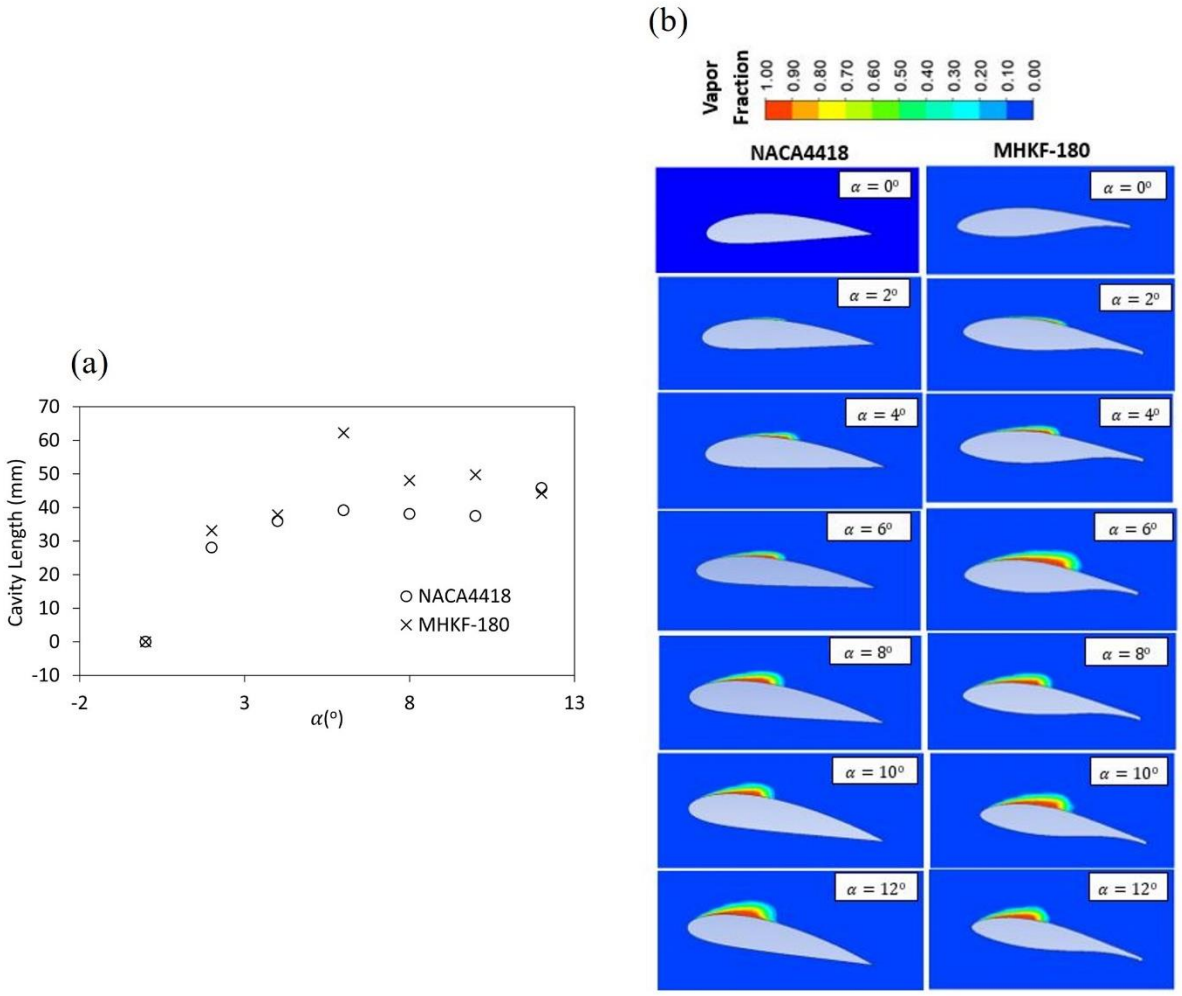

Fig. 5.15. Comparison of (a) cavity length and (b) vapor fraction of MHKF-180 and NACA4418 for different α at $\sigma = 1$.

For Strouhal number, the frequency is obtained by performing fast-Fourier-transform of the lift coefficient. In Fig. 5.16, the Strouhal number for MHKF-180 and NACA4418 at different angles of attack with $\sigma = 1$ is shown. It is observed that the maximum value of Strouhal number is obtained at 0^0 for both hydrofoils. However, this value is significantly higher for NACA4418 than MHKF-180, possibly because at 0^0 there is no cavity on both the hydrofoils and NACA4418 has sharp trailing edge, causing the generation of higher frequency vortices as compared to MHKF-180. On the other hand, the Strouhal number is found to decrease with an increase in the angle of attack. This observation is consistent with what was reported in literature (Kurtulus 2015; Zhao et al. 2018). Moreover, it should be noted that for angle 6° and beyond the Strouhal is almost same for both hydrofoils, whose value is found to be close to 0.192.

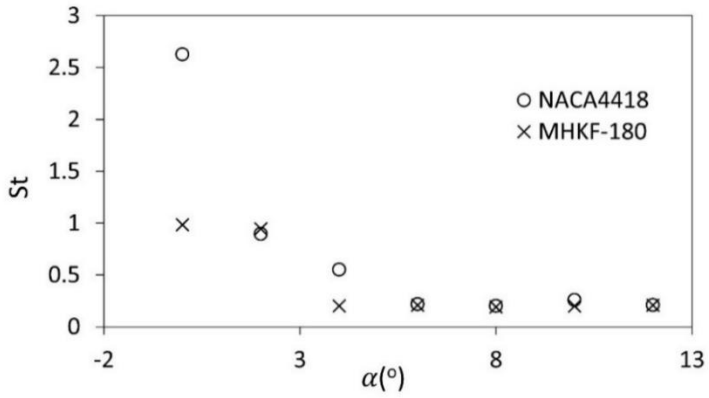

Fig. 5.16. Strouhal number with angle of attack for MHKF-180 and NACA4418 hydrofoils, $\sigma = 1$.

Fig. 5.17 shows the tip maximum deformation with angle of attack for MHKF-180 and NACA4418 hydrofoils. The y-axis represents the maximum tip deformation in mm and the x-axis represent the angle of attack. It has been reported in literature that the tip deformation usually increases with the angle of attack and cavity length (Ducoin et al. 2010a, 2012b; Huang et al. 2019). A similar trend is found from our simulation. Moreover, the maximum tip deformations for MHKF-180 is obtained at 6^0 and for NACA4418 at 12^0, which is consistent to maximum vapor cavity length found at 6^o and 12^o, respectively for MHKF-180 and NACA4418 (Fig. 5.15 (a)). For the structure to be safe from failure, the maximum deflection in the cantilever beam must be below the permissible limit of the structure member, i.e., less than span/120 (IS:800-2007). Considering this it can be seen that for cantilevered hydrofoil with span of 191 mm, the deformations should be less than 1.6 mm. Now, to check the structural strength, it is also important to find stresses developed in the hydrofoil. In Table 5.3, the maximum von-Mises stresses with angles of attack are presented for the hydrofoils. The maximum stress for MHKF-180 is found to be 95.63 MPa at 6^0 and for NACA4418 it is found as 78.63 MPa at 12^0.

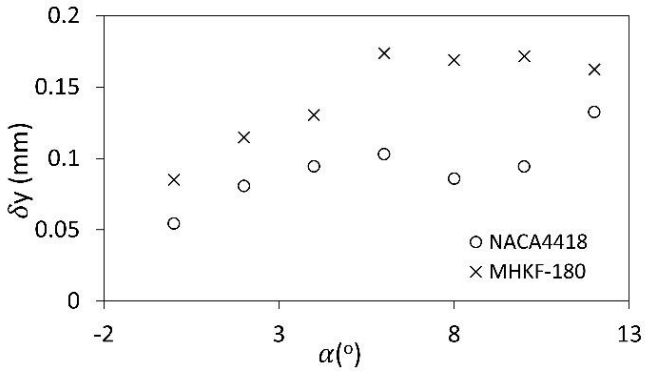

Fig 5.17. Tip maximum deformation of MHKF-180 and NACA4418 hydrofoils at different α for $\sigma = 1$.

Table 5.3. Maximum von-Mises Stress at different angles of attack (α).

α (^{o})	Maximum stress (MPa)	
	NACA4418	**MHKF-180**
0	34.09	45.48
2	44.59	60.21
4	70.12	65.60
6	74.86	95.63
8	60.12	77.48
10	60.46	89.36
12	78.63	91.27

In the above section, a comparison of hydrodynamic and structural results for MHKF-180 and NACA4418 hydrofoil were presented at fixed cavitation number but at different angles of attack. And the major takeaways are the following: (a) the vapor cavity is thicker on MHKF-180 hydrofoil than NACA4418, (b) the lift coefficient value of MHKF-180 is higher as compared to NACA4418 hydrofoil at all angles of attack, (c) the drag coefficient is also higher for MHKF-180 than NACA4418 due to added trailing edge thickness, (d) the Strouhal number for both MHKF-180 and NACA4418 hydrofoil is almost same at α = 6^0, 8^0, 10^0 and 12^0, (e) the tip deformation and von-Mises stress developed in MHKF-180 is higher as compared to NACA4418 hydrofoil at all angles of attack. In the next section, the performance of MHKF-180 and NACA4418 hydrofoils is analysed at different cavitation numbers with a fixed angle of attack.

5.3.3 Time-Averaged Results at Different Cavitation Numbers For Fixed Angle of Attack ($\alpha = 8^o$)

In Fig. 5.18 (a), a comparison of time-averaged lift coefficient of 3D MHKF-180 hydrofoil and NACA4418 is presented at $\alpha = 8^0$ for different cavitation numbers ranging from 0.5 to 2.5. It is observed that with an increase in the cavitation number, the lift coefficient increases and it became constant as it moves towards non-cavitating condition , which is consistent with the results reported in literature (Zhao et al. 2018). At lower cavitation numbers, the suction side of the hydrofoil is covered with a larger cavity producing lower pressure difference on the hydrofoil and, therefore, lower values of lift coefficient. Further, as the cavitation number

increases, the cavity on the hydrofoil decreases, and the pressure difference increases resulting in a higher lift coefficient. The maximum value of lift coefficient is obtained at $\sigma = 2.3$ for both the MHKF-180 and NACA4418 hydrofoils with maximum value of 1.39 and 1.115, respectively, and this value remains constant for higher cavitation numbers as non-cavitating condition is already reached. The maximum percentage difference of 24.6% is obtained between the lift coefficient value of MHKF-180 and NACA4418 at σ = 0.5. On comparing the results of C_l, MHKF-180 is found to have higher lift coefficient than NACA4418 for all cavitation numbers. Clearly, MHKF-180 is performing better.

Similarly, in Fig. 5.18 (b) the comparison of time averaged drag coefficient of 3D MHKF-180 hydrofoil with NACA4418 is presented at $\alpha = 8^0$ for different cavitation numbers. It is observed that drag coefficient is almost constant for lower value of cavitation number i.e., $\sigma = 0.5,0.8,1$. Further, the drag coefficient decreases with the increase in cavitation number and remains constant for σ >2. This decrease in drag coefficient is due to decrease in skin friction drag (Anderson 2011). The maximum difference in drag coefficient value of NACA4418 and MHKF-180 is obtained at σ =1.2. For cavitating condition the MHKF-180 hydrofoil has comparatively higher drag than NACA4418 for all cavitation numbers but for non-cavitating condition both the hydrofoils have almost same drag coefficient.

The other parameter for studying the hydrodynamic performance of hydrofoil is lift to drag ratio which is shown in Fig. 5.18 (c). It is observed that l/d increases with the increase in cavitation number and attains its maximum value at σ=2, and beyond this l/d becomes constant. For cavitating condition till σ = 1.5, l/d for both the hydrofoils are almost equal but as it moves towards non-cavitating condition, the l/d of MHKF-180 is much higher than the NACA4418 due to its higher lift coefficient values.

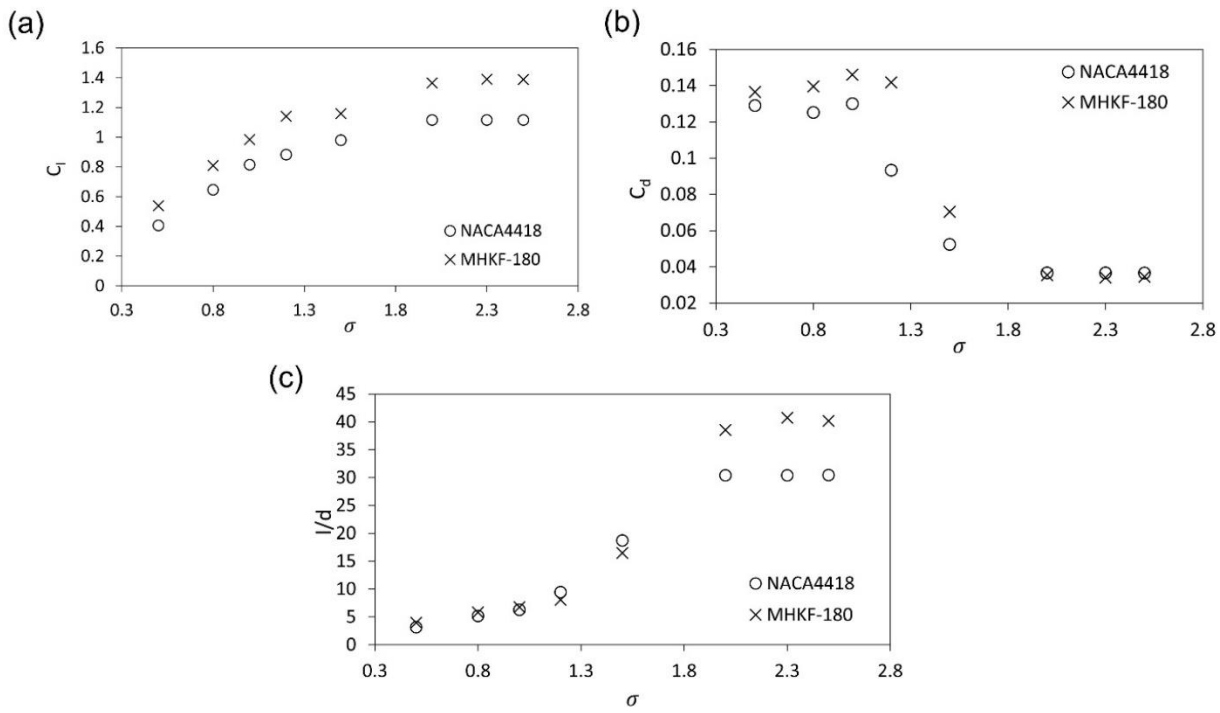

Fig. 5.18. Comparison of (a) lift coefficient, (b) drag coefficient, and (c) l/d for MHKF-180 and NACA4418 at different σ for $\alpha = 8^0$.

In Fig. 5.19 (a) and (b), the vapor cavity length and vapor volume fraction for MHKF-180 and NACA4418 are shown for different cavitation numbers ranging from 0.5 to 2.3 and $\alpha = 8^0$. It is observed that there is a larger cavity covering the hydrofoil suction surface at a lower cavitation number, and as the cavitation number increases, the cavity length decreases. The maximum cavity is obtained at $\sigma = 0.5$, for both the hydrofoils. At σ = 2, there is no cavity on NACA4418 while MHKF-180 has observable amount of cavity on the upper surface as shown in Fig. 5.19 (b). Therefore, there is maximum difference between the cavity length of NACA4418 and MHKF-180 at σ = 2. The vapor cavity formed on the hydrofoil can also be understood with the help of the pressure coefficient curve which is defined based on pressure distribution on the hydrofoil surface. The length over which the pressure coefficient remains constant defines the cavity length (Štigler 2009; Huang et al. 2010; Wu and Chen 2016). The pressure coefficient curve on the middle section of NACA4418 and MHKF-180 hydrofoils for different cavitation numbers is shown in Fig. 5.20 (a) and (b), respectively. For almost all cavitation numbers, MHKF-180 has a larger cavity than NACA4418 hydrofoil.

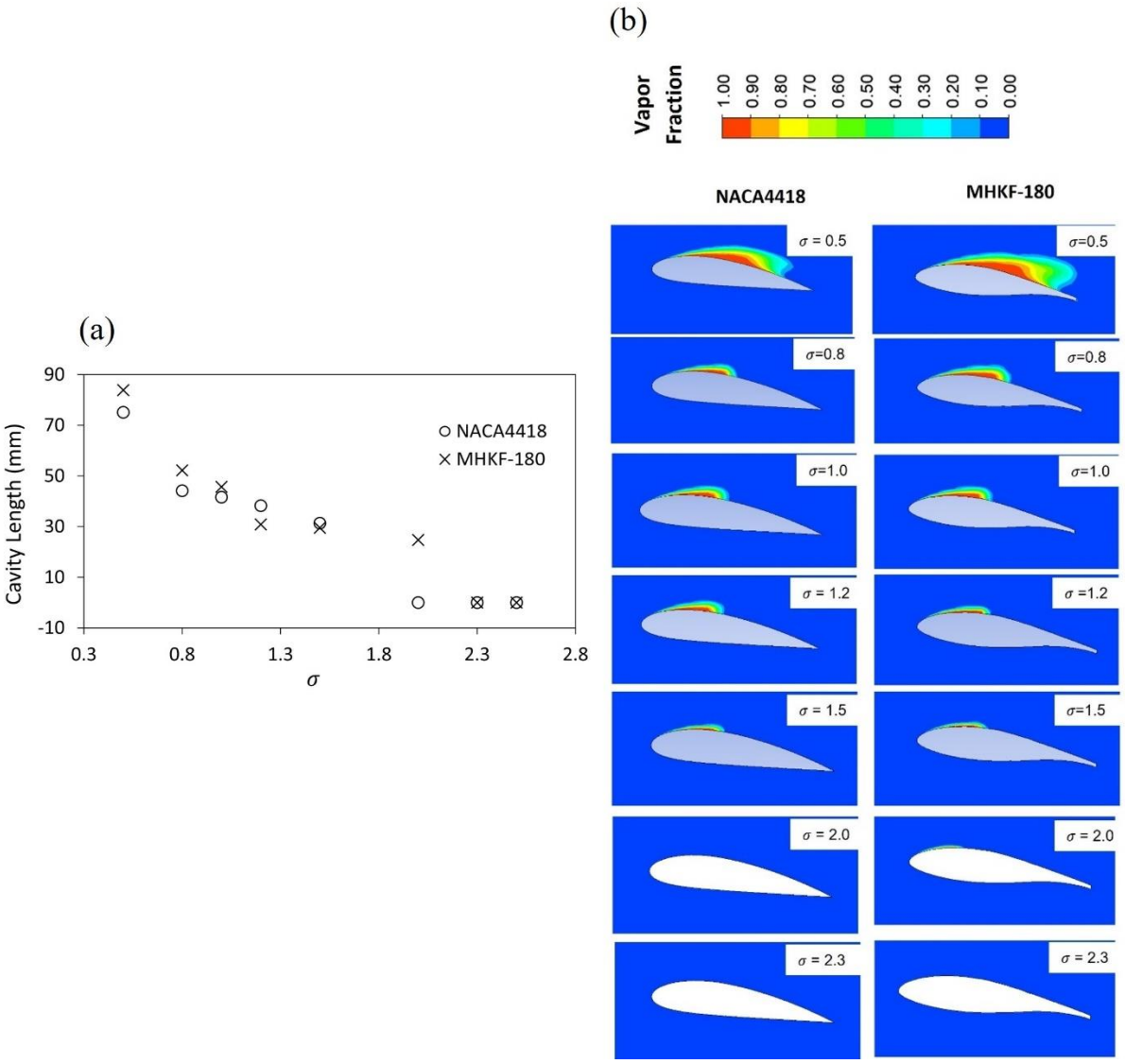

Fig. 5.19. Comparison of (a) cavity length and (b) vapor fraction of MHKF-180 and NACA4418 for different σ at $\alpha = 8^0$.

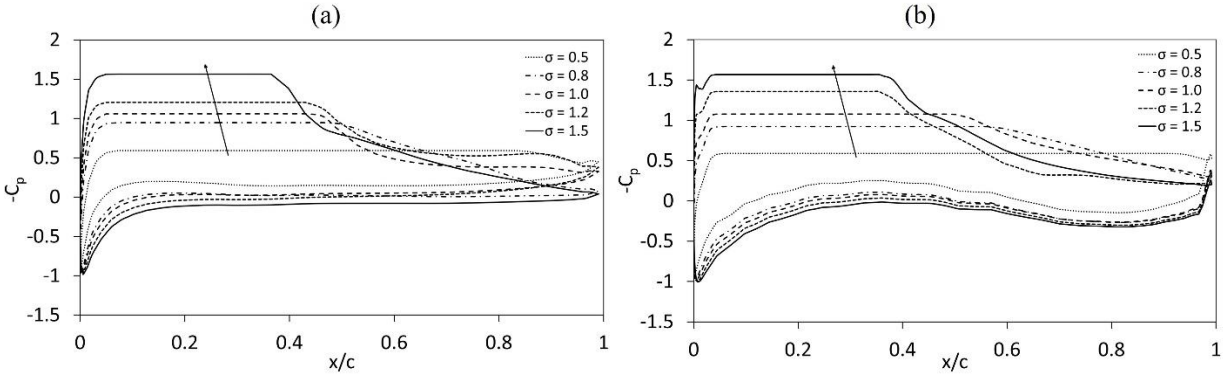

Fig. 5.20. Pressure coefficient curve for (a) NACA4418 and (b) MHKF-180 hydrofoils at different σ for $\alpha = 8^0$.

In Fig. 5.21, the comparison of Strouhal number for MHKF-180 and NACA4418 hydrofoil is presented at different cavitation numbers for $\alpha = 8^0$. It is observed that the Strouhal number increases with the increase in cavitation number and again drops for non cavitating condition and remains constant. This is in line with the observation made in earlier reported works (Dular and Bachert 2009; Luo et al. 2012; Carrat et al. 2017). The minimum value of the Strouhal number for both the hydrofoils is obtained at $\sigma = 0.5$ and maximum value at $\sigma = 1.2$. On overall comparison, MHKF-180 has a slightly lower Strouhal number for cavitating condition than NACA4418 due to lower shedding frequency and larger cavity for almost all cavitation numbers.

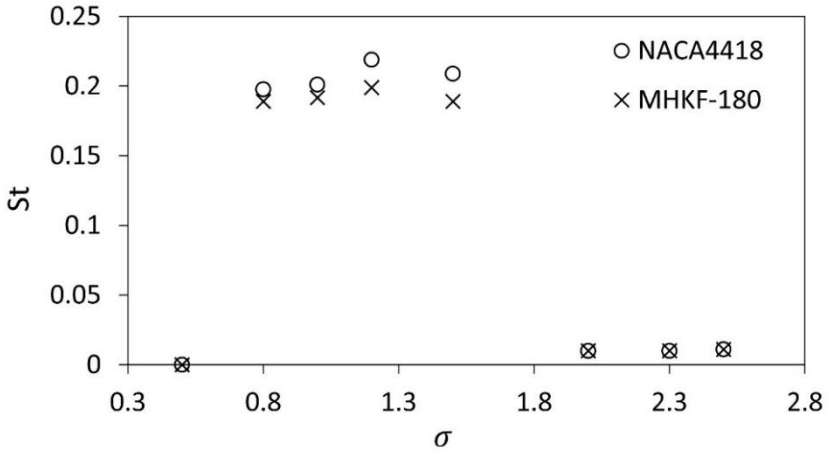

Fig. 5.21. Strouhal number comparison for MHKF-180 and NACA4418 at cavitation numbers and $\alpha = 8^0$.

In Fig. 5.22, the comparison of tip maximum deformation of 3D MHKF-180 hydrofoil with NACA4418 hydrofoil at different cavitation numbers is presented for $\alpha = 8^0$. It is observed that the tip deformation increases with the increase in cavitation number. For MHKF-180, the maximum deformation is obtained at $\sigma = 2.3$ and for NACA4418 at $\sigma = 1.2$. In Table 5.4, the comparison of maximum von-Mises stress for MHKF-180 and NACA4418 hydrofoils is given for different cavitation numbers. The maximum stress that MHKF-180 is subjected to is 112.88 MPa at $\sigma = 1.5$, whereas NACA4418 has maximum stress of 93.73 MPa at $\sigma = 1.2$. Comparatively, it can be stated that MHKF-180 has larger deformation and high stresses than NACA4418 at all cavitation numbers.

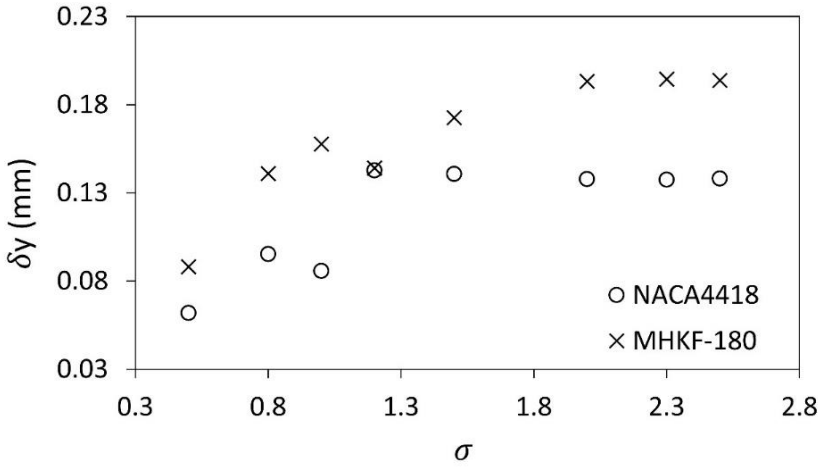

Fig. 5.22. Tip maximum deformation of MHKF-180 and NACA4418 hydrofoils at different cavitation numbers for $\alpha = 8^{o}$.

Table 5.4. Maximum von-Mises Stress at different cavitation numbers (σ)

σ	**Maximum stress (MPa)**	
	NACA4418	**MHKF-180**
0.5	42.60	58.11
0.8	64.51	92.51
1.0	60.12	77.48
1.2	93.73	94.47
1.5	92.69	112.88
2.0	83.17	100.03
2.3	82.92	100.59
2.5	83.35	100.23

5.4 Conclusions

In this chapter, a comparative study of structural and hydrodynamic performance of stainless-steel 3D MHKF-180 and NACA4418 cavitating hydrofoil is carried out using one-way Fluid-Structure Interaction (FSI). For this purpose, the numerical simulation is performed using ANSYS Fluent and ANSYS Static structure module. The natural frequency of both the hydrofoils is computed using Acoustic Modal Analysis for the fully wetted condition in still water. The Realizable $k - \epsilon$ turbulence model is used to solve the turbulence effect, and vapor volume fraction is calculated using the Zwart-Gerber-Belamri cavitation model.

The major findings, based on the results presented in this chapter, are given below:

(1) For different angles of attack at σ = 1, MHKF-180 predicts higher lift coefficient as compared to NACA4418 with maximum percentage difference of 29% at $\alpha = 0^o$.
(2) For different cavitation numbers at $\alpha = 8^o$, the lift coefficient value of MHKF-180 is higher than NACA4418 with maximum percentage difference of 24.6% at σ = 0.5.
(3) For $\sigma = 1$, the MHKF-180 has larger cavity length than NACA4418 hydrofoil for almost all angles of attack.
(4) The first bending natural frequency of MHKF-180 has been found to be smaller than that for NACA4418 hydrofoil. Their values for MHKF-180 was 193.77 Hz and 202 Hz for NACA4418.
(5) MHKF-180 has larger tip deformation than NACA4418 at all angles of attack. The maximum for MHKF-180 is found as 0.174 mm at $\alpha = 6^o$, and for NACA4418 it is found as 0.1325 mm at $\alpha = 12^o$.
(6) MHKF-180 has larger tip deformation than NACA4418 for both cavitating and non cavitating condition. The maximum deformation for MHKF-180 is found as 0.194 mm at σ = 2.3, and for NACA4418 it is found as 0.144 mm at σ = 1.2.
(7) For $\sigma = 1$, the maximum von Mises stress developed in MHKF-180 is 95.63 MPa at 6^o, while in NACA4418 it is 78.63 MPa at 12^o.
(8) For $\alpha = 8^o$, the maximum von Mises stress developed in MHKF-180 is 112.88 MPa at σ = 1.5, whereas in NACA4418 it is 93.73 MPa at σ = 1.2.

CHAPTER 6

CAVITATION IN SPRAY C NOZZLE USING CONVENTIONAL AND ALTERNATIVE FUEL

The flow inside the direct-injection diesel nozzles working at high injection pressures is strongly affected even by minor geometric irregularities. The irregularities can cause phenomenon such as cavitation and flow separation (Payri et al. 2016b; Tekawade et al. 2020; Maes et al. 2020). Cavitation can have a negative impact not only on the injector reliability, but also on the downstream development of the fuel spray. Therefore, there has been a concentrated effort to study the cavitation in the internal nozzle flows using computational fluid dynamics (CFD). Earlier, studied were made on the two-dimensional geometries to study the effect of corner angle and radius, hole diameter and so on (Schmidt et al. 1999). However, due to advancement in the CFD, more studies are now applied to three-dimensional geometries of realistic diesel injectors (Pastor et al. 2020)

In the present numerical work, the fuel injector selected for studying cavitation is Engine Combustion Network's (ECN) Spray C210037, which is referred as "Spray C". The ECN is an open platform for worldwide collaboration among researchers undertaking fundamental research on internal combustion engines, with a focus on close collaboration between experiments and CFD development initiatives. Spray C is a sharp-edged, diverging nozzle which is likely to cavitate. The orifice of Spray C has drilled off-center with respect to sac region. A 20 μm ridge is provided at the inlet which could lead to flow separation in the nozzle (Matusik et al. 2018). It has been observed from the literature that people have studied cavitation in Spray C using n-dodecane and commercial diesel fuel only (Payri et al. 2016a; Tekawade et al. 2020). To the best of our knowledge, no one has reported using alternative fuels like oxymethylene ether (OME_n). OME_n is a synthetic fuel, promising absorbents for carbon dioxide, and can be used as a drop-in replacement for conventional diesel fuel (Cai et al. 2020). In the present work, the comparison of cavitation characteristics of two different fuels i.e., n-dodecane and OME_3 are studied in Spray C injector nozzle using CONVERGE v3.0 code.

6.1 Governing Equations

In this a single-fluid approach, homogeneous multiphase mixture model is used, which is governed by set of governing equations for mass, momentum, and energy, with the addition of

a turbulence closure model for unsteady Reynolds-averaged Navier-Stokes (URANS) equations. The mass and momentum conservation equations are given in section 3.1 of chapter 3. Additional energy equation is given below:

$$\frac{\partial}{\partial t}(\rho_m e) + \frac{\partial}{\partial x_j}(\rho_m e u_j) = -p\frac{\partial u_j}{\partial x_j} + \tau_{ij}\frac{\partial u_i}{\partial x_j} + \frac{\partial}{\partial x_j}\left(k_{eff}\frac{\partial T}{\partial x_j}\right) + \frac{\partial}{\partial x_j}\left(\rho_m \sum_s D_{eff} h_s \frac{\partial Y_s}{\partial x_j}\right), \quad (6.1)$$

where the effective (viscous + turbulent) stress tensor is given by

$$\tau_{ij} = \frac{\partial}{\partial x_j}\left[\mu_{\text{eff}}\left(\frac{\partial u_i}{\partial x_j} + \frac{\partial u_j}{\partial x_i} - \frac{2}{3}\frac{\partial u_k}{\partial x_k}\delta_{ij}\right)\right]. \quad (6.2)$$

where e is the internal energy, Y_s represents the mass fraction of the individual species (s), h_s is the species enthalpy, k_{eff} is the sum of the molecular and turbulent conductivity, D_{eff} is the molecular and turbulent diffusion coefficient. RNG $k-\epsilon$ turbulence model is used to account for the turbulence in injector nozzle, as it is considered to be more stable and has faster convergence rate than other two-equation turbulence model for the internal flows (Yakhot et al. 1992; Givler et al. 2013; Jupudi et al. 2016; Saha et al. 2018). The equations for RNG $k-\epsilon$ model are mentioned in section 3.2.2. To define the local turbulent conductivity and diffusivity of mixture, turbulent Prandtl and Schmidt numbers are set to Pr = 0.74 and Sc = 0.71, respectively in CONVERGE v3.0. In the present study, the multiphase system is comprising of (1) a liquid phase, (b) a vapor phase, and (c) non-condensable gases. The species used are liquid fuel, vapor fuel and N_2. The subscript g will be used to present the sum of vapor and non-condensable gases. The mixture density ρ_m is expressed using below equation:

$$\rho_m = \alpha_1\rho_1 + \alpha_2\rho_2 + \alpha_3\rho_3 = \alpha_g\rho_g + (1-\alpha_g)\,\rho_{liq}, \quad (6.3)$$

Mass fraction (Y_s) and volume fraction (α_s) of the individual species are related through

$$\rho_s\alpha_s = Y_s\rho_m\,, \quad (6.4)$$

Using above two equations, the global void fraction α_g can be represented as

$$\alpha_g = \frac{Y_g/\rho_g}{\Sigma_s(Y_s/\rho_s)} = \frac{Y_g/\rho_g}{1/\rho_m}, \quad (6.5)$$

In the present implementation, instead of transporting the void fraction (α_g) directly, first the species are solved using the species transport equation and then the α_g is calculated.

$$\frac{\partial \rho_m Y_s}{\partial t} + \frac{\partial u_j \rho_m Y_s}{\partial x_j} = \frac{\partial}{\partial x_j}\left(\rho_m D_s \frac{\partial Y_s}{\partial x_j}\right) + S_s, \tag{6.6}$$

where S_s is the source or sink term associated with the mass transfer due to phase change, and D_s is the diffusivity coefficient of each component in the mixture. The non-condensable gas (N_2) does not have the source or sink term. The S_s is estimated using Homogeneous Relaxation Model (HRM) which is described in next section.

The ideal gas equation is used to calculate the densities of all the gaseous species:

$$\rho_s = \frac{p}{R_s T}, \tag{6.7}$$

where R_s is the gas constant and T is the temperature. The liquid can be considered either incompressible or compressible. In this work, it is considered compressible.

6.1.1 Cavitation Model (Homogeneous Relaxation Model)

In earlier chapters for cavitation on hydrofoils, bubble-dynamics based cavitation model i.e., Zwart-Gerber-Belamri model was used because the thermal effects on hydrofoils were neglected. However, for nozzle cavitation, energy equation is being solved, and therefore bubble-dynamics based cavitation model might not be a suitable choice since thermal effects are essential to consider in the nozzle cavitation. Therefore, in the present work for cavitation in injector nozzle, the mass exchange between the liquid and vapor is based on the homogeneous relaxation model (HRM) developed by Bilicki and Kestin (1990). This model is capable of capturing the essence of non-equilibrium phase change. Cavitation is the pressure-driven vaporization phenomenon which takes place at low temperatures in which the density of vapor is so small that latent heat flow does not affect the overall phenomenon. This results in much faster time scale of heat transfer than the time scale of bulk motion. Therefore, the bulk motion is mainly controlled by the inertia of liquid. The HRM assumes a simple first-order rate equation for the evolution of instantaneous vapor quality *x* towards the equilibrium vapor quality $\bar{x}$ over a given time scale θ.

The instantaneous non equilibrium quality of vapor (x) is calculated as

$$x = \frac{m_{vap}}{m_{vap} + m_{liq}}, \tag{6.8}$$

The HRM evaluates the source term S_s in the fuel species conservation equation. The S_s is estimated using rate of change of local vapor quality (Dx/Dt). The term Dx/Dt is expressed in HRM model with the help of time scale θ as:

$$\frac{Dx}{Dt} = \frac{\bar{x}-x}{\theta}, \tag{6.9}$$

The equilibrium vapor quality $\bar{x}$ is a function of thermodynamic properties at local pressure i.e., $\bar{x}$ (p, h) which is defined by the equation with bounds at zero and unity :

$$\bar{x} = \frac{h-h_{l,sat}}{h_{v,sat}-h_{l,sat}}, \tag{6.10}$$

In the above equation h is the actual enthalpy of liquid and vapor, excluding air content, and subscript l, sat and v, sat refers to saturated liquid and vapor, respectively. The time scale θ is calculated using the empirical fit given by Downar-Zapolski et al. (1996).

$$\theta = \theta_0 \alpha^{-0.54} \psi^{-1.76} \quad [\text{s}], \tag{6.11}$$

where $\theta_0 = 3.84 \times 10^{-7}$; $\psi = \frac{|p_{sat}-p|}{P_{crit}-p_{sat}}$; $\alpha = \alpha_v + \alpha_{N_2,}$

These specific values of parameters are known to be effective for flow problems with injection pressure higher than 10 bar (Downar-Zapolski et al. 1996; Neroorkar et al. 2012). HRM is capable of predicting the phase change from liquid to vapor and vice versa, whenever the thermodynamic condition is feasible. Non-condensable gases are included in α, despite the fact that gases were not considered in the initial HRM formulation. In a given cell, when liquid volume fraction is very low as compared to gaseous species, then just considering the fuel vapor volume fraction may not provide the physical thermodynamic condition in that particular cell. Furthermore, Downar-Zapolski et al. (1996) pointed that the relaxation time decreases exponentially to very small values with the increase in void fraction. There is asymptotic decrease in the relaxation time scale when void fraction exceed 10% (Saha et al. 2017). This implies that the addition of gases in the void fraction should not affect the prediction of the relaxation time scale theoretically. To understand the relations between S_s and $(Dx)/(Dt)$, Battistoni et al. (2015) explained the effect of non-condensable gases on the cavitation. If instantaneous vapor quality of a computational cell is represented by x^0, and x^1 is corresponding value for the following time step, with the time-step size of Δt, then $x^1 = \bar{x} - (\bar{x} - x^0)e^{-\Delta t/\theta}$. Hence,

$$S_s = \frac{(x^1 - x^0)(m_{vap} + m_{liq})}{V\Delta t} = (x^1 - x^0)\rho \frac{(Y_v + Y_l)}{\Delta t}, \quad (6.12)$$

where V represents the volume of computation cell and m_{liq} and m_{vap} are the mass of the liquid and vapor phases in the computational, respectively.

6.2 Geometry and Meshing

Spray C is a single orifice diverging nozzle with a nominal hole diameter of 200 μm. It is manufactured with a sharp inlet corner to produce cavitation and has 5% hydro erosion to maintain flow rate consistency in the injector (Westlye et al. 2016). The three-dimensional part image of Spray C and section of injector nozzle hole using x-ray tomography is shown in Fig. 6.1 (Tekawade et al. 2020). The simulation is performed using the CONVERGE v3.0 code, in which mesh is generated automatically during run time. A truncated cone-shaped fixed embedding is used near the hole to improve the accuracy around the zone of interest as shown in Fig .6.2. Five level of embedding is used, according to which the smallest cell has a dimension 2^5 = 32 times smaller than the base/maximum grid size in the domain (Saha et al. 2017). For grid independence test three different base grid size is used i.e., coarse grid (1000 μm), medium grid (500 μm), and fine grid (250 μm). Considering the computational cost and cavitation capturing ability, the medium grid is found to be grid independent. A vertical cut plane showing the mesh with a base grid size of 500 μm and a minimum cell size of 15.625 μm is shown in Fig.6.3. There were around 1.3 million cells in the domain. The results for the grid independence test is given in the results and discussion section.

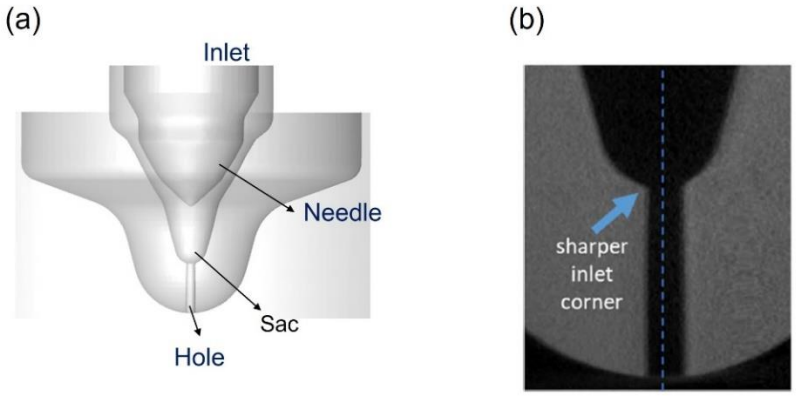

Fig. 6.1. Surface rendering of X-ray tomography of ECN (a) Spray C injector nozzle and (b) asymmetrical sharp corner hole of Spray C.

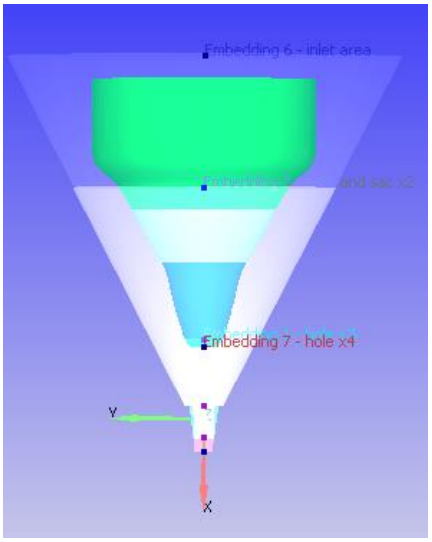

Fig. 6.2. Cylindrical embedding in single hole Spray C nozzle.

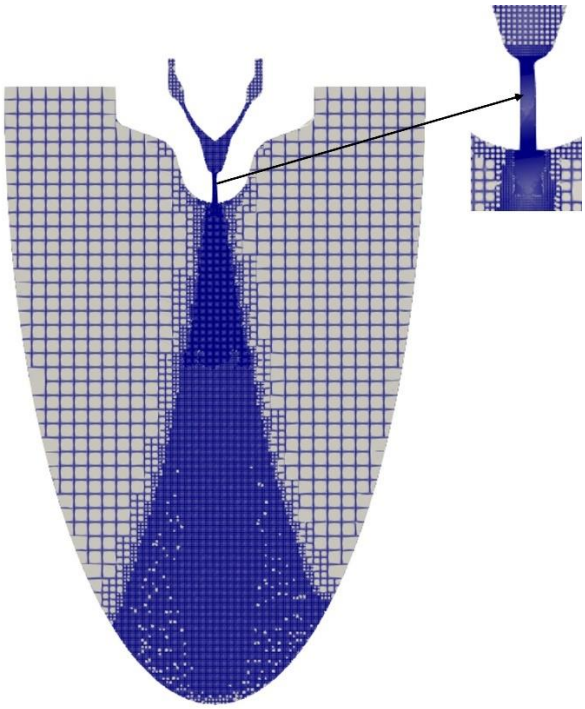

Fig. 6.3. Vertical cut-plane showing the mesh with 15.625 μm as minimum grid size and 500 μm base grid size.

6.3 Boundary Conditions

The inlet and outlet of the nozzle are provided with pressure values for both the fuel cases. The fuel properties for n-dodecane and OME_3 are mentioned in the Table 6.1. The inlet pressure or injection pressure is 150 MPa and outlet pressure is 2 MPa, the walls are kept as the no-slip condition. Turbulent kinetic energy and turbulence dissipation rate is provided at the inlet and outlet. The standard law-of-wall for turbulence is used to model the boundary layer. The transient simulation is run until both the inflow and outflow mass flow rates are stabilized. In

the liquid fuel very small mass fraction of non-condensable gas (N_2 = 10^{-6} mass fraction) is used as a nucleation site for cavitation initiation. The governing equation is solved using finite volume method in the CONVERGE v3.0 code. The Rhie-Chow algorithm has been used to collocate all the transport variables at the cell center. Pressure implicit with the splitting operator (PISO) algorithm is used for the pressure-velocity coupling. Successive Over-Relaxation (SOR) algorithm has been used for better numerical stability. RNG $\kappa - \epsilon$ turbulence model is used for solving the turbulence effect inside nozzle, and phase change is captured using homogenous relaxation model (HRM). Table 6.2 shows the operating parameters used for Spray C.

Table 6.1. Properties of n-Dodecane and OME_3 fuels at a temperature of 303 K

Properties	**n-dodecane**	**OME_3**
Density (kg/m^3)	742	1032
Viscosity (N.s/m^2)	0.001285	0.001
Surface Tension (N/m)	0.0245	0.0257
Vapor Pressure (Pa)	28.47	581.50
Specific Heat (J/kg K)	2222	3455

Table 6.2. Operating parameters for Spray C

Operating parameters	**Spray C**
Inlet Pressure (MPa)	150
Chamber Pressure (MPa)	2
Chamber Temperature (K)	303
Fuel Temperature (K)	338
Chamber Fluid	N_2

6.4 Results and Discussion

The results obtained from the numerical simulation using n-dodecane and OME_3 fuel in Spray C are discussed in this section for three different cases. First case is using n-dodecane fuel is Spray C for grid independence test and validation with the experimental results. Second case is using OME_3 fuel in the nozzle and comparing the cavitation characteristics with the n-dodecane. In third case the saturation pressure of n-dodecane is replaced with the saturation pressure of OME_3 and results are compared with the first case.

6.4.1 Grid Independence Test and Validation

For grid independence test, the comparison is made using n-dodecane fuel in Spray C injector nozzle. Three different grids have been examined using different base grid size or maximum cell size. The base grid size for coarse grid (0.18 million cells) is 1000 μm, for medium grid (1.3 million cells) is 500 μm, and fine grid (7.8 million cells) it is 250 μm. Accordingly, the minimum cell size for coarse grid, medium grid, and fine grid are 31.25 μm, 15.625 μm, and 7.8125 μm, respectively. The mass fraction contours using three different grids is presented in Fig.6.6. From mass fraction contour it is observed that coarse grid is unable to capture the flow separation along the nozzle wall and hence shows minimum cavitation, whereas medium grid and fine grid are showing presence of cavitation on the side wall of Spray C similar to the experimental results in the literature (Tekawade et al. 2020). Similarly, the mass flow rate along the flow time is plotted with respect to different grids in Fig. 6.5. The mass flow rate for the coarse grid is around 9.95 mg/ms, for medium grid it is 9.80 mg/ms, and for fine grid it is 9.90 mg/ms. On comparing the computational cost associated and the results computed using fine grid with 7.8 million cells and the medium grid having 1.3 million cells, it can be concluded that medium grid can be used for further simulations as it is computationally optimum and giving closer results to experimental data in the literature. The experimental value provided for the mass flow rate of n-dodecane in the literature is 10.06 mg/ms (Payri et al. 2016a), giving percentage difference of around 2.58% for the medium grid with mass flow rate of 9.80 mg/ms. Therefore, medium grid with base grid size 500 μm is considered as grid independent mesh.

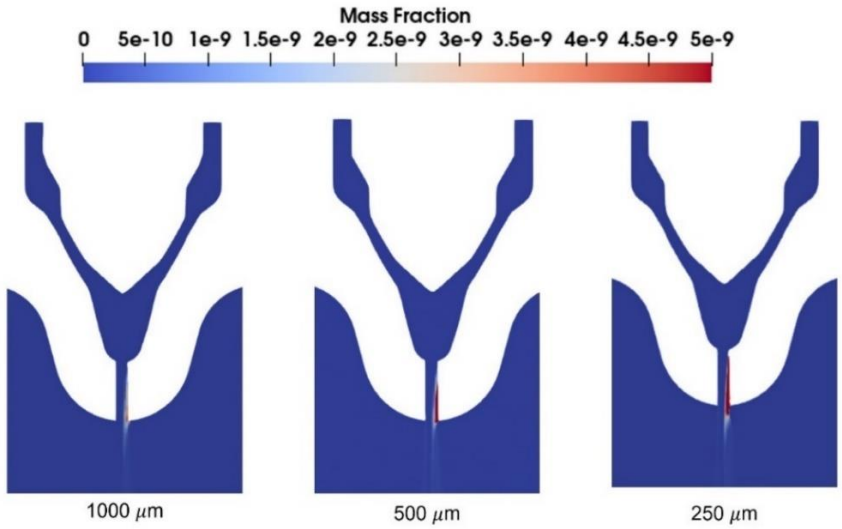

Fig. 6.4. Comparison of vapor mass fraction contours using different grid size for grid independence test in Spray C.

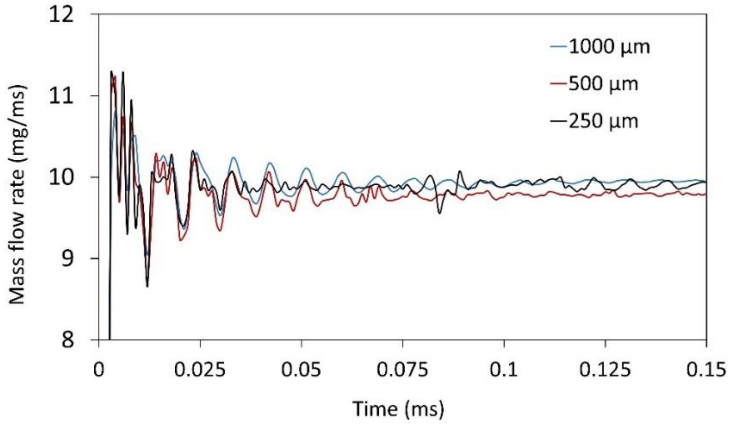

Fig. 6.5. Mass flow rate predictions for grid independence test in case of Spray C.

Fig. 6.6 presents the direct comparsion between the experimental results in the literature (Tekawade et al. 2020) and void fraction contours from the CFD data for medium grid in Spray C using n-dodecane fuel. The void fraction contour shows that cavitation begins at the sharp inlet corner of the nozzle and extends to the nozzle's exit. Most of the nozzle cross-section is filled with a liquid phase enclosed with a thin layer of vapor near the wall. The presence of vapor cavity shows the flow separation at the sharp corner of Spray C, which is predicted well using simulation. Both the expeirmental imaging techinique and simulated result predict cavitation extending to the nozzle exit. Clearly, from the void fraction contour and mass flow rate comparison it is observed that the numerical results are in good agreement with the experimental data. Next, the comparison of results obtained through simulation for n-dodecane and OME_3 is presented.

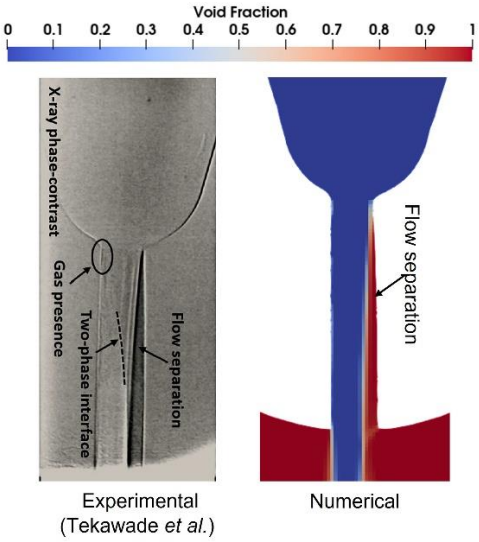

Fig. 6.6. Comparison between intensity map from X-ray tomography experiments Tekawade et al. 2020) with void fraction contour from simulation for n-dodecane.

Fig. 6.7 compares the mass flow rate of n-dodecane and OME_3 fuels from the nozzle exit to the chamber. Initially, there is fluctuation in the mass flow rate value till 0.05 ms due to pressure oscillations in the sac region, and later the mass flow rates become almost constant. The stabilized mass flow rate of n-dodecane fuel is 9.8 mg/ms, which is consistent with the literature as discussed earlier, whereas the mass flow rate for OME_3 is 11.55 mg/ms. The OME_3 mass rate is 1.178 times that of n-dodecane. The mass flow rate can also be computed theoretically using the Bernoulli's equation on the basis of the reference density for OME_3 (ρ_1= 996.312 kg/m^3) and n-dodecane (ρ_2= 716.41 kg/m^3). The change in Bernoulli's velocity can be calculated as:

$$\frac{1}{2}\rho_1 U_1^2 = \frac{1}{2}\rho_2 U_2^2 \tag{6.13}$$

$$\frac{U_2}{U_1} = \sqrt{\frac{\rho_1}{\rho_2}} = \sqrt{1.4} = 1.183.$$

Mass flow rate is defined as:

$$\dot{m} = \rho U A \tag{6.14}$$

$$\text{which gives } \frac{\dot{m}_1}{\dot{m}_2} = 1.17.$$

which is giving closer approximation to the numerically simulated values.

The higher density and lower viscosity of OME_3 fuel results in higher mass flow rate of OME_3 as compared to n-dodecane. It will be more meaningful to compare the mass fraction profiles of n-dodecane and OME_3 fuels inside the nozzle to understand how the cavity is forming using these two fuels. Therefore, Fig. 6.8 compares the mass fraction contour of vapor for n-dodecane and OME_3 fuel. It is evident from the contour that the mass fraction of OME_3 is higher than the n-dodecane at the asymmetric wall of the hole resulting in more cavitation than n-dodecane.

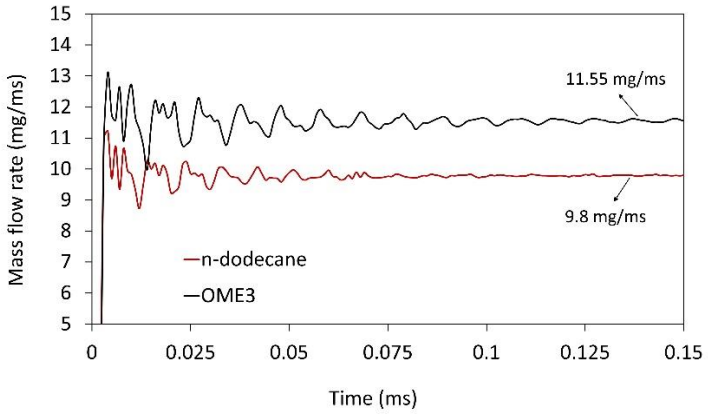

Fig. 6.7. Comparison of mass flow rate predictions through Spray C nozzle for n-dodecane and OME_3.

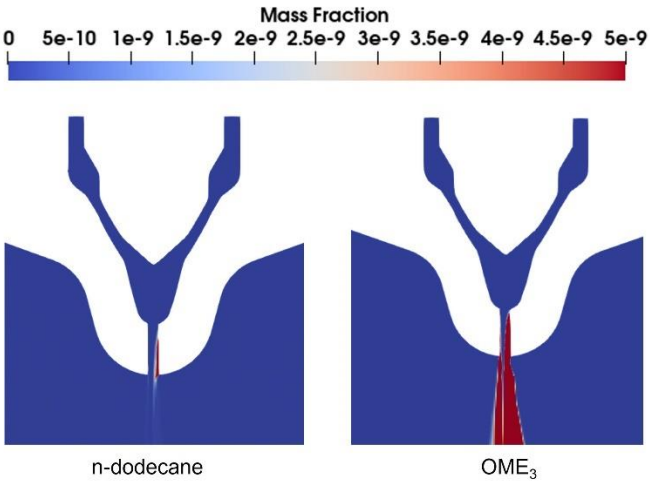

Fig. 6.8. Comparison of vapor mass fraction contours on a vertical cut-plane passing through the mid-section of the Spray C nozzle for n-dodecane and OME_3.

Next, in Fig. 6.9, the density contour of both fuels is presented. The center of the nozzle is filled with the higher density liquid fuel, whereas the wall is covered with the low-density gas, which can be seen in the contour. For OME_3, the density at the inlet of nozzle is around 1000 kg/m^3 whereas for dodecane it is around 700 kg/m^3. This difference is mainly due to the

difference in the properties of both the fuel as mentioned in table 6.1. In, Fig. 6.10 the mass fraction contour comparison for third case is presented, in which the saturation pressure of n-dodecane is replaced with the OME_3 saturation pressure. The vapor pressure of OME_3 at 303 K is 581.50 Pa, whereas for n-dodecane it is 28.47 Pa. Therefore, due to higher vapor pressure of OME_3, more cavitation can be seen for this case also. For third case there is no change in mass flow rate or density is observed with respect to n-dodecane case.

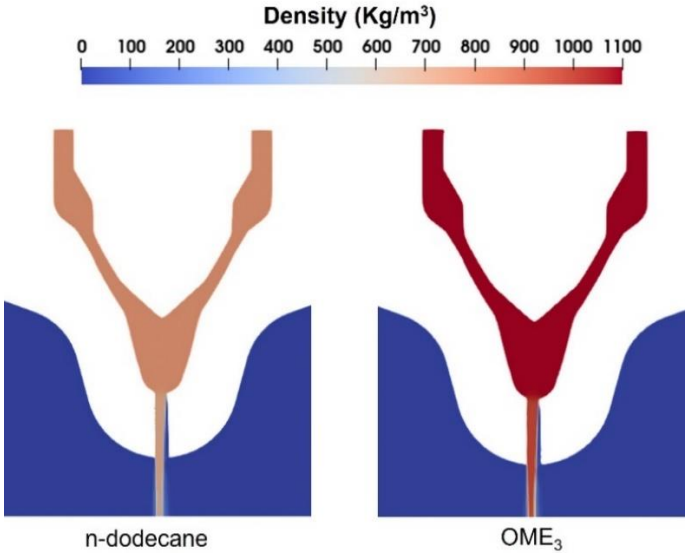

Fig. 6.9. Density variation for n-dodecane and OME_3.

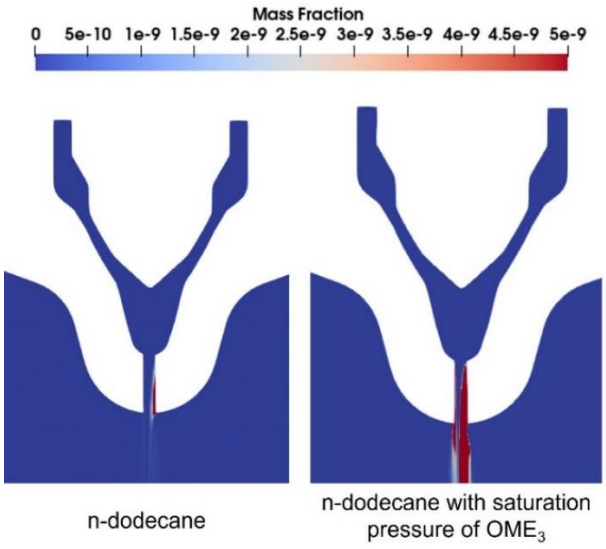

Fig. 6.10. Mass fraction contour for n-dodecane and saturation pressure of n-dodecane replaced with OME_3 saturation pressure.

6.5 Conclusions

This chapter provides the insight about the cavitation characteristic of n-dodecane and oxymethylene ether fuel (OME_3) in cavitating Spray C injector nozzle using commercial CONVERGE v3.0 code. The Homogeneous Relaxation Model (HRM) coupled with the multiphase mixture model is used for cavitation modeling, and RNG $\kappa - \epsilon$ is used to model the turbulence effect. The void fraction contour and the mass flow rate of n-dodecane fuel are compared with the experimental results provided in the literature. The mass flow rate, and contours of mass fraction and density are presented for OME_3 and n-dodecane fuels comparison. The findings are:

(1) The mass flow rate of n-dodecane fuel was found to be in good agreement with the experimental data with a percentage difference of 3%.
(2) The simulations predict the flow separation at the sharp asymmetric corner of the nozzle similar to experimental work. The flow separation at the corner initiates the cavitation along the wall to the nozzle exit.
(3) The mass flow rate obtained for n-dodecane is 9.8 mg/ms and for OME_3 is 11.55 mg/ms. The mass flow rate difference is mainly attributed to higher density of OME_3 fuel.
(4) The OME_3 fuel produced more cavity than n-dodecane fuel in the Spray C nozzle due to higher saturation pressure of OME_3 as compared to n-dodecane.

CHAPTER 7

CONCLUSIONS

Cavitation occurs in flow regions where the hydrodynamic effect reduces the local pressure below the saturation vapor pressure of the liquid, causing the formation of vapor bubbles. When these vapor bubbles enter the region of higher pressure, they collapse violently producing enough force to damage the solid body. In case of hydrofoils, cavitation can affect the hydrodynamic and structural performance potentially. In injector nozzles, cavitation can cause a fuel injection instability and decreased fuel efficiency. This thesis is a compilation of three studies motivated by the cavitation phenomenon on hydrofoils and in injector nozzle. The goal of the three studies are:

1) Assessment of cavitation and turbulence models on cavitating hydrofoils.
2) Study of the hydrodynamic and structural performance of 3D MHKF-180 and NACA4418 under cavitation using Fluid-Structure Interaction (FSI).
3) Study of the cavitation in Spray C injector nozzle using conventional and alternative fuel.

The major conclusions from these three studies are presented below:

7.1 Assessment of Cavitation and Turbulence Models on Cavitating Hydrofoils

In this part of thesis, the systematic investigation of two different cavitation models i.e., Schnerr -Sauer (SS) and Zwart-Gerber-Belamri (ZGB) and four of four different turbulence models i.e., Standard $k-\epsilon$, RNG $k-\epsilon$, Realizable $k-\epsilon$, and SST $k-\omega$ is studied on cavitating 3D NACA4412 and Clark-y hydrofoil. The performance is computed in terms of lift coefficient, drag coefficient, lift-to-drag ratio, and velocity profiles.

The major findings, based on the above investigation are:

(1) On comparing the performance of SS and ZGB cavitation model on cavitating NACA4412 hydrofoil, both models were found to give similar performance. However, ZGB is used for further numerical simulations on cavitating hydrofoils due to its robustness and accuracy.
(2) On comparing performance of different turbulence models on cavitating NACA4412 and Clark-y hydrofoil, Realizable $k-\epsilon$ was found to be more accurate than other two equations models.

Further using Realizable $k-\epsilon$ turbulence model and Zwart-Gerber-Belamri cavitation model the performance of cavitating MHKF-180s hydrofoil is computed at different angle of attack for Reynolds number ranging from 1.1 X 10^6 – 2.6 X 10^6 at σ =1. Also, comparative study of hydrodynamic performance of 3D cavitating and non-cavitating MHKF-180s hydrofoil is carried out for α varying from -5^o to +12^o at Re =1.3 million. The finding for above analysis are given below:

(3) The hydrodynamic performance of cavitating 3D MHKF-180s hydrofoil at different angles of attack and σ = 1, found to be independent of Reynolds number.

(4) For σ =1, the MHKF-180s has maximum cavity at an angle of attack 12^o at all Reynolds number.

(5) On comparing the hydrodynamic performance of non-cavitating and cavitating (σ =1) MHKF-180s hydrofoil at different angle of attack (α = -5^o, 0^o, 5^o, 7^o, 10^o, and 12^o) at Re = 1.3 X 10^6, it was found that:

   (i) There is no cavitation on MHKF-180s hydrofoil at α = -5^o and 0^o for σ =1.

   (ii) Lift coefficient for cavitating case is reduced as compared to non-cavitating condition with maximum reduction of 40.5% at α = 10^o.

   (iii) The drag coefficient for cavitating cases is higher at almost all angles of attack when compared to non-cavitating conditions due to increase in pressure drag. The maximum increment in C_d value is obtained at α =12^o which is almost seven times of non-cavitating C_d.

   (iv) Lift-to-drag ratio for cavitating condition is found to be lower than non-cavitating condition. The maximum reduction is observed at α =12^o, due to maximum cavity.

   (v) For cavitating condition, the skin friction coefficient (C_f) is found to be lower due to presence of cavity on the upper surface of hydrofoil.

   (vi) At α = 12^o, the x-component velocity on vertical lines of hydrofoil upper surface was found to be lower at σ =1, with much earlier flow separation along the chord.

   (vii) At α = 12^o, the maximum turbulent kinetic energy present at the wake of cavitating hydrofoil was much higher (25 m^2/s^2) than non-cavitating hydrofoil (4m^2/s^2).

In the last part of the first objective, the hydrodynamic performance of MHKF-180s is compared with MHKF-180 at different angles of attack and σ =1. The negligible change is observed in the performance of two foils and therefore, in the second objective of the thesis the hydrodynamic and structural performance of 3D MHKF-180 hydrofoil is compared with NACA4418 at different angles of attack and at different cavitation numbers using FSI.

7.2 Study of the Hydrodynamic and Structural Performance of 3D MHKF-180 and NACA4418 under Cavitation using Fluid-Structure Interaction (FSI)

In this study, a comparative study of structural and hydrodynamic performance of stainless-steel 3D MHKF-180 and NACA4418 cavitating hydrofoil is carried out using one-way Fluid-Structure Interaction (FSI). For this purpose, the numerical simulation is performed using ANSYS Fluent and ANSYS Static structure module. The natural frequency of both the hydrofoils is computed using Acoustic Modal Analysis for the fully wetted condition in still water. The Realizable $k-\epsilon$ turbulence model is used to solve the turbulence effect, and vapor volume fraction is calculated using the Zwart-Gerber-Belamri cavitation model.

The findings, based on the results, are given below:

(1) For different angles of attack at σ = 1, MHKF-180 predicts higher lift coefficient as compared to NACA4418 with maximum percentage difference of 29% at $\alpha = 0^{o}$.
(2) For different cavitation numbers at $\alpha = 8^{o}$, the lift coefficient value of MHKF-180 is higher than NACA4418 with maximum percentage difference of 24.6% at σ = 0.5.
(3) For $\sigma = 1$, the MHKF-180 has larger cavity length than NACA4418 hydrofoil for almost all angles of attack.
(4) The first bending natural frequency of MHKF-180 has been found to be smaller than that for NACA4418 hydrofoil. Their values for MHKF-180 was 193.77 Hz and 202 Hz for NACA4418.
(5) MHKF-180 has larger tip deformation than NACA4418 at all angles of attack. The maximum for MHKF-180 is found as 0.174 mm at $\alpha = 6^{o}$, and for NACA4418 it is found as 0.1325 mm at $\alpha = 12^{o}$.
(6) MHKF-180 has larger tip deformation than NACA4418 for both cavitating and non cavitating condition. The maximum deformation for MHKF-180 is found as 0.194 mm at σ = 2.3, and for NACA4418 it is found as 0.144 mm at σ = 1.2.
(7) For $\sigma = 1$, the maximum von Mises stress developed in MHKF-180 is 95.63 MPa at 6^{o}, while in NACA4418 it is 78.63 MPa at 12^{o}.
(8) For $\alpha = 8^{o}$, the maximum von Mises stress developed in MHKF-180 is 112.88 MPa at σ = 1.5, whereas in NACA4418 it is 93.73 MPa at σ = 1.2.

7.3 Study of the Cavitation in Spray C Injector Nozzle using Conventional and Alternative Fuel

In this study, the cavitation characteristic of conventional n-dodecane fuel is compared with synthetic fuel i.e., oxymethylene ether fuel (OME_3) in cavitating Spray C injector nozzle using commercial CONVERGE v3.0 code. The Homogeneous Relaxation Model (HRM) coupled with the multiphase mixture model is used for cavitation modeling, and RNG $\kappa - \epsilon$ is used to model the turbulence effect. The void fraction contour and the mass flow rate of n-dodecane fuel are compared with the experimental results provided in the literature. The mass flow rate, and contours of mass fraction and density are presented for OME_3 and n-dodecane fuels comparison. The findings are:

(1) The mass flow rate of n-dodecane fuel was found to be in good agreement with the experimental data with a percentage difference of 3%.
(2) The simulations predict the flow separation at the sharp asymmetric corner of the nozzle similar to experimental work. The flow separation at the corner initiates the cavitation along the wall to the nozzle exit.
(3) The mass flow rate obtained for n-dodecane is 9.8 mg/ms and for OME_3 is 11.55 mg/ms. The mass flow rate difference is mainly attributed to higher density of OME_3 fuel.
(4) The OME_3 fuel produced more cavity than n-dodecane fuel in the Spray C nozzle due to higher saturation pressure of OME_3 as compared to n-dodecane.

7.4 Scope for Further Study

The present work has given scope for future studies in the following areas:

(1) Large Eddy Simulation (LES) or Detached Eddy Simulation (DES) turbulence models should be tested to further investigate the role of turbulence models in cavitation on hydrofoils and injector nozzles.
(2) Volume of fluid (VOF) method can be used for the cavitating flow on hydrofoils.
(3) Two-way fluid structure interaction (FSI) study can be used on rigid and flexible cavitating hydrofoils.
(4) Attempts should be made using numerical simulations to understand the failures of hydrofoils caused due to cavitation.
(5) In spray C the effect of cavitation can be studied on the spray formation along with combustion and emission model using OME_3 and other synthetic fuels.

LIST OF PUBLICATIONS

Journals

1. **Singh, S.,** Danish, M., & Saha, K. (2021). Numerical simulation of unsteady cavitating flow around 2-D MHKF-180 and NACA4418 hydrofoils. *Journal of Ocean Engineering and Marine Energy*, 7, 243-259. [IF: 1.9]. https://doi.org/10.1007/s40722-021-00200-3
2. **Singh, S.,** Danish, M., Saha, K., & Singh, B. N. (2023). Numerical simulation and analysis of fluid-structure interaction on 3D MHKF-180 and NACA4418 cavitating hydrofoils. *Ocean Engineering*, 272, 113867. [IF: 5.0]. https://doi.org/10.1016/j.oceaneng.2023.113867
3. **Singh, S.,** Sachdeva, A., Danish, M., & Saha, K. (2023). Assessment of Unsteady Cavitating and Non-Cavitating Flows on 3D Marine Hydrokinetic Foil (MHKF-180s). *Renewable Energy* (under review).

Conferences

1. **Singh, S.,** Danish, M., Saha, K., & Ranjan, V. (2018). Numerical simulation of Vortex-shedding from NACA4418 hydrofoil. *Vibroengineering Procedia*, 21, 125-130. https://doi.org/10.21595/vp.2018.20396
2. **Singh, S.,** Danish, M., & Saha, K. (2019). Computational investigation of cavitating flow around two dimensional NACA 4424 and MHKF-240 hydrofoil. *Vibroengineering Procedia*, 29, 159-164. https://doi.org/10.21595/vp.2019.21121

Book Chapter

1. **Singh, S.,** Ailaboina, A., Battistoni, M., Danish, M., & Saha, K. (2023). Numerical Investigation of Cavitation Behaviour for Dodecane and OME3 Fuel in ECN Spray C Injector Nozzle. Lect. Notes in Mechanical Engineering, Sudev Das et al. (Eds), Springer Nature, ISBN: 978-981-99-5989-1.

Publications (Other than Ph.D. work)

1. Kumar. P., **Singh, S.,** & Reddy, S. R. (2022). Assessment of unsteady cavitating flow around modified NACA4412 hydrofoil. *Ocean Engineering*, 266, 113039. [IF: 5.0]. https://doi.org/10.1016/j.oceaneng.2022.113039

2. Sachdeva, A., **Singh, S.,** & Danish, M. (2023). Fluid flow analysis of unsteady cavitating flow over MHKF-180s hydrofoil. *Materials Today: Proceedings*. https://doi.org/10.1016/j.matpr.2023.08.337
3. Kumar, P., **Singh, S.,** & Reddy, R. (2023). Computational investigation of cavitating flow on 3D NACA4412 hydrofoil with arc dimple. *Materials Today: Proceedings.* https://doi.org/10.1016/j.matpr.2023.08.256
4. Kumar, A., **Singh, S.,** & Bhalla, N. A. (2019). Effect of slant angle variation on the drag force for Ahmed body car model. *Vibroengineering Procedia*, 29, 153-158. https://doi.org/10.21595/vp.2019.21115
5. Kumar, P., **Singh, S.,** & Reddy, R. (2022). Computational Study of Unsteady Cavitating Flow on 3D NACA4412 Hydrofoil. 9 th International and 49th National Conference on Fluid Mechanics and Fluid Power (FMFP), IIT Roorkee.
6. Deshpande, S. S., Danish, M., & **Singh, S.(**2022). Numerical Simulation and Analysis of Power-law Fluid Flow in a Four-sided Lid-driven Cavity. International Conference in Recent Advances in Mechanical Engineering (ICRAM2022), IIT Jodhpur. ISBN: 978-93- 91355-76-0 (e-Book).
7. Kumar, P., **Singh, S.,** & Reddy, R.(2022). Numerical Investigation of Unsteady Cavitating Flow on NACA4412 Hydrofoil. The 1st International Conference in Fluid, Thermal and Energy Systems (ICFTES'22), NIT Calicut.
8. Sachdeva, A., **Singh, S.,** Danish, M., & Reddy, M.S. (2023). Numerical Investigation of Cavitating Base MHKF-180s and Modified MHKF-180s Hydrofoil. The 2nd Biennial International Symposium on Fluids and Thermal Engineering (FLUTE 2023), Amity University.
9. Saeedrashed, Y., Sachdeva, A., **Singh, S.,** & Benim, A. C. (2023). Numerical Simulation of Cavitation Characteristics on Stepped Spillway Due to Different Geometry Configuration. 14th International Conference on Computational Heat and Mass Transfer ICCHMT 2023, Düsseldorf, Germany.
10. Reddy, M.S., Sachdeva, A., **Singh, S.,** & Danish, M. (2023). Transonic Shock Boundary Layer Interaction over SHM-1 and Modified SHM-1 Airfoil. 10th International and 50th National Conference on Fluid Mechanics and Fluid Power (FMFP), IIT Jodhpur, India (accepted).

REFERENCES

Ahn, S. H., Xiao, Y., Wang, Z., Luo, Y., & Fan, H. (2018). Unsteady prediction of cavitating flow around a three-dimensional hydrofoil by using a modified RNG k-ε model. Ocean Engineering, 158, 275-285.

Akcabay, D. T., Chae, E. J., Young, Y. L., Ducoin, A., & Astolfi, J. A. (2014). Cavity induced vibration of flexible hydrofoils. Journal of Fluids and Structures, 49, 463-484.

Akcabay, D. T., & Young, Y. L. (2014). Influence of cavitation on the hydroelastic stability of hydrofoils. Journal of Fluids and Structures, 49, 170-185.

Anderson, J. (2011). EBOOK: Fundamentals of Aerodynamics. Tata McGraw Hill Education.

Andriotis, A., Gavaises, M., & Arcoumanis, C. (2008). Vortex flow and cavitation in diesel injector nozzles. Journal of Fluid Mechanics, 610, 195-215.

Arcoumanis, C., Flora, H., Gavaises, M., Kampanis, N., & Horrocks, R. (1999). Investigation of cavitation in a vertical multi-hole injector. SAE transactions, 661-678.

Arcoumanis, C., Flora, H., Gavaises, M., & Badami, M. (2000). Cavitation in real-size multi-hole diesel injector nozzles. SAE transactions, 1485-1500.

Ausoni, P., Farhat, M., Escaler, X., Egusquiza, E., & Avellan, F. (2007). Cavitation influence on von Kármán vortex shedding and induced hydrofoil vibrations. Journal of Fluid Engineering, 129(8), 966-973.

Battistoni, M., Duke, D., Swantek, A. B., Tilocco, F. Z., Powell, C. F., & Som, S. (2015). Effects of noncondensable gas on cavitating nozzles. Atomization and Sprays, 25(6).

Battistoni, M., Som, S., & Longman, D. E. (2014). Comparison of mixture and multifluid models for in-nozzle cavitation prediction. Journal of Engineering for Gas Turbines and Power, 136(6), 061506.

Benaouicha, M., Guillou, S., Santa Cruz, A., & Trigui, H. (2018). Fluid-structure interaction approach for numerical investigation of a flexible hydrofoil deformations in turbulent fluid flow. In Pressure Vessels and Piping Conference (Vol. 51654, p. V004T04A011). American Society of Mechanical Engineers.

Bensow, R. E. (2011). Simulation of the unsteady cavitation on the Delft Twist11 foil using RANS, DES, and LES. In Second international symposium on marine propulsors.

Bilicki, Z., & Kestin, J. (1990). Physical aspects of the relaxation model in two-phase flow. Proceedings of the Royal Society of London. A. Mathematical and Physical Sciences, 428(1875), 379-397.

Billet, M. L., & Holl, J. W. (1981). Scale effects on various types of limited cavitation. Journal of Fluid Engineering, 103(3), 405-414.

Blake, W. K., & Maga, L. J. (1975). On the flow− excited vibrations of cantilever struts in water. I. Flow− induced damping and vibration. The Journal of the Acoustical Society of America, 57(3), 610-625.

Brandner, P. A., & Pearce, B. W. (2012). Experimental modelling of steady hydrofoil fluid-structure interaction. Proceedings of the 18th Australasian Fluid Mechanics Conference, 3-7.

Brennen, C. E. (2005). Fundamentals of multiphase flow. Cambridge university press.

Brennen, C. E. (2014). Cavitation and bubble dynamics. Cambridge university press.

Britannica. (2023). https://www.britannica.com/technology/naval-architecture/Cavitation.

Cai, L., Jacobs, S., Langer, R., vom Lehn, F., Heufer, K. A., & Pitsch, H. (2020). Auto-ignition of oxymethylene ethers (OMEn, n= 2–4) as promising synthetic e-fuels from renewable electricity: shock tube experiments and automatic mechanism generation. Fuel, 264, 116711.

Cao, W., Xu, H., Ren, H., & Wang, C. (2015). Numerical study on characteristics of 3D cavitating hydrofoil. In MATEC Web of Conferences (Vol. 25, p. 03002). EDP Sciences.

Capurso, T., Lopez, M., Lorusso, M., Torresi, M., Pascazio, G., Camporeale, S. M., & Fortunato, B. (2017). Numerical investigation of cavitation on a NACA0015 hydrofoil by means of OpenFOAM. Energy Procedia, 126, 794-801.

Carrat, J. B., Fortes-Patella, R., & Franc, J. P. (2017). Assessment of cavitating flow aggressiveness on a hydrofoil: Experimental and numerical approaches. In Fluids Engineering Division Summer Meeting (Vol. 58042, p. V01AT05A013). American Society of Mechanical Engineers.

Celik, I. B., Ghia, U., Roache, P. J., & Freitas, C. J. (2008). Procedure for estimation and reporting of uncertainty due to discretization in CFD applications. Journal of Fluids Engineering-Transactions of the ASME, 130(7).

Chaves, H., Knapp, M., Kubitzek, A., Obermeier, F., & Schneider, T. (1995). Experimental study of cavitation in the nozzle hole of diesel injectors using transparent nozzles. SAE transactions, 645-657.

Chebli, R., Audebert, B., Zhang, G., & Coutier-Delgosha, O. (2021). Influence of the turbulence modeling on the simulation of unsteady cavitating flows. Computers & Fluids, 221, 104898.

Chen, Y., & Heister, S. D. (1995). Two-phase modeling of cavitated flows. Computers & Fluids, 24(7), 799-809.

Čupr, P., Štefan, D., Habán, V., & Rudolf, P. (2019). FSI analysis of francis-99 hydrofoil employing SBES model to adequately predict vortex shedding. In Journal of Physics: Conference Series (Vol. 1296, No. 1, p. 012002). IOP Publishing.

Dabiri, S., Sirignano, W. A., & Joseph, D. D. (2007). Cavitation in an orifice flow. Physics of Fluids, 19(7).

Darandale, G. R., M. V. Jadhav, A. R. Warade, and Vikas S. Hakke. "Hydrodynamic cavitation a novel approach in wastewater treatment: A review." *Materials Today: Proceedings* 77 (2023): 960-968.

De La Torre, O., Escaler, X., Egusquiza, E., & Farhat, M. (2013). Experimental investigation of added mass effects on a hydrofoil under cavitation conditions. Journal of Fluids and Structures, 39, 173-187.

Deng, Y., Feng, J., Wan, F., Shen, X., & Xu, B. (2020). Evaluation of the turbulence model influence on the numerical simulation of cavitating flow with emphasis on temperature effect. Processes, 8(8), 997.

Downar-Zapolski, P., Bilicki, Z., Bolle, L., & Franco, J. (1996). The non-equilibrium relaxation model for one-dimensional flashing liquid flow. International Journal of Multiphase Flow, 22(3), 473-483.

Ducoin, A., Astolfi, J. A., & Gobert, M. L. (2012a). An experimental study of boundary-layer transition induced vibrations on a hydrofoil. Journal of Fluids and Structures, 32, 37-51.

Ducoin, A., Astolfi, J. A., & Sigrist, J. F. (2012b). An experimental analysis of fluid structure interaction on a flexible hydrofoil in various flow regimes including cavitating flow. European Journal of Mechanics-B/Fluids, 36, 63-74.

Ducoin, A., Astolfi, J. A., Deniset, F. O., & Sigrist, J. F. O. (2010). Fluid structure interaction analysis on a transient pitching hydrofoil. In ASME Pressure Vessels and Piping Conference (Vol. 43673, pp. 665-671).

Ducoin, A., & Young, Y. L. (2013). Hydroelastic response and stability of a hydrofoil in viscous flow. Journal of Fluids and Structures, 38, 40-57.

Ducoin, A., Young, Y. L., & Sigrist, J. F. O. (2010). Hydroelastic responses of a flexible hydrofoil in turbulent, cavitating flow. In Fluids Engineering Division Summer Meeting (Vol. 54518, pp. 493-502).

Duke, D., Swantek, A., Tilocco, Z., Kastengren, A., Fezzaa, K., Neroorkar, K., Moulai, M., Powell, C., & Schmidt, D. (2014). X-ray imaging of cavitation in diesel injectors. SAE international Journal of Engines, 7(2), 1003-1016.

Dular, M., & Bachert, R. (2009). The issue of Strouhal number definition in cavitating flow. Journal of Mechanical Engineering, 55(11), 666-674.

Dular, M., Bachert, R., Stoffel, B., & Širok, B. (2005). Experimental evaluation of numerical simulation of cavitating flow around hydrofoil. European Journal of Mechanics-B/Fluids, 24(4), 522-538.

Fabula, A. (1962). Thin-airfoil theory applied to hydrofoils with a single finite cavity and arbitrary free-streamline detachment. Journal of Fluid Mechanics, 12(2), 227-240.

Ferraro, F., Russo, C., Schmitz, R., Hasse, C., & Sirignano, M. (2021). Experimental and numerical study on the effect of oxymethylene ether-3 (OME3) on soot particle formation. Fuel, 286, 119353.

Fine, N. E. (1988). Computational and experimental investigations of the flow around cavitating hydrofoils. Doctoral Dissertation, Massachusetts Institute of Technology.

Furuya, O. (1975). Nonlinear calculation of arbitrarily shaped supercavitating hydrofoils near a free surface. Journal of Fluid Mechanics, 68(1), 21-40.

Geng, L., Chen, J., De La Torre, O., & Escaler, X. (2020). Numerical simulation of cavitation erosion aggressiveness induced by unsteady cloud cavitation. Applied Sciences, 10(15), 5184.

Giovannetti, L.M., Farousi, A., Ebbesson, F., Thollot, A., Shiri, A., & Eslamdoost, A. (2022). Fluid-Structure Interaction of a Foiling Craft. Journal of Marine Science and Engineering, 10(3), 372.

Givler, S. D., Raju, M., Pomraning, E., Senecal, P. K., Salman, N., & Reese, R. (2013). Gasoline combustion modeling of direct and port-fuel injected engines using a reduced chemical mechanism (No. 2013-01-1098). SAE technical paper.

Gnanaskandan, A. (2015). Development of a methodology for LES of Turbulent Cavitating Flows Doctoral Dissertation, University of Minnesota.

Goncalvès, E., & Charrière, B. (2014). Modelling for isothermal cavitation with a four-equation model. International Journal of Multiphase Flow, 59, 54-72.

Goundar, J. N., & Ahmed, M. R. (2014). Marine current energy resource assessment and design of a marine current turbine for Fiji. Renewable Energy, 65, 14-22.

Hao, J., Zhang, M., & Huang, X. (2019). Experimental study on influences of surface materials on cavitation flow around hydrofoils. Chinese Journal of Mechanical Engineering, 32, 1-11.

Hidalgo, V., Luo, X., Ji, B., & Aguinaga, A. (2014). Numerical study of unsteady cavitation on 2D NACA0015 hydrofoil using free/open-source software. Chinese Science Bulletin, 59, 3276-3282.

Hong, F., Yuan, J., Zhou, B., & Li, Z. (2017). Modeling of unsteady structure of sheet/cloud cavitation around a two-dimensional stationary hydrofoil. Proceedings of the Institution of Mechanical Engineers, Part E: Journal of Process Mechanical Engineering, 231(3), 455-469.

Huang, R. F., Du, T. Z., Wang, Y. W., & Huang, C. G. (2020). Numerical investigations of the transient cavitating vortical flow structures over a flexible NACA66 hydrofoil. Journal of Hydrodynamics, 32, 865-878.

Huang, S., He, M., Wang, C., & Chang, X. (2010). Simulation of cavitating flow around a 2-D hydrofoil. Journal of Marine Science and Application, 9, 63-68.

Huang, Z., Xiong, Y., & Xu, Y. (2019). The simulation of deformation and vibration characteristics of a flexible hydrofoil based on static and transient FSI. Ocean Engineering, 182, 61-74.

Iwai, Y., & Li, S. (2003). Cavitation erosion in waters having different surface tensions. Wear, 254(1-2), 1-9.

Ji, B., Peng, X. X., Long, X. P., Luo, X. W., & Wu, Y. L. (2015). Numerical evaluation of cavitation shedding structure around 3D Hydrofoil: Comparison of PANS, LES, and RANS results with experiments. In Journal of Physics: Conference Series (Vol. 656, No. 1, p. 012127). IOP Publishing.

Jupudi, R. S., Finney, C. E., Primus, R., Wijeyakulasuriya, S., Klingbeil, A. E., Tamma, B., & Stoyanov, M. K. (2016). Application of high-performance computing for simulating cycle-to-cycle variation in dual-fuel combustion engines (No. 2016-01-0798). SAE Technical Paper.

Kamal, H., Ali, A., Manickam, S., & Le, C. F. (2022). Impact of cavitation on the structure and functional quality of extracted protein from food sources–An overview. *Food Chemistry*, 135071.

Kashyap, S. R., & Jaiman, R. K. (2021). A robust and accurate finite element framework for cavitating flows with moving fluid-structure interfaces. Computers & Mathematics with Applications, 103, 19-39.

Kermeen, R. W. (1956). NACA 4412 and Walchner Profile 7 Hydrofoils in Noncavitating and cavitating Flows. Rep. No, 47, 1-21.

Kim, S., Cheong, C., & Park, W. G. (2018). Numerical investigation into effects of viscous flux vectors on hydrofoil cavitation flow and its radiated flow noise. Applied Sciences, 8(2), 289.

Kim, M. J., Kim, S. H., Lee, K. C., Paik, B. G., & Kim, M. C. (2021). Cavitator design for straight-running supercavitating torpedoes. *Applied Sciences*, *11*(14), 6247.

Kinnas, S. A., & Fine, N. E. (1993). A numerical nonlinear analysis of the flow around two- and three-dimensional partially cavitating hydrofoils. Journal of Fluid Mechanics, 254, 151-181.

Kinzel, M., Lindau, J., Peltier, L., Kunz, R., & Sankaran, V. (2007). Detached-eddy simulations for cavitating flows. In 18th AIAA Computational Fluid Dynamics Conference (p. 4098).

Kubota, A., Kato, H., & Yamaguchi, H. (1992). A new modelling of cavitating flows: a numerical study of unsteady cavitation on a hydrofoil section. Journal of fluid Mechanics, 240, 59-96.

Kulkarni, A., García, E. J., Damone, A., Schappals, M., Stephan, S., Kohns, M., & Hasse, H. (2020). A Force Field for Poly (oxymethylene) Dimethyl Ethers (OMEn). Journal of Chemical Theory and Computation, 16(4), 2517-2528.

Kundu, P., Sarkar, A., & Nagarajan, V. (2019). Improvement of performance of S1210 hydrofoil with vortex generators and modified trailing edge. Renewable Energy, 142, 643-657.

Kurtulus, D. F. (2015). On the unsteady behavior of the flow around NACA 0012 airfoil with steady external conditions at Re= 1000. International journal of micro air vehicles, 7(3), 301-326.

Li, D. Q., Grekula, M., & Lindell, P. (2009). A modified SST k-ω Turbulence Model to Predict the Steady and Unsteady Sheet Cavitation on 2D and 3D Hydrofoils. Proceedings of the 7th International Symposium on Cavitation (p. 1-10).

Li, X., Li, B., Yu, B., Ren, Y., & Chen, B. (2019). Calculation of cavitation evolution and associated turbulent kinetic energy transport around a NACA66 hydrofoil. Journal of Mechanical Science and Technology, 33, 1231-1241.

Liaghat, T., Guibault, F., Allenbach, L., & Nennemann, B. (2014). Two-way fluid-structure coupling in vibration and damping analysis of an oscillating hydrofoil. In ASME International Mechanical Engineering Congress and Exposition (Vol. 46476, p. V04AT04A073). American Society of Mechanical Engineers.

Liu, X., Luo, Y., Presas, A., Wang, Z., & Zhou, L. (2018). Cavitation effects on the structural resonance of hydraulic turbines: Failure analysis in a real francis turbine runner. Energies, 11(9), 2320.

Liu, Z. H., Wang, B. L., Peng, X. X., & Liu, D. C. (2016). Calculation of tip vortex cavitation flows around three-dimensional hydrofoils and propellers using a nonlinear k-ε turbulence model. Journal of Hydrodynamics, Ser. B, 28(2), 227-237.

Lohrberg, H., Stoffel, B., Fortes-Patella, R., Coutier-Delgosha, O., & Reboud, J. (2002). Numerical and experimental investigations on the cavitating flow in a cascade of hydrofoils. Experiments in fluids, 33(4), 578-586.

Luo, X. W., Ji, B., Zhang, Y., & Xu, H. Y. (2012). Cavitating flow over a mini hydrofoil. Chinese Physics Letters, 29(1), 016401.

Maes, N., Skeen, S. A., Bardi, M., Fitzgerald, R. P., Malbec, L. M., Bruneaux, G., ... & Martin, G. (2020). Spray penetration, combustion, and soot formation characteristics of the ECN Spray C and Spray D injectors in multiple combustion facilities. Applied Thermal Engineering, 172, 115136.

Majnarić, D., & Zamarin, A. (2020). Stiffness Adjustment of Surface-Piercing Hydrofoils Within Fluid-Structure Interaction. Pomorski zbornik, (3), 189-204.

Matusik, K. E., Duke, D. J., Kastengren, A. L., Sovis, N., Swantek, A. B., & Powell, C. F. (2018). High-resolution X-ray tomography of Engine Combustion Network diesel injectors. International Journal of Engine Research, 19(9), 963-976.

Ming, Z., Mbango-Ngoma, P. A., Xiao-zhen, D., & Qing-Guang, C. (2021). Numerical investigation of the trailing edge shape on the added damping of a Kaplan turbine runner. Mathematical Problems in Engineering, 2021, 1-11.

Mohan, B., Yang, W., Yu, W., & Tay, K. L. (2017). Numerical analysis of spray characteristics of dimethyl ether and diethyl ether fuel. Applied Energy, 185, 1403-1410.

Monette, C., Nennemann, B., Seeley, C., Coutu, A., & Marmont, H. (2014). Hydro-dynamic damping theory in flowing water. In IOP Conference Series: Earth and Environmental Science (Vol. 22, No. 3, p. 032044). IOP Publishing.

Muratoglu, A., & Yuce, M. I. (2015). Performance analysis of hydrokinetic turbine blade sections. Advances in Renewable Energy, 2, 1-10.

Neroorkar, K., Shields, B., Grover Jr, R. O., Torres, A. P., & Schmidt, D. (2012). Application of the homogeneous relaxation model to simulating cavitating flow of a diesel fuel (No. 2012-01-1269). SAE Technical Paper.

Noon, A. A., Arif, M., Tipu, J. A. K., Jabbar, A. U., Siddiqi, M. U. R., & Sharif, A. (2021). Performance enhancement of centrifugal pump through cavitation reduction using optimization techniques. International J. of Thermofluid Science and Technology, 8(4), 080404.

Nur-E-Mostafa, M., Karim, M. M., & Sarker, M. M. A. (2012). Numerical study of unsteady behavior of partial cavitation on two dimensional hydrofoils. Journal of Shipping and Ocean Engineering, 2(1), 10-17.

Örley, F., Hickel, S., Schmidt, S. J., & Adams, N. A. (2017). Large-eddy simulation of turbulent, cavitating fuel flow inside a 9-hole diesel injector including needle movement. International Journal of Engine Research, 18(3), 195-211.

Pastor, J. V., García-Oliver, J. M., Micó, C., & Tejada, F. J. (2020). Comparison of the Diffusive Flame Structure for Dodecane and OME X Fuels for Conditions of Spray A of the ECN. SAE International Journal of Advances and Current Practices in Mobility, 3(2020-01-2120), 402-411.

Payri, R., Gimeno, J., Cuisano, J., & Arco, J. (2016a). Hydraulic characterization of diesel engine single-hole injectors. Fuel, 180, 357-366.

Payri, R., Salvador, F. J., Gimeno, J., & Peraza, J. E. (2016b). Experimental study of the injection conditions influence over n-dodecane and diesel sprays with two ECN single-hole nozzles. Part II: Reactive atmosphere. Energy conversion and management, 126, 1157-1167.

Phillips, R. S. (2012). Cavitation assessment and hydrodynamic performance characteristics of a marine hydrokinetic turbine foil design. Master Thesis, Pennsylvania State University.

Piehl, J., & Bravo, L. (2018). Assessment of Cavitation Models for Computational Fluid Dynamics Analysis of Erosion Risk in a Hydrocarbon-Fueled Nozzle. US Army Research Laboratory: Adelphi, MD, USA.

Pope, S. B. (2000). Turbulent flows. Cambridge university press.

Ranz, W. E. (1958). Some experiments on orifice sprays. The Canadian Journal of Chemical Engineering, 36(4), 175-181.

Saha, K. (2014). Modelling of cavitation in nozzles for diesel injection applications. Doctoral Dissertation, University of Waterloo.

Saha, K., & Li, X. (2015). Assessment of cavitation models for flows in diesel injectors with single-and two-fluid approaches. Journal of Engineering for Gas Turbines and Power, 138(1), 011504.

Saha, K., Som, S., & Battistoni, M. (2017). Investigation of homogeneous relaxation model parameters and their implications for gasoline injectors. Atomization and Sprays, 27(4).

Saha, K., Srivastava, P., Quan, S., Senecal, P. K., Pomraning, E., & Som, S. (2018). Modeling the dynamic coupling of internal nozzle flow and spray formation for gasoline direct injection applications (No. 2018-01-0314). SAE Technical Paper.

Sauer, J., & Schnerr, G. H. (2000). Unsteady cavitating flow-a new cavitation model based on a modified front capturing method and bubble dynamics. In Proceedings of 2000 ASME fluid engineering summer conference (Vol. 251, pp. 1073-1079). ASME.

Schmidt, D. P. (1997). Cavitation in diesel fuel injector nozzles. Doctoral Dissertation, The University of Wisconsin-Madison.

Schmidt, D. P., Rutland, C. J., Corradini, M. L., Roosen, P., & Genge, O. (1999). Cavitation in two-dimensional asymmetric nozzles. SAE transactions, 613-629.

Schmidt, D. P., Rutland, C. J., & Corradini, M. L. (1997). A numerical study of cavitating flow through various nozzle shapes. SAE transactions, 1664-1673.

Sedlar, D., Lozina, Z., & Vucina, D. (2011). Experimental investigation of the added mass of the cantilever beam partially submerged in water. Technical Gazette, 18(4), 589-594.

Sedlar, M., Ji, B., Kratky, T., Rebok, T., & Huzlík, R. (2016). Numerical and experimental investigation of three-dimensional cavitating flow around the straight NACA2412 hydrofoil. Ocean Engineering, 123, 357-382.

Sforzo, B. A., Matusik, K. E., Powell, C. F., Kastengren, A. L., Daly, S., Skeen, S. A., ... & Manin, J. (2018). Fuel nozzle geometry effects on cavitation and spray behavior at diesel engine conditions (No. SAND2018-0300C). Sandia National Lab.(SNL-NM), Albuquerque, NM (United States).

Shaheed, R., Mohammadian, A., & Kheirkhah Gildeh, H. (2019). A comparison of standard k–ε and realizable k–ε turbulence models in curved and confluent channels. Environmental Fluid Mechanics, 19, 543-568.

Smith, S. M., Venning, J. A., Pearce, B. W., Young, Y. L., & Brandner, P. A. (2020). The influence of fluid–structure interaction on cloud cavitation about a flexible hydrofoil. Part 2. Journal of Fluid Mechanics, 897, A28.

Som, S., Longman, D. E., Ramirez, A. I., & Aggarwal, S. (2012). Influence of nozzle orifice geometry and fuel properties on flow and cavitation characteristics of a diesel injector (pp. 112-126). InTech.

Suzuki, T., Mahfuz, H., & Canino, M. (2015). Fatigue load and life estimation of composite turbine blades under random ocean current. In OCEANS 15-MTS/IEEE Washington (pp. 1-7).

Štigler, J., & Svozil, J. (2009). Modeling of cavitation flow on NACA 0015 hydrofoil. Engineering Mechanics, 16(6), 447-455.

Tekawade, A., Mitra, P., Sforzo, B. A., Matusik, K. E., Kastengren, A. L., Schmidt, D. P., & Powell, C. F. (2019a). A comparison between CFD and 3D X-ray Diagnostics of Internal Flow in a Cavitating Diesel Injector Nozzle. In ILASS-Americas 30th Annual Conference on Liquid Atomization and Spray Systems, Tempe, AZ, May 2019.

Uddin, M. I., & Karim, M. M. (2017). Application of volume of fluid (VOF) method for prediction of wave generated by flow around cambered hydrofoil. Procedia engineering, 194, 82-89.

Vijayakumar T (2018). Numerical Investigation on Cavitation and Spray Characteristics of Diethyl Ether and Diesel Fuels. Doctoral Dissertation, Vellore Institute of Technology.

Wang, G., Senocak, I., Shyy, W., Ikohagi, T., & Cao, S. (2001). Dynamics of attached turbulent cavitating flows. Progress in Aerospace sciences, 37(6), 551-581

Westlye, F. R., Battistoni, M., Skeen, S. A., Manin, J., Pickett, L. M., & Ivarsson, A. (2016). Penetration and combustion characterization of cavitating and non-cavitating fuel injectors under diesel engine conditions (No. 2016-01-0860). SAE Technical Paper.

Winklhofer, E., Kull, E., Kelz, E., & Morozov, A. (2001). Comprehensive hydraulic and flow field documentation in model throttle experiments under cavitation conditions. In Proceedings of the ILASS-Europe conference, Zurich (pp. 574-579).

Woods, L. C. (1964). On the theory of growing cavities behind hydrofoils. Journal of Fluid Mechanics, 19(1), 124-136.

Wu, P. C., & Chen, J. H. (2016). Numerical study on cavitating flow due to a hydrofoil near a free surface. Journal of Ocean Engineering and Science, 1(3), 238-245.

Wu, Q., Huang, B., Wang, G., & Cao, S. (2018). The transient characteristics of cloud cavitating flow over a flexible hydrofoil. International Journal of Multiphase Flow, 99, 162-173.

Wu, Y., Liu, S., Dou, H. S., & Zhang, L. (2011). Simulations of unsteady cavitating turbulent flow in a Francis turbine using the RANS method and the improved mixture model of two-phase flows. Engineering with Computers, 27, 235-250.

Wu, T. (1953). A Theory for Hydrofoils of Finite Span. Dep Navy Off Nav Res Rep No 26-8 24426.

Yakhot, V. S. A. S. T. B. C. G., Orszag, S. A., Thangam, S., Gatski, T. B., & Speziale, C. (1992). Development of turbulence models for shear flows by a double expansion technique. Physics of Fluids A: Fluid Dynamics, 4(7), 1510-1520.

Ye, C. L., Wang, C. Y., Zi, D., Tang, Y., van Esch, B. P., & Wang, F. J. (2021). Improvement of the SST γ-Reθt transition model for flows along a curved hydrofoil. Journal of Hydrodynamics, 33(3), 520-533.

Young, Y. L. (2007). Time-dependent hydroelastic analysis of cavitating propulsors. Journal of fluids and structures, 23(2), 269-295.

Young, Y. L. (2008). Fluid–structure interaction analysis of flexible composite marine propellers. Journal of Fluids and Structures, 24(6), 799-818.

Yu, A., Tang, Q., & Zhou, D. (2019). Cavitation evolution around a NACA0015 hydrofoil with different cavitation models based on level set method. Applied Sciences, 9(4), 758.

Zarruk, G. A., Brandner, P. A., Pearce, B. W., & Phillips, A. W. (2014). Experimental study of the steady fluid–structure interaction of flexible hydrofoils. Journal of Fluids and Structures, 51, 326-343.

Zeng, Y., Yao, Z., Gao, J., Hong, Y., Wang, F., & Zhang, F. (2019a). Numerical investigation of added mass and hydrodynamic damping on a blunt trailing edge hydrofoil. Journal of Fluids Engineering, 141(8), 081108.

Zeng, Y. S., Yao, Z. F., Zhou, P. J., Wang, F. J., & Hong, Y. P. (2019b). Numerical investigation into the effect of the trailing edge shape on added mass and hydrodynamic damping for a hydrofoil. Journal of Fluids and Structures, 88, 167-184.

Zhang, S., Chen, H., & Ma, Z. (2021). A modified filter-based model for simulation of unsteady cavitating flows around a NACA66 hydrofoil. Modern Physics Letters B, 35(01), 2150032.

Zhao, S., Xiang, M., Zhou, H., & Zhang, W. (2018). Hydrodynamics analysis on the high-speed surface vehicle with super-cavitating hydrofoils. Journal of Applied Fluid Mechanics, 11(4), 1005-1012.

Zwart, P. J., Gerber, A. G., & Belamri, T. (2004). A two-phase flow model for predicting cavitation dynamics. In Fifth international conference on multiphase flow, Yokohama, Japan (Vol. 152).

Numerical Simulation and Analysis of Cavitating Flow around Hydrofoil and in Injector Nozzle

Thesis submitted in fulfilment of the requirements for the Degree of

DOCTOR OF PHILOSOPHY

By

SRIJNA SINGH

Department of Mechanical Engineering

Bennett University (The Times Group)

Greater Noida, Uttar Pradesh-201310, India

November 2023

CHAPTER 7

CONCLUSIONS

Cavitation occurs in flow regions where the hydrodynamic effect reduces the local pressure below the saturation vapor pressure of the liquid, causing the formation of vapor bubbles. When these vapor bubbles enter the region of higher pressure, they collapse violently producing enough force to damage the solid body. In case of hydrofoils, cavitation can affect the hydrodynamic and structural performance potentially. In injector nozzles, cavitation can cause a fuel injection instability and decreased fuel efficiency. This thesis is a compilation of three studies motivated by the cavitation phenomenon on hydrofoils and in injector nozzle. The goal of the three studies are:

1) Assessment of cavitation and turbulence models on cavitating hydrofoils.
2) Study of the hydrodynamic and structural performance of 3D MHKF-180 and NACA4418 under cavitation using Fluid-Structure Interaction (FSI).
3) Study of the cavitation in Spray C injector nozzle using conventional and alternative fuel.

The major conclusions from these three studies are presented below:

7.1 Assessment of Cavitation and Turbulence Models on Cavitating Hydrofoils

In this part of thesis, the systematic investigation of two different cavitation models i.e., Schnerr -Sauer (SS) and Zwart-Gerber-Belamri (ZGB) and four of four different turbulence models i.e., Standard $k-\epsilon$, RNG $k-\epsilon$, Realizable $k-\epsilon$, and SST $k-\omega$ is studied on cavitating 3D NACA4412 and Clark-y hydrofoil. The performance is computed in terms of lift coefficient, drag coefficient, lift-to-drag ratio, and velocity profiles.

The major findings, based on the above investigation are:

(1) On comparing the performance of SS and ZGB cavitation model on cavitating NACA4412 hydrofoil, both models were found to give similar performance. However, ZGB is used for further numerical simulations on cavitating hydrofoils due to its robustness and accuracy.
(2) On comparing performance of different turbulence models on cavitating NACA4412 and Clark-y hydrofoil, Realizable $k-\epsilon$ was found to be more accurate than other two equations models.

Further using Realizable $k-\epsilon$ turbulence model and Zwart-Gerber-Belamri cavitation model the performance of cavitating MHKF-180s hydrofoil is computed at different angle of attack for Reynolds number ranging from 1.1 X 10^6 – 2.6 X 10^6 at σ =1. Also, comparative study of hydrodynamic performance of 3D cavitating and non-cavitating MHKF-180s hydrofoil is carried out for α varying from -5^o to +12^o at Re =1.3 million. The finding for above analysis are given below:

(3) The hydrodynamic performance of cavitating 3D MHKF-180s hydrofoil at different angles of attack and σ = 1, found to be independent of Reynolds number.

(4) For σ =1, the MHKF-180s has maximum cavity at an angle of attack 12^o at all Reynolds number.

(5) On comparing the hydrodynamic performance of non-cavitating and cavitating (σ =1) MHKF-180s hydrofoil at different angle of attack (α = -5^o, 0^o, 5^o, 7^o, 10^o, and 12^o) at Re = 1.3 X 10^6, it was found that:

   (i) There is no cavitation on MHKF-180s hydrofoil at α = -5^o and 0^o for σ =1.

   (ii) Lift coefficient for cavitating case is reduced as compared to non-cavitating condition with maximum reduction of 40.5% at α = 10^o.

   (iii) The drag coefficient for cavitating cases is higher at almost all angles of attack when compared to non-cavitating conditions due to increase in pressure drag. The maximum increment in C_d value is obtained at α =12^o which is almost seven times of non-cavitating C_d.

   (iv) Lift-to-drag ratio for cavitating condition is found to be lower than non-cavitating condition. The maximum reduction is observed at α =12^o, due to maximum cavity.

   (v) For cavitating condition, the skin friction coefficient (C_f) is found to be lower due to presence of cavity on the upper surface of hydrofoil.

   (vi) At α = 12^o, the x-component velocity on vertical lines of hydrofoil upper surface was found to be lower at σ =1, with much earlier flow separation along the chord.

   (vii) At α = 12^o, the maximum turbulent kinetic energy present at the wake of cavitating hydrofoil was much higher (25 m^2/s^2) than non-cavitating hydrofoil (4m^2/s^2).

In the last part of the first objective, the hydrodynamic performance of MHKF-180s is compared with MHKF-180 at different angles of attack and σ =1. The negligible change is observed in the performance of two foils and therefore, in the second objective of the thesis the hydrodynamic and structural performance of 3D MHKF-180 hydrofoil is compared with NACA4418 at different angles of attack and at different cavitation numbers using FSI.

7.2 Study of the Hydrodynamic and Structural Performance of 3D MHKF-180 and NACA4418 under Cavitation using Fluid-Structure Interaction (FSI)

In this study, a comparative study of structural and hydrodynamic performance of stainless-steel 3D MHKF-180 and NACA4418 cavitating hydrofoil is carried out using one-way Fluid-Structure Interaction (FSI). For this purpose, the numerical simulation is performed using ANSYS Fluent and ANSYS Static structure module. The natural frequency of both the hydrofoils is computed using Acoustic Modal Analysis for the fully wetted condition in still water. The Realizable $k-\epsilon$ turbulence model is used to solve the turbulence effect, and vapor volume fraction is calculated using the Zwart-Gerber-Belamri cavitation model.

The findings, based on the results, are given below:

(1) For different angles of attack at σ = 1, MHKF-180 predicts higher lift coefficient as compared to NACA4418 with maximum percentage difference of 29% at $\alpha = 0^{o}$.
(2) For different cavitation numbers at $\alpha = 8^{o}$, the lift coefficient value of MHKF-180 is higher than NACA4418 with maximum percentage difference of 24.6% at σ = 0.5.
(3) For $\sigma = 1$, the MHKF-180 has larger cavity length than NACA4418 hydrofoil for almost all angles of attack.
(4) The first bending natural frequency of MHKF-180 has been found to be smaller than that for NACA4418 hydrofoil. Their values for MHKF-180 was 193.77 Hz and 202 Hz for NACA4418.
(5) MHKF-180 has larger tip deformation than NACA4418 at all angles of attack. The maximum for MHKF-180 is found as 0.174 mm at $\alpha = 6^{o}$, and for NACA4418 it is found as 0.1325 mm at $\alpha = 12^{o}$.
(6) MHKF-180 has larger tip deformation than NACA4418 for both cavitating and non cavitating condition. The maximum deformation for MHKF-180 is found as 0.194 mm at σ = 2.3, and for NACA4418 it is found as 0.144 mm at σ = 1.2.
(7) For $\sigma = 1$, the maximum von Mises stress developed in MHKF-180 is 95.63 MPa at 6^{o}, while in NACA4418 it is 78.63 MPa at 12^{o}.
(8) For $\alpha = 8^{o}$, the maximum von Mises stress developed in MHKF-180 is 112.88 MPa at σ = 1.5, whereas in NACA4418 it is 93.73 MPa at σ = 1.2.

7.3 Study of the Cavitation in Spray C Injector Nozzle using Conventional and Alternative Fuel

In this study, the cavitation characteristic of conventional n-dodecane fuel is compared with synthetic fuel i.e., oxymethylene ether fuel (OME_3) in cavitating Spray C injector nozzle using commercial CONVERGE v3.0 code. The Homogeneous Relaxation Model (HRM) coupled with the multiphase mixture model is used for cavitation modeling, and RNG $\kappa - \epsilon$ is used to model the turbulence effect. The void fraction contour and the mass flow rate of n-dodecane fuel are compared with the experimental results provided in the literature. The mass flow rate, and contours of mass fraction and density are presented for OME_3 and n-dodecane fuels comparison. The findings are:

(1) The mass flow rate of n-dodecane fuel was found to be in good agreement with the experimental data with a percentage difference of 3%.
(2) The simulations predict the flow separation at the sharp asymmetric corner of the nozzle similar to experimental work. The flow separation at the corner initiates the cavitation along the wall to the nozzle exit.
(3) The mass flow rate obtained for n-dodecane is 9.8 mg/ms and for OME_3 is 11.55 mg/ms. The mass flow rate difference is mainly attributed to higher density of OME_3 fuel.
(4) The OME_3 fuel produced more cavity than n-dodecane fuel in the Spray C nozzle due to higher saturation pressure of OME_3 as compared to n-dodecane.

7.4 Scope for Further Study

The present work has given scope for future studies in the following areas:

(1) Large Eddy Simulation (LES) or Detached Eddy Simulation (DES) turbulence models should be tested to further investigate the role of turbulence models in cavitation on hydrofoils and injector nozzles.
(2) Volume of fluid (VOF) method can be used for the cavitating flow on hydrofoils.
(3) Two-way fluid structure interaction (FSI) study can be used on rigid and flexible cavitating hydrofoils.
(4) Attempts should be made using numerical simulations to understand the failures of hydrofoils caused due to cavitation.
(5) In spray C the effect of cavitation can be studied on the spray formation along with combustion and emission model using OME_3 and other synthetic fuels.